



**University of
Reading**

Department of Mathematics and Statistics

Stalactite Inspired Thin Film Flow

Samuel R. Harrison

A thesis submitted in fulfilment of the requirements for the degree of
Doctor of Philosophy

September 2022

Declaration

I confirm that this is my own work and the use of all material from other sources has been properly and fully acknowledged.

Abstract

Geomorphic patterns are abundant in nature, however the mechanisms that drive the formation and the evolution of these structures are not well understood. In this thesis, we focus on one such pattern. On the surface of stalactites, we find centimetre scale ripples, called crenulations. Stalactites grow as a result of a thin film flowing down the outside, which deposits calcium on the surface. This deposition changes the shape of the wall, which will in turn affect the flow. As the stalactite grows at a much slower rate than the fluid flows, we can model these separately. In this thesis, we will first look at modelling the thin film flow in the appropriate geometries. For this problem, we will consider the radius and the wavelength to be of similar sizes. These will be much larger than the fluid thickness. For this model, we consider the crenulation amplitude to be a similar size to the fluid thickness. We will then look to see how the crenulation wavelength and amplitude affects the flow. Using these flows, we then look at modelling the evolution of the stalactite wall. We examine under what conditions we would expect the crenulations to form and how they evolve once they do.

Acknowledgements

First of all, I would like to thank my supervisor Professor Demetrios Papageorgiou for his guidance throughout the PhD. I am especially grateful to him for his endless enthusiasm, encouragement and expert knowledge.

I am thankful to the MPE CDT for organising funding through EPSRC, as well as hosting events throughout the PhD. Also thanks to all the staff and students, in particular the Echos.

I would like to thank Tim and Lizzy at Treak Cliff Cavern for allowing me to measure and photograph the stalactites there.

I am grateful to Paul for his discussions on improving accuracy of numerical schemes; Oliver, Cathie, and Woody for the enjoyable office environment; and Indi and Jonny for maths sanity checks.

Finally, I would like to thank my family and Kasia for all their support.

Contents

| | |
|--|------------|
| Abstract | iii |
| Acknowledgements | v |
| 1 Introduction | 1 |
| 1.1 The Origins of Stalactites | 1 |
| 1.1.1 Crenulations | 5 |
| 1.2 Thin Film Flows | 7 |
| 1.2.1 Flows down cylinders | 8 |
| 1.2.2 Flows over topography | 9 |
| 1.2.3 Other applications | 10 |
| 1.3 Deposition Problems | 11 |
| 1.4 Outline of the Thesis | 12 |
| 2 Problem Setup | 13 |
| 2.1 Stalactite Parameters | 13 |
| 2.2 Hydrodynamic Model | 19 |
| 2.2.1 Scalings | 21 |
| 2.3 Crenulation Shapes | 25 |

vii

| | | |
|----------|--|-----------|
| 2.4 | Growth of Stalactites | 27 |
| 2.5 | Computational Methods | 29 |
| 3 | Hydrodynamics 1: Inertialess Flow | 33 |
| 3.1 | Introduction | 33 |
| 3.2 | Governing Equations | 34 |
| 3.3 | Steady States | 36 |
| 3.3.1 | Small amplitude wall | 36 |
| 3.3.2 | Numerical steady state solutions | 38 |
| 3.3.3 | Alternative wall shapes | 41 |
| 3.4 | Stability Analysis | 44 |
| 3.5 | Time Dependent Solutions | 47 |
| 3.5.1 | Time periodic waves | 52 |
| 3.5.2 | Branching solutions | 55 |
| 3.5.3 | Dripping cases | 58 |
| 3.6 | Steady State vs. Time Dependent | 60 |
| 3.7 | Conclusions | 61 |
| 4 | Hydrodynamics 2: Effects of Inertia | 63 |
| 4.1 | Introduction | 63 |
| 4.2 | Governing Equations | 64 |
| 4.2.1 | Smooth cylinder case | 65 |
| 4.2.2 | Wall with topography | 68 |
| 4.2.3 | Conservative form | 69 |
| 4.3 | Steady States | 71 |

| | | |
|----------|----------------------------|------------|
| 4.3.1 | Small ϵ | 72 |
| 4.3.2 | Small amplitude walls | 73 |
| 4.3.3 | Nonlinear steady solutions | 78 |
| 4.4 | Linear Stability Analysis | 85 |
| 4.5 | Time Dependent Solutions | 87 |
| 4.5.1 | Different regimes | 88 |
| 4.5.2 | Time periodic waves | 90 |
| 4.6 | Conclusions | 93 |
| 5 | Deposition | 95 |
| 5.1 | Introduction | 95 |
| 5.2 | Underlying Chemistry | 96 |
| 5.2.1 | Chemical reactions | 96 |
| 5.2.2 | Chemical transport | 99 |
| 5.3 | Linear Stability Analysis | 107 |
| 5.4 | Wall Evolution Models | 113 |
| 5.4.1 | Regime 1 - Thin fluid | 113 |
| 5.4.2 | Regime 2 | 117 |
| 5.5 | Conclusion | 123 |
| 6 | Conclusion | 125 |
| | Bibliography | 128 |

List of Tables

| | | |
|-----|---|-----|
| 2.1 | Approximate values of variables for a soda straw stalactite. | 14 |
| 2.2 | Approximate values of variables for a conical stalactite. | 15 |
| 2.3 | Table of approximate fluid thickness for flow rates given in this section . . | 18 |
| 2.4 | Physical parameters | 21 |
| 5.1 | Names of chemicals and their symbols. | 96 |
| 5.2 | Rate and equilibrium constants. Here T is the temperature in Kelvin (Kaufmann and Dreybrodt, 2007; Buhmann and Dreybrodt, 1985). | 101 |
| 5.3 | Rate constants for conversion of carbon dioxide to bicarbonate at 285 K. . | 102 |
| 5.4 | Modelled Stalactite Parameters | 121 |

List of Figures

| | | |
|-----|--|----|
| 1.1 | Conceptual model of karst system. Here we have the rainwater travel through the soil zone, where it reacts with carbon dioxide. This then travels through the carbonate bedrock, where dissolution occurs. The water then reaches the caves through fractures to enter the cave environment, which has a channel to the surface, so the carbon dioxide pressure is lower. In the cave, precipitation occurs, allowing for speleothems to grow Tooth (2000). | 2 |
| 1.2 | The growth of stalactites. (a) shows a drop hanging on the ceiling after water has entered the cave from a fracture. This drop deposits calcium in a ring around its edge. In (b) we see that eventually the drop drips, leaving behind this deposit. (c) shows after some time this ring around the edge has grown downwards, forming a channel in which the water is contained. (d) shows that water now also flows down the outside walls. Now the stalactite is thickening and becoming a conical shape (Moore, 1962). | 4 |
| 1.3 | Stalactites found in caves. a) shows soda straw stalactites on the roof of the National Showcaves Centre for Wales. b) shows stalactites in Treak Cliff Cavern, Castleton, UK. c) a cone stalactite with crenulations also in Treak Cliff Cavern. | 5 |
| 2.1 | Crenulations on a stalactite transitioning between soda straw and conical, at Treak Cliff Cavern, Castleton. | 14 |

| | | |
|-----|--|----|
| 2.2 | Volumetric flow rate of a stalactite in the Père Noël cave, Belgium (Genty and Deflandre, 1998). Here we can see the seasonality of the flow rate, with the summer months experiencing much lower flow rates. There is also a sharp rise in the flow rate during the autumn months, with a more gradual decrease over the spring months. | 16 |
| 2.3 | How the fluid thickness is affected by the radius of the stalactite according to equation (2.4) | 19 |
| 2.4 | Sketch of cross-section of the problem. | 20 |
| 2.5 | Different shapes of steps used as the wall. (a) shows how decreasing the steepness parameter makes the step approach a right angle. (b) shows steps of different widths. | 26 |
| 2.6 | Different shapes of sawtooth used as the wall. (a) shows how decreasing the steepness parameter makes the point of the saw much sharper. (b) shows the different configurations of saw we have. | 27 |
| 2.7 | Numerical error of $(\cos z)_{zzzz}$ for the different differentiation methods, with 2^n points. | 31 |
| 3.1 | (a) The amplitude of the fluid disturbance against the wavelength for $R = 0.5, 1, 2$. (b) The phase shift of the fluid disturbance from the wall disturbance for $R = 0.5, 1, 2$ | 38 |
| 3.2 | (a) Plot showing how the flow rate is affected by walls of different wavelengths and amplitudes. (b) and (c) show the fluid thickness for wavelengths of $L = \pi$ and $L = 4\pi$ respectively. (d) shows the fluid profile in relation to the wall for walls of amplitude $\delta = 1$ | 40 |

| | | |
|-----|--|----|
| 3.3 | Steady state fluid thickness over a wall step. (a) and (c) show how different wavelengths affect the fluid thickness, with the step up and down being equal lengths. (a) shows the fluid profile, whereas (c) shows the difference of the fluid thickness from the mean. (b) has a narrow step up and (d) a narrow step down and are both with wavelength $L = 2\pi$ | 42 |
| 3.4 | Steady state fluid thickness over a wall shaped like a sawtooth. (a) and (b) show how different wavelengths affect the fluid thickness. (a) shows the fluid profile, whereas (b) shows the difference of the fluid thickness from the mean. (c)-(f) show mean fluid thicknesses for different directions of step, all with wavelength $L = 2\pi$. In all cases $\ell = 0.8$ | 43 |
| 3.5 | The number of unstable modes of the steady state for walls of the form $\eta = \delta \cos\left(\frac{2\pi z}{L}\right)$ where $R = \text{Bo} = 1$ | 45 |
| 3.6 | Growth rates of the first 4 unstable modes of the steady states from the Floquet analysis for different amplitude walls. | 46 |
| 3.7 | Plots used to classify the types of the solutions. (i) are plots of $\ h\ _2$ against time, and (ii) are phase plots of $\ h\ _2$ against its time derivative. (a) shows a time periodic solution. (b) has a time periodic solution where the period is different to the time it takes for a fluid peak to traverse 1 spatial period. (c) shows a quasi-periodic solution. (d) shows a non-periodic solution. (e) shows the case where the fluid produces a dripping motion. | 49 |
| 3.8 | Map of the maximum $\ h\ _2$ of figure 3.7(b)-(d). | 50 |
| 3.9 | Speed of main peak in travelling wave for different wavelength and amplitude walls. | 51 |

| | | |
|------|---|----|
| 3.10 | (a) Plot showing the $\ h\ _2$ for 20 time units from $t = 300$ (b), (c) and (d) show the fluid thickness for wavelengths of $L = 2.25\pi$, $L = 4\pi$ and $L = 6\pi$ respectively where the amplitude of the wall is $\delta = 1$ for all cases. The grey curves are taken every 0.1 time unit between the consecutive maximums highlighted in (a). The fluid thickness at the maximum and minimum flow rates and $\ h\ _2$ are highlighted. | 53 |
| 3.11 | Colour plots showing the fluid thickness moving in a frame that travels at the mean wave speed. (a) shows all 500 time units for the $L = 4\pi$ case. (b), (c) and (d) show the fluid thickness for wavelengths of $L = 2.25\pi$, $L = 4\pi$ and $L = 6\pi$ respectively where the amplitude of the wall is $\delta = 1$ for all cases. These have been taken from $t = 300$ and show at least one period. The location of the peaks and troughs of the fluid thickness is highlighted, as well as the time at which the fluid thickness peak travels above the peaks and troughs of the wall. | 54 |
| 3.12 | The fluid thickness for the travelling in a frame of reference that tracks the waves. (a) is the $\delta = 1, L = 4\pi$ showing a single peak (b) is the $\delta = 1, L = 6\pi$ showing a double peak (c) is the $\delta = 1, L = 9\pi$ showing a triple peak. | 55 |
| 3.13 | Example solutions that occur for wall wavelength $L = 9\pi$ with wall amplitude being $\delta = 1$. (a)-(c) are time periodic solutions, with (d)-(e) being non-periodic solutions. Subfigures (i) show the fluid thickness over time in a frame that moves with the mean speed of the wave. Subfigures (ii) show the time averaged size of the first 10 Fourier modes of the fluid thickness, as well as the range. | 57 |
| 3.14 | Mean flow rates for a periodic travelling wave ($\delta = 1$), a dripping case ($\delta = 3$), and where the fluid is held in place ($\delta = 3.5$). | 58 |

| | | |
|------|--|----|
| 3.15 | Fluid profiles for a dripping case where the wall is $\eta = 3 \cos(\frac{z}{2})$. (a) shows the 50 time unit period where the fluid moves slowly from the wall peak. (b) shows a 5 time unit period where most of the fluid traverses the wall period. | 59 |
| 3.16 | Fluid profiles that result from simulating the flow with low mean flow rates. | 59 |
| 3.17 | The difference between the time averaged fluid thickness and the steady state. (a) shows cases from figure 3.13. (b) shows the example of the dripping case from 3.15. | 61 |
| 4.1 | Geometry of the smooth cylinder problem | 65 |
| 4.2 | Geometry of the problem with a wall disturbance | 68 |
| 4.3 | How the wavelength affect the amplitude (a) and the phase shift (b) for small ϵ | 73 |
| 4.4 | Phase shift of the fluid thickness disturbance from the wall disturbance, depending on the wavelength L and ϵ . Here $Re, R, Bo = 1$ | 76 |
| 4.5 | How the parameters affect the fluid disturbance. (a) shows the effect of the wavelength on the amplitude for different radii, here $Re, Bo = 1$ and $\epsilon = 0.1$. The dotted lines are the small ϵ approximation from equations (4.41)-(4.42) (b) shows how the phase shift is deflected from π when $L = 2\pi, R = 1, Bo = 1$. | 77 |
| 4.6 | How the wall shape affect the disturbance to the fluid thickness. (a) shows the amplitude of the fluid disturbance compared to the amplitude of the wall. (b) shows the phase shift of the fluid disturbance from the wall disturbance. | 80 |
| 4.7 | Normalised disturbance to the fluid thickness for different amplitude walls. Here $R = Bo = Re = 1$. The subplots have wavelengths (a) $L = \pi$, (b) $L = \frac{3\pi}{2}$, (c) $L = 2\pi$ and (d) $L = 4\pi$ | 82 |
| 4.8 | Fluid thickness for different (a) Reynolds numbers and (b) Bond numbers. The subplots have wavelengths (i) $L = \pi$, (ii) $L = 2\pi$ and (ii) $L = 4\pi$ | 83 |

| | | |
|------|---|-----|
| 4.9 | Fluid thickness for different (a) radii and (b) ϵ . The subplots have wavelengths (i) $L = \pi$, (ii) $L = 2\pi$ and (iii) $L = 4\pi$ | 84 |
| 4.10 | The number of unstable modes of the steady state for walls of the form $\eta = \delta \cos\left(\frac{2\pi z}{L}\right)$ where $R = \text{Bo} = \text{Re} = 1$, $\epsilon = 0.1$ | 86 |
| 4.11 | Plots used to classify the types of the solutions. (i) are plots of $\ H\ _2$ against time and (ii) are phase plots of $\ H\ _2$ against its time derivative. (a) shows a stable steady state. (b) shows a time periodic solution. (c) shows a quasi-periodic solution. (d) shows a non-periodic solution. (e) shows the case where the solution blows up. | 89 |
| 4.12 | Fluid thickness for different shaped walls over a period for time periodic waves. (a)-(c) have a wavelength of 2π (d) has 1.73π (e) has 3π and (f) has 4π . (a) has amplitude 0.1, (b), (d) and (e) have amplitude 1 and (c) and (f) have amplitude 3. The grey lines show the fluid thickness every 0.1 time units. The fluid thicknesses with the maximum and minimum $\ H\ $ are shown, as well as the steady state fluid thickness. | 91 |
| 4.13 | Colour plots that show the fluid thickness moving in a frame that travels at the mean wave speed. (a) shows a time periodic wave, (b) shows a quasi periodic wave and (c) shows a chaotic wave. | 92 |
| 5.1 | Values for the rates k_+ and k_- for different pH, at temperatures of 12°C and 20°C | 104 |
| 5.2 | Rate at which carbon dioxide is produced dependent on the partial pressure of Carbon dioxide. The rate was calculated from equation (5.23), where the bicarbonate concentration is calculated using equation (5.29), at a temperature of 12°C and a pH of 8. This was done for initial calcium concentrations of 2 and 5 mol/m ³ | 105 |

| | | |
|-----|---|-----|
| 5.3 | Growth of wall perturbation. (a) and (b) shows for which radius and wavelength that the wall perturbation grows, highlighting the most unstable wavelength for a given radius. (c) shows the speed at which the radius grows. (d) and (e) show the speed at which the perturbation grows and also the speed at which it travels. (a) and (d) have a flow rate of 10^{-9} m ³ /s. (b) and (e) have a flow rate of 5×10^{-9} m ³ /s. | 111 |
| 5.4 | Growth of wall perturbation for different flow rates and wavelengths. (a) has a radius of 5 mm and (b) has a radius of 5 cm. | 112 |
| 5.5 | Radii and wavelengths for which growth occurs. Here we have a wall amplitude of $\delta = 1$ and a flow rate $Q = 1 \times 10^{-9}$ m ³ /s. | 120 |
| 5.6 | Growth of the radius for the modelled stalactite (a) shows the size of the radius and (b) shows the speed at which it grows. | 122 |
| 5.7 | Growth of the crenulation amplitude for the modelled stalactite (a) shows the size of the amplitude and (b) shows the speed at which it grows. | 122 |
| 5.8 | Migration of the crenulation peak. | 123 |

Chapter 1

Introduction

This thesis is motivated by the morphological instabilities, called crenulations, that form on calcite surfaces. These instabilities can be seen on flowstones, draperies, and stalagmites (Meakin and Jamtveit, 2010), but here we will focus on the crenulations that occur on the surface of stalactites. Stalactites grow as a result of a thin liquid film that is saturated with calcium, and this calcium is deposited on the wall (Short et al., 2005b). The shape of the stalactite will affect the flow of the fluid. This in turn will affect how the calcium is deposited, which again changes the shape. We will therefore be looking into modelling the flow based on a stalactite with crenulations, and then we will look at seeing how this flow will affect the growth.

1.1 The Origins of Stalactites

In order to model the problem, we must first understand how stalactites form. We will be looking at limestone stalactites that form in caves, however stalactites can also form from other minerals being deposited (Hicks, 1950). Stalactites can also form from the solidification of lava (Allred and Allred, 1998) and water, however, these have different boundary conditions. Icicles, for example, have a growth rate depending on the temperature gradient (Ueno, 2007), rather than a concentration gradient, which is the case for limestone

(Bertagni and Camporeale, 2017).

The overall process is described in more detail in Fairchild et al. (2012), and the main points are summarised below. In the karst environment, the process begins with rainwater.

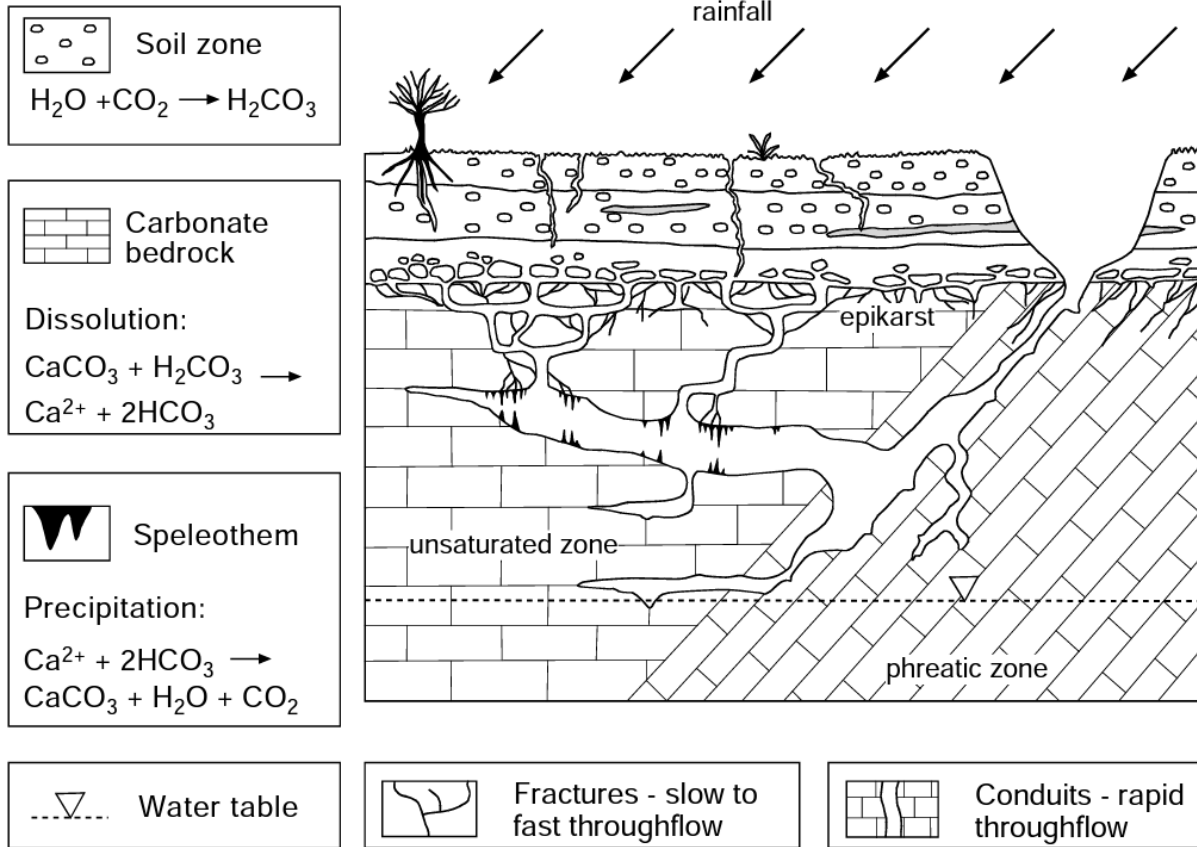


Figure 1.1: Conceptual model of karst system. Here we have the rainwater travel through the soil zone, where it reacts with carbon dioxide. This then travels through the carbonate bedrock, where dissolution occurs. The water then reaches the caves through fractures to enter the cave environment, which has a channel to the surface, so the carbon dioxide pressure is lower. In the cave, precipitation occurs, allowing for speleothems to grow Tooth (2000).

As the water percolates through soil, it absorbs carbon dioxide that has been released by microorganisms, plants, and animals through respiration (Raich and Schlesinger, 1992). This carbon dioxide mixed in the water forms carbonic acid. Under the soil layer we have a bedrock of limestone. Limestone is very porous and contains joints and fractures that the water can flow through. As the water is now acidic, it dissolves the calcium from the limestone, which in turn causes the fractures to grow. The calcium rich water then enters a cave environment, a large cavity in the bedrock. The cave may have an opening

and where there is good ventilation, then the cave will have a CO_2 pressure similar to that of the atmosphere. As the CO_2 concentration is much higher in the water than the atmosphere, it is outgassed until it attains equilibrium with that of the cave atmosphere. This in turn increases the pH of the water, resulting in it becoming supersaturated with calcium carbonate. Stalactites form as this calcium carbonate is deposited (Dreybrodt, 2012; Meakin and Jamtveit, 2010). Initially, the water forms pendant drops on the cave's ceiling. These droplets may form directly under the fissure that fed the water onto the ceiling, however where there is a gradient on the ceiling the pendant drop may travel towards a local minimum (Maltsev, 1999). The initial drop deposits a ring of calcite around the outside in a manner similar to that found by Kumar et al. (2021). This ring builds up and acts as a channel for water to flow down the middle of (Moore, 1962). These channels are known as tubular or soda straw stalactites.

Soda straws fed from a fracture clearly have the water flowing down the inside. Maltsev (1999) suggests that soda straws can still appear when they are not under a feeding fracture, as a large pressure difference can cause water to be sucked through the cleavage in the calcite crystals into the inner channel.

Curl (1972) looked into the growth of soda straw stalactites and found that they must have a minimum radius of around 2.5 mm, which is a result of the surface tension of the drop. Moore (1962) and Paul et al. (2013) noted that soda straws stalactites grow seasonally due to increased pressure of CO_2 in the soil during summer months, causing a fluctuation of the pH across a year. Additionally, the flow rate can change with Arbel et al. (2010) noting the groundwater is linked with rainfall in the area. This results in seasonal differences in the groundwater as well as shorter term increases after storms, which also would affect the growth rate. This results in the soda straw stalactites having visible growth layers. Conical stalactites form when water starts flowing down the outside of soda straw stalactites. This may be due to leakage from the walls if the flow rate is large enough (Ford and Williams, 2013). Conical stalactites can have both internal and external feeding, however the inner channel may get blocked, resulting in growth only

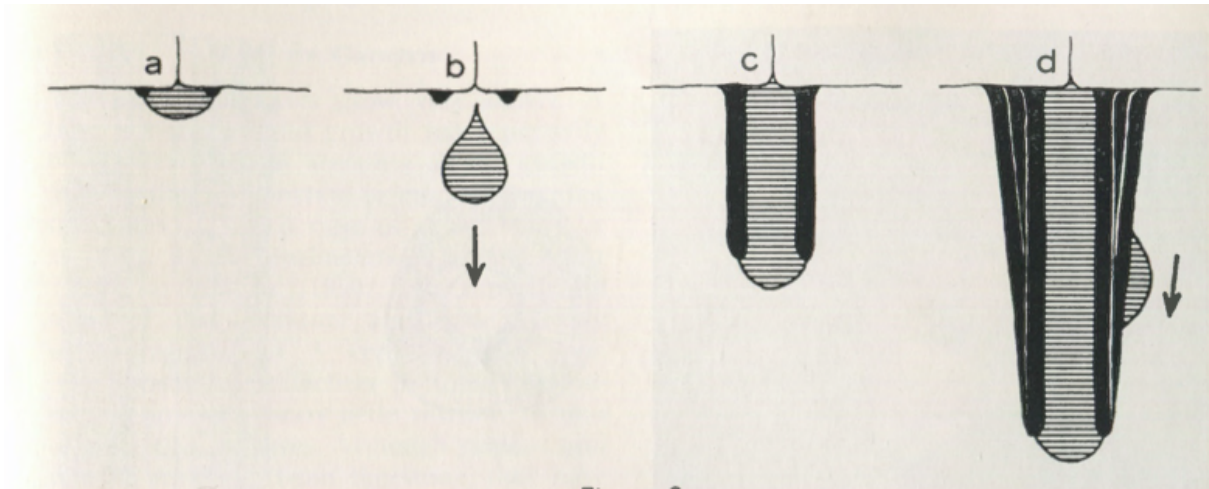


Figure 1.2: The growth of stalactites. (a) shows a drop hanging on the ceiling after water has entered the cave from a fracture. This drop deposits calcium in a ring around its edge. In (b) we see that eventually the drop drips, leaving behind this deposit. (c) shows after some time this ring around the edge has grown downwards, forming a channel in which the water is contained. (d) shows that water now also flows down the outside walls. Now the stalactite is thickening and becoming a conical shape (Moore, 1962).

coming from the fluid flowing down the outer walls. Conical stalactites tend to have higher flow rates than soda straw stalactites (Fairchild and Baker, 2012). Therefore, an increase in the volume of water should occur for the soda straws to transition. Kim and Sanderson (2010) provides a possible transition event with changes in rock fractures. Here they note that the size of the fractures or intersection between two fractures can increase the flow, which in turn results in bigger stalactites.

The effect of the external flow was looked at by Short et al. (2005b). Here they were able to model the overall conical shape of stalactites. As the calcite crystals grow with their long axis perpendicular to the calcite surface (Moore, 1962), we can determine whether the growth was due to internal or external feeding. Here, internal feeding results in crystals orientated parallel to the flow, as the stalactite lengthens from the bottom. External flow causes the radius of the stalactite to increase, and so the calcite crystals are perpendicular to the flow direction (Moore, 1962; Forti and Springer, 2020).



Figure 1.3: Stalactites found in caves. a) shows soda straw stalactites on the roof of the National Showcaves Centre for Wales. b) shows stalactites in Treak Cliff Cavern, Castleton, UK. c) a cone stalactite with crenulations also in Treak Cliff Cavern.

1.1.1 Crenulations

Many limestone features have patterns on their surface (Meakin and Jamtveit, 2010), with stalactites being no exception. On the surface of stalactites, there are centimetre scale ripples known as crenulations. These can be seen on figure 1.3 (c). Previous works mostly focus on looking at the effect of a small perturbation to the wall fluid interface (Vesipa et al., 2015; Camporeale and Ridolfi, 2012; Camporeale, 2017). These works often ignore the effect of the radius of the stalactite, however the radius is a similar length to the crenulation wavelength. The linear stability analysis is usually performed based on a large radius stalactite. The crenulations could form on stalactites with smaller radii, as we have these dynamics as soon as the water starts flowing down the outside of a soda straw stalactite.

Crenulations also form on icicles (Ueno, 2007; Ueno et al., 2009; Bertagni and Camporeale, 2017). The hydrodynamics can be modelled in the same way for both icicles and

stalactites, as they exhibit similar shapes, and have a thin film flowing down them. The wall growth equations are slightly different, but at leading order for both cases, the wall grows proportionally to the fluid thickness. The wall growth rate being 10^5 times faster in the ice case than the karst case (Bertagni and Camporeale, 2017).

Ueno (2007) looks at thin film flow down an inclined plane. The solid-liquid interface is initially considered flat. A perturbation is made to the solid liquid interface, which results in a perturbation to the fluid liquid interface. The ratio between the amplitudes of the wall and fluid disturbances is looked at for a vertical fluid and one going down a gentle slope of angle $\frac{\pi}{18}$. The amplitude of the fluid disturbance is found to be less than the wall disturbance. Here it is also found that the wavelength of the crenulations depends on two length scales, one being the capillary length and the other being the fluid thickness. The wavelength also depends on the dimensionless Péclet number, which is the ratio of heat transfer to thermal diffusion. Ueno et al. (2009) expanded on these ideas, changing the thermal boundary conditions.

Camporeale and Ridolfi (2012) model the growth of stalactites by making use of the PWP equation for calcite deposition (Plummer et al., 1978)

$$F = \kappa_1(\text{H}^+) + \kappa_2(\text{H}_2\text{CO}_3^*) + \kappa_3 - \kappa_4(\text{Ca}^{2+})(\text{HCO}_3^-). \quad (1.1)$$

This shows that the rate of calcite deposition (F) depend on the activities of hydrogen, calcium, and bicarbonate ions, as well as the activity of carbonic acid. The equation is based on the reactions which occur to produce calcite, with κ_i being the rate constants for these reactions. Using this, they performed linear stability analysis to calculate critical wavelengths depending on the fluid thickness. Here they also found that the crenulations should migrate upstream. Vesipa et al. (2015) also looks at a thin film down an inclined plane. Again they made use of the PWP equations and considered a perturbation to the bottom surface. They looked more fully at how the Reynolds number, calcium concentration, pressure of carbon dioxide, temperature, and angle affected the growth. Here they found that the wavelength of the crenulations was only substantially affected by

the fluid properties. However, all these properties could have a substantial effect on the growth rate and migration speed.

Camporeale (2017) worked to improve the hydrodynamics of the previous models by using a gradient expansion technique to find an evolution equation for the fluid surface. A formula for the wavelength of the crenulations was found based on the Reynolds number and calcium concentration. He also derived a formula for the migration speed. These models all suggest that the crenulation wavelength should increase with the Reynolds number. Physically, this can be viewed as thicker fluids result in longer wavelengths. However, if the flow rate is constant, a stalactite with a larger radius will result in a thinner film, meaning that it should have a smaller wavelength.

Other geological features can also form from thin films flowing down inclined planes. Draperies which are an instability in the direction of flow of the fluid can occur on underhanging walls (Ledda et al., 2021).

1.2 Thin Film Flows

Thin films are those where the thickness of the fluid is much smaller than the characteristic length scale of the flow. This allows the introduction of a small parameter ϵ , which is the ratio between the fluid thickness and the larger length scale.

In the case of stalactites, the longer length scale can be either the wavelength of the crenulation or the radius of the stalactite. The momentum and mass equations can be approximated by only looking at the terms which appear at leading order or first order in ϵ . Various review papers have looked into the dynamics and instabilities caused by thin films, such as Craster and Matar (2009); Oron et al. (1997). Here we can see that the fluid can be driven by several different forces such as gravitation, centrifugal, intermolecular or electromagnetic. The film can also be driven by thermal gradients and will be affected by surface tension and topography.

In the case of stalactites, we have gravity driven flow over topography. Gravity driven

flows can be separated into those with or without significant inertia. With negligible inertia, it is interesting to look at the contact line. It has been shown theoretically and experimentally that the contact line develops fingers or rivulets across the flow (Bertozzi and Brenner, 1998; Johnson et al., 1999). The instability on the surface of stalactites is perpendicular to the flow, so is unlikely to arise because of this. Falling films with significant inertia lead to waves in the direction of the flow (Chang et al., 1993).

Taking a gravity driven thin film down an inclined plane and expanding up to $O(\epsilon)$ one can derive the Benney equation (Benney, 1966)

$$h_t + \left(\frac{2}{3}h^3 + \epsilon \left(\frac{16 \text{Re}}{15}h^6h_x - \frac{2}{3}\cot\theta h^3h_x + \frac{1}{3\text{Bo}}h^3h_{xxx} \right) \right)_x = 0. \quad (1.2)$$

This gives an evolution equation for the fluid thickness h , which has the effects of the Reynolds number Re , which is the ratio between inertial and viscous forces; the Bond number Bo , which is the ratio between gravitational forces and the surface tension forces; and the angle of the slope from the horizontal θ . The subscripts denote derivatives, with t being time and x is the spatial coordinate in the direction of the flow.

Under suitable rescaling, the Benney equation (1.2) can be reduced to a weakly nonlinear evolution equation known as the Kuramoto-Sivashinsky equation Kuramoto (1978); Sivashinsky (1977)

$$h_t + hh_x + h_{xx} + h_{xxx} = 0. \quad (1.3)$$

1.2.1 Flows down cylinders

In the case of stalactites, instead of flow down an inclined plane, we will consider flow down an axisymmetric and vertical cylinder. Work here generally considers the fluid to be thin compared to the radius. Considering the surface tension to be the leading cause for wave formation, Frenkel (1992) derived an evolution equation for the free surface. This

was rescaled by Kalliadasis and Chang (1994) to

$$h_t + (h^3 + \beta h^3 h_x + h^3 h_{xxx})_x = 0 \quad (1.4)$$

where the parameter β depends on the Bond number and the radius. This equation was studied numerically to find that depending on the size of the radius, the fluid interface could exhibit solitary wave like structures or blow-up in finite time.

Considering a long wave perturbation of the fluid interface of a similar length to the radius of a cylinder, Frenkel (1993) derives an equation similar to the Benney equation (1.2)

$$h_t + 2h^2 h_x + \epsilon \left(\frac{8 \text{Re}}{15} h^6 h_x + \frac{1}{3 \text{Bo}} \left(\frac{h_x}{R^2} + h_{xxx} \right) + \frac{1}{6R} h^4 \right)_x = 0 \quad (1.5)$$

which in addition to the parameters seen in the Benney equation (1.2), has the parameter R , the ratio between the radius of the cylinder and the fluid thickness. Here instead of the slope term we have a similar $h^3 h_z$ term as a result of the curvature of a cylinder. There is also an additional h^4 term. However, in the limit where the radius increases to infinity these terms vanish, and we are left with the Benney equation (1.2) for a vertical plane.

Craster and Matar (2006) consider thin film flow down a cylinder, where the radius is not necessarily thicker than the fluid thickness. Here, they use scalings similar to those used by Papageorgiou (1995) to model viscous liquid threads. Craster and Matar (2006) consider the fluid to be thin compared to a capillary length scale. Here they compared experimental results with those simulated numerically and found a good agreement between the two.

1.2.2 Flows over topography

Another feature that could influence the flow on a stalactite is the shape of the crenulations. Surface topography leads to additional surface tension terms. Flow down an inclined plane

with sinusoidal walls has been studied by Wierschem and Aksel (2003); Wierschem et al. (2005). Here they used linear and Floquet analysis to determine the stability of steady state solutions. Here they discovered that the wall corrugations have a stabilising effect.

Kalliadasis et al. (2000) looks at the effect that trenches and mounds have on the steady state fluid thickness. The shape of the trench was modelled as

$$\eta = \delta \left(1 + \frac{1}{\pi} \left(\tan^{-1} \left(\frac{x - \ell}{\xi} \right) - \tan^{-1} \left(\frac{x}{\xi} \right) \right) \right) \quad (1.6)$$

with δ, ℓ, ξ representing the trench depth, width, and steepness. Here they found that a capillary ridge forms just upstream of where the wall steps down.

Tseluiko et al. (2013) looked at the stability of film flowing down an inclined plane with topography. Here they looked at both sinusoidal walls and trenches. On sinusoidal walls, the steady state fluid is thinnest around the wall maximum. Here they found that the wavelength and the amplitude of the wall can be either stabilising or destabilising.

Combining cylindrical geometry with a wall perturbation was done experimentally by Kuehner et al. (2019, 2021). Here they used a 3D-printed pipe with semicircular corrugations. Water was poured down the inside of the pipe and a statically deformed free surface was observed. Here they found that the free surface amplitude increased as the wall amplitude did. They also observed that the phase shift of the free surface changed the most for shorter wavelengths.

1.2.3 Other applications

While the motivation for the fluid dynamics was based on stalactites, flow down a cylinder with topography could have many industrial applications. Coating a surface is one such application, and modelling it can be important to minimise defects that could arise as a result of an instability. Several coating methods are listed in a review paper by Weinstein and Ruschak (2004).

An example of this is the manufacturing of 3D printed parts (Zhu et al., 2015). Here,

the coating film could smooth surface defects or cause them to grow. The geometry of our problem could also be useful for desalination (Sadeghpour et al., 2019; Zeng et al., 2019). Here, water vapour can be condensed onto liquid beads. Such beads form on cylindrical strings, where the size of the beads would be influenced by the radius and the topography.

1.3 Deposition Problems

Stalactites grow due to the deposition of calcium on the surface. As dissolution and precipitation are related through a reversible reaction, much work on calcite precipitation is based on Plummer et al. (1978). Here they derive a rate equation for dissolution of calcium known as the PWP equation. This requires the concentration of the chemicals at the calcite surface. Buhmann and Dreybrodt (1985) expanded on this by looking at how chemicals are transported throughout the fluid layer. In this work they determined that for calcite dissolution and precipitation, the rate could be limited by the conversion of carbon dioxide to carbonic acid or diffusion across the fluid, depending on the fluid thickness.

The precipitation was looked into further in Dreybrodt (1980, 1981), with the cases with a thin fluid layer having precipitation rates increasing with the fluid thickness. However, with larger film thicknesses, where diffusion becomes the rate limiting process, thicker film thickness can cause smaller precipitation rates. Dreybrodt (1999) uses these to model stalagmite growth, where he looks at how different flow conditions, temperature, concentration of calcium ions and fluid thicknesses affect the growth rates.

For stalactites, Short et al. (2005b) shows that the time it takes for calcium ions and carbon dioxide to diffuse from the stalactite boundary to the air boundary is around 0.1s. This is much faster than that of the rate limiting carbon dioxide reaction, which takes around 10s. Therefore, we expect to be in the case where the deposition is proportional to fluid thickness. Vesipa et al. (2015) however, suggests that crenulations in the wall grow more when the fluid is thinnest. The chemical model is looked at more extensively in

chapter 5.

1.4 Outline of the Thesis

In chapter 2 we show the derivation of the models that will be used. Chapters 3 and 4 look at the hydrodynamics of the problem. Specifically, chapter 3 has the fluid primarily driven by surface tension, where chapter 4 uses a Benney like equation. Chapter 5 looks at the deposition of calcium on the wall and the resulting moving boundary problem. Chapter 6 concludes.

Chapter 2

Problem Setup

2.1 Stalactite Parameters

We wish to model our stalactite as a cylinder with a thin film flowing down it. For this model, we will have four main parameters that can change. These are the flow rate of water Q ; the radius of the stalactite \tilde{R} ; the amplitude of the crenulation $\tilde{\delta}$; and the wavelength of the crenulation \tilde{L} . The fluid thickness \tilde{h} is also an important parameter for the growth of stalactites. It is however derived from the flow rate and the radius. In order to create our model, it would be useful to know approximate values for these parameters.

We will look at the stalactites in the two different stages in their life: soda straw stalactites, where the flow is predominantly internal; and conical stalactites, where the flow is predominately external. As stalactites evolve from soda straw stalactites to conical ones, we can model stalactites having reasonable values between the two.

For a soda straw stalactite the diameter, which Curl (1972) found to depend on the surface tension, was calculated to be around 5 mm for water. Samples studied by Paul et al. (2013) confirm diameters of this size. Soda straw stalactites have banding based on yearly growth (Paul et al., 2013; Fairchild et al., 2001; Huang and Fairchild, 2001; Huang et al., 2001; Desmarchelier et al., 2006). This is due to the seasonal fluctuation of rainfall and carbon dioxide. These bands are 0.5 mm long, with a relief of 2 μm . Soda straws can

get up to 6 m in length, however, as they are fragile, many of them break when they are only 100s of millimetres long (Fairchild and Baker, 2012).

In summary, we are looking at these values.

| Variable | Symbol | Value |
|--------------------|------------------|----------------------|
| Diameter | $2\tilde{R}$ | 5×10^{-3} m |
| Banding amplitude | $ \tilde{\eta} $ | 2×10^{-6} m |
| Banding wavelength | \tilde{L} | 5×10^{-4} m |
| Length | ℓ | 0.1-6 m |

Table 2.1: Approximate values of variables for a soda straw stalactite.

Soda straw stalactites are fairly regular in their dimensions, where conical stalactites are less so. This is because conical stalactites have the fluid now flowing down the outside. This means that calcium will be deposited on the outside surface, increasing the radius. Some smaller stalactites were measured in Treak Cliff Cavern, Castleton, UK.



Figure 2.1: Crenulations on a stalactite transitioning between soda straw and conical, at Treak Cliff Cavern, Castleton.

Figure 2.1 shows a stalactite of radius 7 mm. This would be an example of a transitioning stalactite. Here the crenulation wavelength was 4 mm and the amplitude was too small

to measure. A stalactite of radius 17 mm was also measured. Here the crenulations had a wavelength of 8 mm and an amplitude of 0.4 mm. According to Short et al. (2005b); Vesipa et al. (2015) conical stalactites have the values.

| Variable | Symbol | Value |
|-------------------------|-------------|------------------------------|
| Radius | \tilde{R} | $(0.5 - 1) \times 10^{-1}$ m |
| Crenulation wavelengths | \tilde{L} | $(1 - 10) \times 10^{-2}$ m |
| Length | ℓ | 0.1-6 m |

Table 2.2: Approximate values of variables for a conical stalactite.

While the wavelength of the bands on soda straw stalactites may seem small compared to the values of conical stalactites, the ratio between the wavelength and the radius is similar. When performing linear stability analysis, Vesipa et al. (2015); Camporeale (2017) consider a small perturbation to an inclined plane. These small amplitude bands could be viewed as the initial disturbance in the analysis. Another thing to note is if the same amount of fluid is flowing down the outside of a soda straw stalactite, the fluid thickness would be larger than for the conical case, due to the smaller radius.

Next we will consider the flow rate. Soda straws typically grow when they have lower flow rates than conical stalactites. This is because carbon dioxide is only degassed once the fluid comes into contact with the air as it forms a drop. If the flow rate is too high, the drop will drip before it has had time for calcite to be deposited on the walls (Forti and Springer, 2020). According to Short et al. (2005b) typical flow rates are 10 – 1000 cm^3/hour depending on how much rainfall the area around the cave gets. These values are given per hour, so it is likely that these measurements were taken over a couple of hours. As stalactites take many years to grow, it would be better to have mean flow rates measured over a similar period of time. Genty and Deflandre (1998) recorded the drip flow under a soda straw stalactite of the Père Noël cave in Belgium. Here they found the minimum flow rate was 227 ml/day, with the maximum flow rate being 10 135 ml/day. Over the 5 years of data the mean flow was 1763.3 l/year. Even et al. (1986) measured

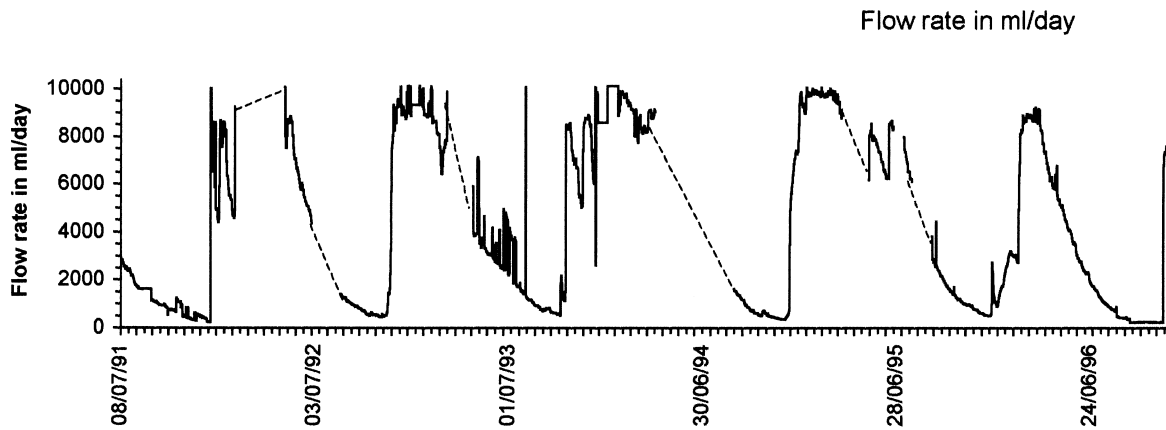


Figure 2.2: Volumetric flow rate of a stalactite in the Père Noël cave, Belgium (Genty and Deflandre, 1998). Here we can see the seasonality of the flow rate, with the summer months experiencing much lower flow rates. There is also a sharp rise in the flow rate during the autumn months, with a more gradual decrease over the spring months.

the flow rates of various stalactites in the Soreq Cave in Israel. Here they measured :

- a straw stalactite with mean discharge 100 ml/day throughout the year.
- a conical stalactite that showed little correlation with the rain, that discharged 85-95 ml/day in summer and 95-100 ml/day in winter.
- a straw stalactite that varies seasonally with 2500-2800 ml/day during winter, decreasing to 170 ml/day in June and 5-8 ml/day in late summer.
- a conical stalactite with a straw on its end. This has a discharge of around 14 ml/day.

These high flow rates on soda straw stalactites in winter are likely to be too fast for growth, with the seasonal banding showing the most growth in summer (Paul et al., 2013).

If the flow rate exceeded the maximum flow rate for water within the soda straw, we would know that fluid must also travel down the outside. The maximum flow rate within the soda straw stalactite would be equivalent to flow down a pipe acting under gravity. This is a Poiseuille flow (Batchelor and Batchelor, 2000) where it is driven by gravity. This

results in the vertical velocity

$$w(r) = \frac{g}{4\nu}(a^2 - r^2) \quad (2.1)$$

which depends on the axial displacement r . Here ν is the kinematic viscosity, g is acceleration due to gravity and a is the radius of the soda straw stalactite. Integrating the velocity over the surface area of the cross-section of the fluid gives the flow rate

$$Q = \frac{\pi a^4 g}{8\nu}. \quad (2.2)$$

The radius of a soda straw stalactite is 2.5 mm, and the kinematic viscosity of water is 1 mm²/s, therefore we find in this case the flow rate would be $Q \sim 1 \times 10^{-4}$ m³/s. The highest flow rate for the soda straw observed in previously mentioned caves was $Q \sim 1 \times 10^{-7}$ m³/s, which is significantly lower, meaning even in winter months, water will flow in a film down the inside of the soda straw stalactite until it joins the drop at the tip.

For conical stalactites Short et al. (2005b) shows that the time it takes for the fluid to traverse the length of a stalactite is of the order of minutes, therefore this is much quicker than seasonal fluctuations to the flow rate, so we can assume that the fluid has coated the stalactite. When the fluid flows down the outside of the stalactite, it has a thickness much thinner than that of the radius of the stalactite. Therefore, Short et al. (2005b) approximates the flow as a gravity driven flow down a flat plate. The flow rate is still calculated by integrating the velocity over the surface area, resulting in

$$Q = \frac{2\pi\tilde{R}\tilde{h}^3}{3\nu} \quad (2.3)$$

where \tilde{R} is the stalactite radius and \tilde{h} is the fluid thickness. Therefore, we can calculate the fluid thicknesses for our example stalactites by solving for \tilde{h}

$$\tilde{h} = \left(\frac{3Q\nu}{2\pi g\tilde{R}} \right)^{\frac{1}{3}} \quad (2.4)$$

Example fluid thickness for the stalactites are given below, with the flow rates converted to m^3/s to make it easier to compare. Here we have picked 3 example radii based on a soda straw stalactite and conical radii from Short et al. (2005b)

| Stalactite | Radius (mm) | 2.5 | 10 | 100 |
|----------------------------------|---------------------------------|-----------------------------------|-----|-----|
| | Flow rate m^3/s | Fluid Thickness (μm) | | |
| Short et al. (2005b) lower bound | 2.8×10^{-9} | 38 | 24 | 11 |
| Short et al. (2005b) upper bound | 2.8×10^{-7} | 180 | 110 | 51 |
| Père Noël cave daily minimum | 2.6×10^{-9} | 37 | 23 | 11 |
| Père Noël cave daily maximum | 1.2×10^{-7} | 130 | 83 | 39 |
| Père Noël cave yearly average | 5.6×10^{-8} | 100 | 65 | 30 |
| Soreq cave 100 ml/day | 1.2×10^{-9} | 28 | 18 | 8 |
| Soreq cave summer minimum | 5.8×10^{-11} | 10 | 7 | 3 |

Table 2.3: Table of approximate fluid thickness for flow rates given in this section

From table 2.3 we see that the fluid thicknesses are usually around $1 \times 10^{-6} - 1 \times 10^{-4}$ m, however most of the flow rates were observed on soda straw stalactites and so may not relate to flow rates on the outside of stalactites. Flow rates greater than $1 \times 10^{-8} \text{ m}^3/\text{s}$ typically occurred in winter months. This period was when less deposition occurred. This could be different on the outside of a stalactite, as the water is immediately in contact with the cave air and so has the carbon dioxide pressure gradient (Paul et al., 2013). The conical stalactite with a straw on its end observed in Soreq Cave (Even et al., 1986) suggests that this flow rate is perhaps too low to sustain conical growth modelled in Short et al. (2005b), with instead the fluid being drawn into a straw as suggested by Maltsev (1999). Therefore, for our model we have decided to use a flow rate of $Q = 1 \times 10^{-9} \text{ m}^3/\text{s}$, that matches the flow rate on the conical stalactite in the Soreq Cave (Even et al., 1986).

From figure 2.3 we can see that increasing the radius decreases the fluid thickness. However, all the fluid thicknesses are of the order 10^{-5} m, which agrees with Short et al. (2005b).

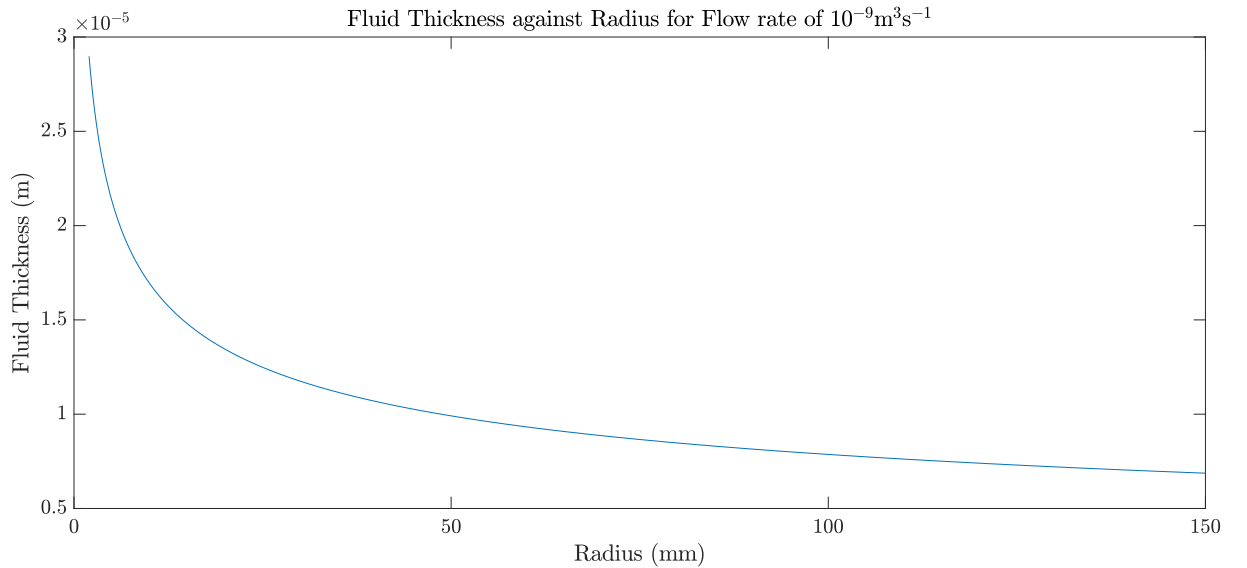


Figure 2.3: How the fluid thickness is affected by the radius of the stalactite according to equation (2.4)

2.2 Hydrodynamic Model

In order to understand the growth of stalactites, we must understand the flow of water down the outside. While conical stalactites do taper towards the point, the angle is very close to vertical (Camporeale, 2017). As soda straw stalactites are cylindrical too, transitioning between the cases will be close to a cylinder. Therefore, we will treat our stalactite as being cylindrical with radius \tilde{R} .

The initial bands observed on soda straws were $2 \mu\text{m}$ which is smaller, but of a similar order of magnitude to that of the fluid thickness. On conical stalactites, these crenulations do grow to amplitudes of the order of millimetres. Therefore, if they do develop from the banding on soda straws, there will be a transitional case where the crenulations will have an amplitude of similar magnitude to the fluid thickness. Even if these crenulations are not the result of this banding, since they end up being larger than the fluid thickness, at some point they must exist with an amplitude similar to that of the fluid thickness.

Due to the symmetry of stalactites, we will model this as an axisymmetric flow. While the radius and crenulations do grow over time, this is on a timescale much slower than the time it takes the fluid to traverse a stalactite (Short et al., 2005b). For this reason we will

assume that the radius R , and the crenulation η are fixed in time.

A sketch of the geometry of the problem is shown in figure 2.4.

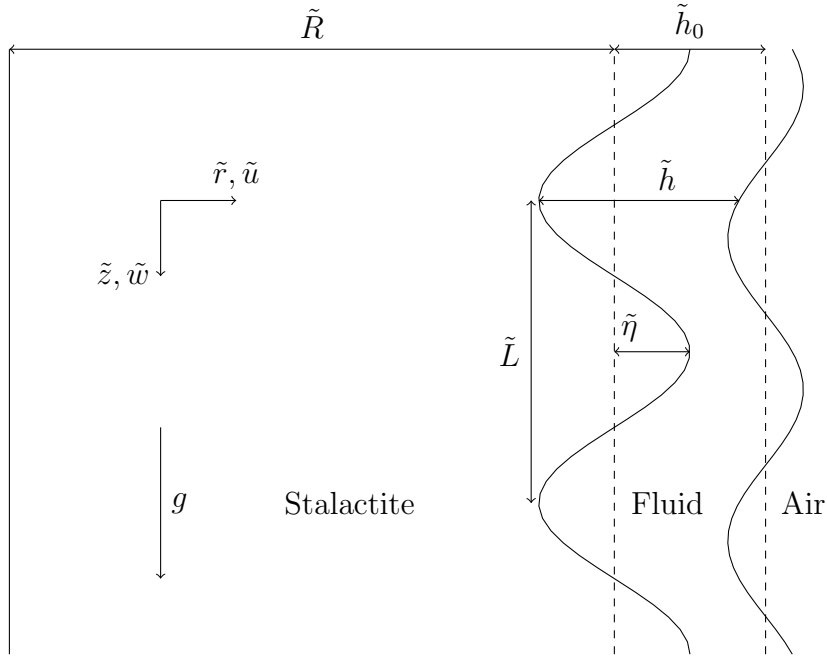


Figure 2.4: Sketch of cross-section of the problem.

For an incompressible fluid with velocity $\tilde{\mathbf{u}} = (\tilde{u}, 0, \tilde{w})$ and pressure \tilde{p} in cylindrical coordinates $\tilde{\mathbf{x}} = (\tilde{r}, \tilde{\theta}, \tilde{z})$, the continuity equation is

$$\frac{\partial \tilde{u}}{\partial \tilde{r}} + \frac{\tilde{u}}{\tilde{r}} + \frac{\partial \tilde{w}}{\partial \tilde{z}} = 0 \quad (2.5)$$

and the Navier-Stokes equations give

$$\frac{\partial \tilde{u}}{\partial \tilde{t}} + \tilde{u} \frac{\partial \tilde{u}}{\partial \tilde{r}} + \tilde{w} \frac{\partial \tilde{u}}{\partial \tilde{z}} = -\frac{1}{\rho} \frac{\partial \tilde{p}}{\partial \tilde{r}} + \nu \left(\frac{\partial^2 \tilde{u}}{\partial \tilde{r}^2} + \frac{1}{\tilde{r}} \frac{\partial \tilde{u}}{\partial \tilde{r}} - \frac{1}{\tilde{r}^2} \tilde{u} + \frac{\partial^2 \tilde{u}}{\partial \tilde{z}^2} \right) \quad (2.6)$$

$$\frac{\partial \tilde{w}}{\partial \tilde{t}} + \tilde{u} \frac{\partial \tilde{w}}{\partial \tilde{r}} + \tilde{w} \frac{\partial \tilde{w}}{\partial \tilde{z}} = -\frac{1}{\rho} \frac{\partial \tilde{p}}{\partial \tilde{z}} + \nu \left(\frac{\partial^2 \tilde{w}}{\partial \tilde{r}^2} + \frac{1}{\tilde{r}} \frac{\partial \tilde{w}}{\partial \tilde{r}} + \frac{\partial^2 \tilde{w}}{\partial \tilde{z}^2} \right) + g \quad (2.7)$$

where ρ is the density, ν is the kinematic viscosity, and g is the acceleration due to gravity.

On the boundary between the stalactite and the fluid we have no flux and no slip,

$$\tilde{u} = 0, \quad \tilde{w} = 0 \quad \text{at} \quad \tilde{r} = \tilde{R} + \tilde{\eta}. \quad (2.8)$$

On the surface of the fluid, where it has an interface with the air, we have the kinematic boundary condition.

$$\tilde{u} = \frac{\partial \tilde{S}}{\partial t} + \tilde{w} \frac{\partial \tilde{S}}{\partial \tilde{z}} \quad \text{at } \tilde{r} = \tilde{S} \quad (2.9)$$

where $\tilde{S} = \tilde{R} + \tilde{\eta} + \tilde{h}$. We also have the tangential and normal stress balances on the free surface ($\tilde{r} = \tilde{S}$), which are

$$2\tilde{S}_{\tilde{z}}(\tilde{u}_{\tilde{r}} - \tilde{w}_{\tilde{z}}) + (1 - \tilde{S}_{\tilde{z}}^2)(\tilde{u}_{\tilde{z}} + \tilde{w}_{\tilde{r}}) = 0 \quad (2.10)$$

and

$$\tilde{p} - \frac{2\mu}{1 + \tilde{S}_{\tilde{z}}^2} \left(\tilde{u}_{\tilde{r}} - \tilde{S}_{\tilde{z}}(\tilde{u}_{\tilde{z}} + \tilde{w}_{\tilde{r}}) + \tilde{S}_{\tilde{z}}^2 \tilde{w}_{\tilde{z}} \right) = \gamma \left(\frac{1}{\tilde{S}(1 + \tilde{S}_{\tilde{z}}^2)^{\frac{1}{2}}} - \frac{\tilde{S}_{\tilde{z}\tilde{z}}}{(1 + \tilde{S}_{\tilde{z}}^2)^{\frac{3}{2}}} \right) \quad (2.11)$$

respectively. Here subscripts denote partial derivatives, $\mu = \rho\nu$ is the dynamic viscosity and γ is the surface tension. This formulation is also used in Craster and Matar (2006).

2.2.1 Scalings

Before we do our scalings, it is useful to note the size of some of the physical parameters of water. These parameters will remain constant for the water flowing down stalactites.

| Parameter | Symbol | Value |
|-----------------------------|----------|--------------------------------------|
| Density | ρ | 997 kg/m ³ |
| Kinematic Viscosity | ν | 1×10^{-6} m ² /s |
| Acceleration due to Gravity | g | 9.81 m/s ² |
| Surface Tension | γ | 7.2×10^{-2} N/m |

Table 2.4: Physical parameters

For this problem, we have five different length scales. In the radial direction we have the radius of our stalactite (\tilde{R}), the crenulation amplitude ($\tilde{\eta}_0$), and the typical fluid

thickness (\tilde{h}_0). In the vertical direction, we have the crementation wavelength (\tilde{L}) and the capillary length \mathcal{L} . The capillary length balances surface tension and gravity through equations (2.7) and (2.11). This results in $\mathcal{L} = \frac{\gamma}{\rho g \tilde{h}_0}$.

For this problem, we will nondimensionalise by using the fluid thickness for \tilde{r} and the crementation wavelength for \tilde{z} . At this point, we will also translate the domain, to make the nondimensional coordinate r be between 0 and $h = \frac{\tilde{h}}{\tilde{h}_0}$. Therefore, we are writing our coordinates as

$$\tilde{r} = \tilde{h}_0 \left(\hat{R} + \hat{\delta} \bar{\eta}(z) + r \right) \quad (2.12)$$

$$\tilde{z} = \tilde{h}_0 \lambda z \quad (2.13)$$

where we have the dimensionless ratios: $\hat{R} = \frac{\tilde{R}}{\tilde{h}_0}$ between the radius and fluid thickness, $\hat{\delta} = \frac{|\bar{\eta}|}{\tilde{h}_0}$ between the crementation amplitude and fluid thickness, and $\lambda = \frac{\tilde{L}}{\tilde{h}_0}$ between the crementation wavelength and fluid thickness. $\bar{\eta}$ is the normalised nondimensional crementation shape.

For this, we will assume the crementation amplitude is similar to the fluid thickness, resulting in $\hat{\delta}$ being $O(1)$. In section 2.1 we found that the wavelength of the crementation was a similar order of magnitude to the radius, varying by at most a factor of 10. While the radius varied between $10^{-3} - 10^{-1}$ m, figure 2.3 showed that the thickness was always around 10^{-5} . This means that $\hat{R} \sim O(10^2 - 10^4)$, with the smaller value relating to soda straw stalactites and the larger relating to conical ones. Similarly, this is true for λ . We therefore rewrite our coordinates as

$$\tilde{r} = \tilde{h}_0 \left(\frac{R}{\epsilon} + \eta(z) + r \right) \quad (2.14)$$

$$\tilde{z} = \tilde{h}_0 \frac{z}{\epsilon} \quad (2.15)$$

where $\epsilon = \frac{1}{\lambda} \ll 1$, $R = \frac{\hat{R}}{\lambda} \sim O(1)$ and $\eta = \hat{\delta} \bar{\eta} \sim O(1)$. Using the small parameter ϵ , we can make an approximation to equations (2.5)-(2.11). The dimensional variables (with

tildes) are related to the nondimensional variables (without tildes) as such

$$\tilde{w} = Ww = \frac{g\tilde{h}_0^2}{\nu}w, \quad \tilde{u} = \epsilon Wu, \quad \tilde{p} = \frac{\gamma}{\tilde{h}_0}p, \quad \tilde{t} = \frac{\tilde{L}}{W}t = \frac{\tilde{h}_0}{\epsilon W}t. \quad (2.16)$$

Noting this change of variables means that the derivatives become

$$\frac{\partial}{\partial \tilde{r}} = \frac{1}{\tilde{h}_0} \frac{\partial}{\partial r} \quad (2.17)$$

$$\frac{\partial}{\partial \tilde{z}} = \frac{\epsilon}{\tilde{h}_0} \left(\frac{\partial}{\partial z} - \eta_z \frac{\partial}{\partial r} \right). \quad (2.18)$$

We can Taylor expand the reciprocal of the radial component

$$\begin{aligned} \frac{1}{\tilde{r}} &= \frac{\epsilon}{\tilde{h}_0} \left(\frac{1}{R + \epsilon(\eta + r)} \right) \\ &= \frac{\epsilon}{Rh_0} \left(1 - \epsilon \frac{\eta + r}{R} + O(\epsilon^2) \right). \end{aligned} \quad (2.19)$$

Using equations (2.14)-(2.19), we can get the nondimensional versions of equations (2.5)-(2.11).

$$u_r + w_z - \eta_z w_r + \epsilon \frac{u}{R} = O(\epsilon^2) \quad (2.20)$$

$$\epsilon u_{rr} - \frac{p_r}{\mathcal{B}} = O(\epsilon^2) \quad (2.21)$$

$$w_{rr} + 1 + \epsilon \left(\frac{w_r}{R} - \frac{1}{\mathcal{B}}(p_z) - \text{Re}(w_t + uw_r + w(w_z - \eta_z w_r)) \right) = O(\epsilon^2) \quad (2.22)$$

$$u = 0, \quad w = 0 \quad \text{at } r = 0 \quad (2.23)$$

$$u = h_t + w(\eta_z + h_z) \quad \text{at } r = h \quad (2.24)$$

$$w_r(h) = O(\epsilon^2) \quad (2.25)$$

$$p(h) = \frac{\epsilon}{R} - \epsilon^2 \left(\frac{\eta + h}{R^2} + \eta_{zz} + h_{zz} \right) \quad (2.26)$$

where $\mathcal{B} = \frac{\tilde{h}_0^2 \rho g}{\gamma}$ is the Bond number and $\text{Re} = \frac{W\tilde{h}_0}{\nu} = \frac{g\tilde{h}_0^3}{\nu^2}$.

To find approximate values for the Bond and Reynolds numbers, we consider the

potential stalactites. For soda straws the radius of the stalactite $R = 2.5$ mm and so if the flow rate is 100 ml/day then fluid thickness is $29 \mu\text{m}$ according to equation (2.4). From this fluid thickness we find $\text{Re} = 0.23$ and $\mathcal{B} = 1.1 \times 10^{-4}$. Soda straw stalactites have a wavelength of around 0.5 mm, which means $\epsilon = 6 \times 10^{-2}$, so here we have roughly $\text{Re} = O(1)$ and $\mathcal{B} = O(\epsilon^3)$.

On the other hand, if we take a conical stalactite of radius 10 cm, with the same flow rate of 100 ml/day, then the fluid thickness is $8.4 \mu\text{m}$. This gives $\text{Re} = 5.7 \times 10^{-3}$ and $\mathcal{B} = 9.6 \times 10^{-6}$. A stalactite with 10 cm radius has been modelled to have a 2 cm crenulation wavelength (Camporeale, 2017), making $\epsilon = 4 \times 10^{-4}$. Here $\mathcal{B} \sim O(\epsilon)$ and $\text{Re} \sim O(\epsilon)$. For conical stalactites however, the amplitude of the crenulations is also significantly larger than the fluid thickness. Therefore, we would expect the curvature of the wall to appear at higher order.

The case where the fluid is a similar thickness to the wall amplitude should occur somewhere between the soda straw stalactite, where the banding is smaller, and the conical one. We will call this the transition stalactite. As this stalactite is somewhere between these 2 cases, we will assume that the Bond number is $\mathcal{B} \sim O(\epsilon^2)$, so we set $\text{Bo} = \frac{\mathcal{B}}{\epsilon^2}$.

If we write the Reynolds number in terms of the flow rate

$$\text{Re} = \frac{3Q}{2\pi\tilde{R}\nu} \tag{2.27}$$

we see that for $\text{Re} = 1$ we require $\frac{Q}{\tilde{R}} = 2 \times 10^{-6}$. This is possible for the $Q = 2 \times 10^{-8}$ m^3/s and $\tilde{R} = 1 \times 10^{-2}$ m, so we will include Re at $O(1)$ for the transition case.

For both cases, equation (2.21) has the pressure term much larger than the biggest velocity term. This means that the pressure is constant with respect to r . From equation (2.26), we see that p_z is $O(\epsilon^2)$. For the soda straw case, this pressure term comes into equation (2.22) at leading order. We will further look at the hydrodynamics for this case in chapter 3. For the transition stalactite, the pressure term is smaller and only comes into equation (2.22) at $O(\epsilon)$. The hydrodynamics based on this scaling for transitioning

stalactites is studied in chapter 4.

While here we have scaled the z direction with respect to the crenulation wavelength, it is also useful to have scaled this instead by the stalactite radius. This would make it clearer to understand the effect changing the wall wavelength will have for a given radius. In this case, we will set $R = 1$ and can set a sinusoidal wall to be of the form

$$\eta = \delta \cos\left(\frac{2\pi z}{L}\right) \quad (2.28)$$

where δ is the amplitude of the wall relative to the fluid thickness and $L = \frac{\tilde{L}}{R}$ is the wavelength of the wall. This makes it easier to see the effect of changing the wavelength, which previously would have to be done by changing several of the other parameters (R, Bo, ϵ).

2.3 Crenulation Shapes

In order to model the crenulations, we will look at three possible shapes. These are sinusoidal, step and sawtooth. For our crenulations, we will assume periodicity. This makes a sinusoidal wall a good place to start, as we can write any periodic function as a Fourier series.

$$\eta = \frac{a_0}{2} + \sum_{n=1}^N \left[a_n \cos\left(\frac{2\pi nx}{L}\right) + b_n \sin\left(\frac{2\pi nx}{L}\right) \right]. \quad (2.29)$$

Steps and sawtooths could be used to model the banding found on soda straw stalactites (Huang and Fairchild, 2001; Huang et al., 2001). Alternatively, they could be used to model plant growth or erosion. These could all be the initial wall perturbation that leads to the growth of the crenulations (Vesipa et al., 2015; Camporeale, 2017).

In order to model these shapes, we will use \tanh as a smoothing function, as is done in

Tseluiko et al. (2008). Our step function will be modelled as

$$\eta = \delta \left[\tanh \left(\frac{2z - L + \ell L}{2\xi L} \right) - \tanh \left(\frac{2z - L - \ell L}{2\xi L} \right) - 2\ell \right]. \quad (2.30)$$

Here δ and L define the amplitude and wavelength of the crenulation as before. Additionally, we have the parameters: ℓ , which is the ratio between the width of the top of the step and the wavelength; and ξ , which controls the steepness of the step. As $\xi \rightarrow 0$ the corners of the step become right angles. The shift of $2\delta\ell$ is done so that the wall has 0 mean ($\int_0^L \eta dz = 0$).

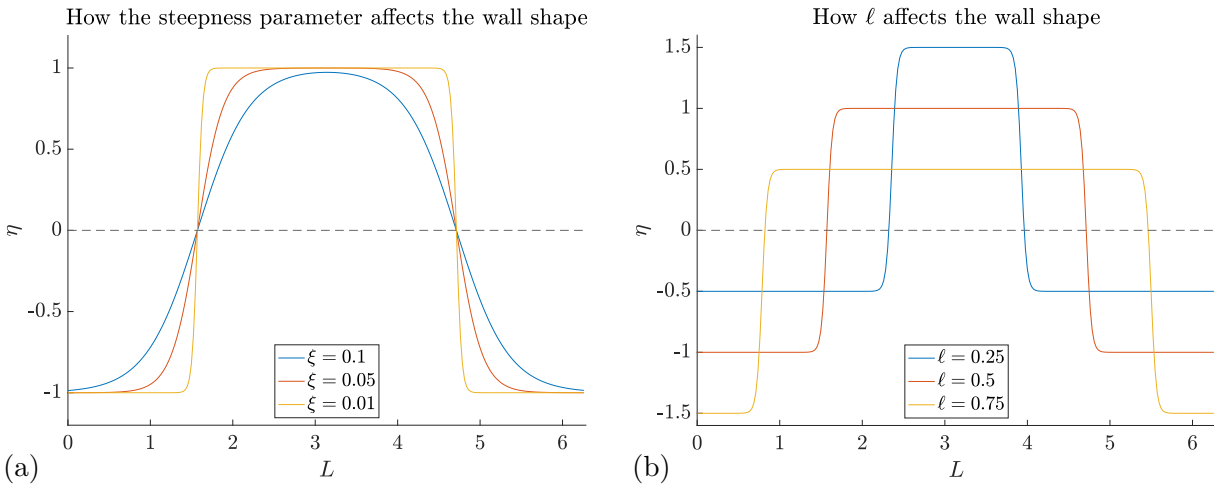


Figure 2.5: Different shapes of steps used as the wall. (a) shows how decreasing the steepness parameter makes the step approach a right angle. (b) shows steps of different widths.

Figure 2.5 shows how ℓ and ξ affect the wall shape. For $\ell > 0.5$ we can view this as being a flat wall with a mound on it, and $\ell < 0.5$ can be viewed as having a trench.

Similarly, we can model our sawtooth using this step

$$\eta = \sigma_1 \delta \left[\frac{2z - L(1 - \sigma_2 \ell)}{2\ell L} \right] \left[\tanh \left(\frac{2z - L + \ell L}{2\xi L} \right) - \tanh \left(\frac{2z - L - \ell L}{2\xi L} \right) \right] - \sigma_2 \delta \ell. \quad (2.31)$$

Again, ξ and ℓ are the steepness parameters and the proportion of the wall that is a sawtooth. $\sigma_1, \sigma_2 \in (-1, 1)$, are parameters to determine the direction of the slope, and whether the step is before or after the slope. Here we have $L(1 - \ell)$ of the wall being flat.

As $\ell \rightarrow 1$ we will have the normally defined sawtooth. However, for the cases $\ell = 1$, we would lose the smoothing effect of the tanh. Therefore, we will generally keep $\ell < 0.9$.

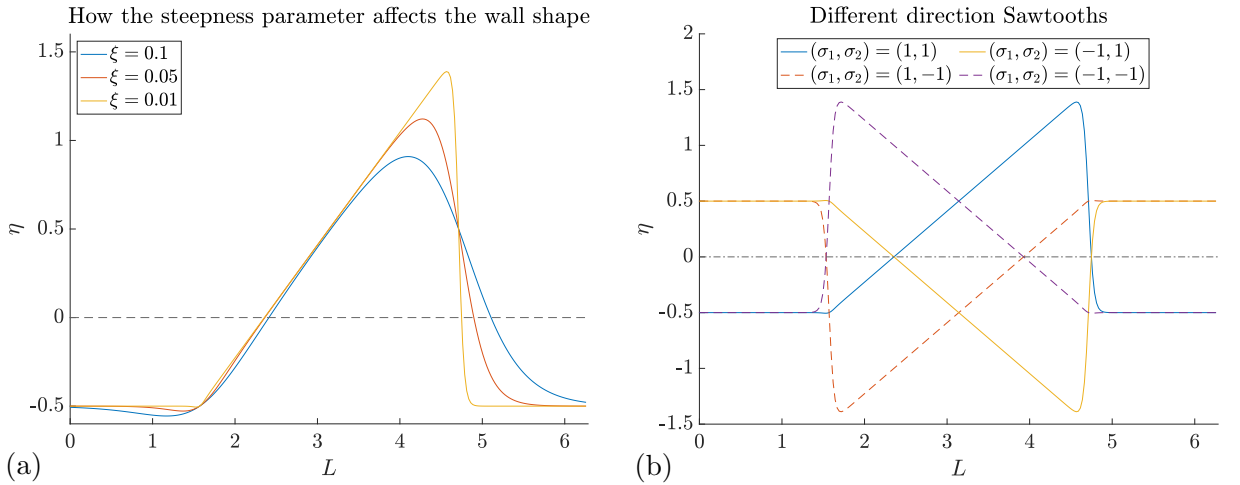


Figure 2.6: Different shapes of sawtooth used as the wall. (a) shows how decreasing the steepness parameter makes the point of the saw much sharper. (b) shows the different configurations of saw we have.

Figure 2.6 shows the different shapes of sawtooths we have. Subfigure (a) similarly to the step plot shows how the smaller ξ is, then the steeper the point of the saw is. In (b) the fluid is flowing from left to right. These walls in the order of the legend are then viewed as: the fluid flowing down a slope before a drop; the fluid dropping down a step before flowing down a slope; the fluid underhanging a slope before a step-up; and the fluid stepping up before underhanging a slope.

2.4 Growth of Stalactites

As highlighted by Short et al. (2005b) the growth of a stalactite is much slower than the time it takes for the fluid to transverse it. The time it takes for the fluid to traverse one crenulation $t_t = \frac{\lambda}{W} \sim 10$ s. Meanwhile, assuming a growth rate v of 1 cm/century, the time it takes for a stalactite to grow by a fluid thickness is $t_g = \frac{\tilde{h}}{v} \sim 10^6$ s. As this is much slower than the traversal times, Short et al. (2005b) separates the timescales and considers a stagnant fluid layer.

Because of the different timescales, Vesipa et al. (2015); Camporeale (2017) make use of a quasi-steady approximation. Here they find the steady state fluid thickness to determine the stalactite growth. However, if the fluid does not settle into a steady state, the dynamics of the fluid may yet affect the growth. Therefore, a time averaged fluid thickness will be considered.

The growth of the stalactite is dependent on the amount of calcite deposited on the surface. This can be viewed as the flux of calcium concentration at the surface. This deposition not only causes the crenulations to grow, but also the radius of the stalactite. Overall we have

$$\tilde{R}_t + \tilde{\eta}_t = -\rho_c D \frac{\partial \tilde{c}}{\partial \tilde{r}} \Big|_{\tilde{R} + \tilde{\eta}} \quad (2.32)$$

where ρ_c is the molar volume of calcite, D is the diffusion coefficient for calcium and \tilde{c} is the concentration of calcium ions in the fluid. The time it takes for the ions to diffuse across the wavelength is $t_d = \frac{\tilde{h}^2}{D} \sim 0.1$ s, which is faster than the fluid transverses. Therefore, the concentrations should effectively be constant across the fluid.

The growth is however limited by the production of carbon dioxide (Plummer et al., 1978; Buhmann and Dreybrodt, 1985). Therefore, to model the growth, we must also consider the carbon dioxide concentration. The concentrations of calcium and carbon dioxide in the fluid layer can be modelled by the convection-diffusion-reaction equations

$$\frac{\partial \tilde{c}_i}{\partial t} + \tilde{\mathbf{u}} \cdot \tilde{\nabla} \tilde{c}_i = D_i \tilde{\nabla}^2 \tilde{c}_i + \tilde{r}_i \quad (2.33)$$

where \tilde{c}_i denotes the concentration, with the subscripts $i = 1, 2$ referring to calcium and carbon dioxide respectively. $\tilde{\mathbf{u}}$ is the velocity of the fluid, D_i denotes the diffusion coefficients and \tilde{r}_i is the reaction rate. For this problem, the conversion of carbon dioxide to bicarbonate is the rate limiting process (Kaufmann and Dreybrodt, 2007). The other chemical reactions of the system occur much faster, and so they can be assumed to be in equilibrium (Buhmann and Dreybrodt, 1985). Therefore, the reaction rate for calcium is

$\tilde{r}_1 = 0$, and the reaction rate for carbon dioxide

$$\tilde{r}_2 = k_-[\text{HCO}_3^-] - k_+\tilde{c}_2, \quad (2.34)$$

where k_{\pm} are the reaction rates.

While the concentrations may vary seasonally, we will consider growth based on mean concentrations so that the temporal derivatives of the concentration are neglected. This is similarly done by Short et al. (2005b); Vesipa et al. (2015). While the concentration of the calcium concentration should deplete further down the stalactite due to the calcium being deposited, the concentration gradient is small and the effect over one wavelength is negligible (Vesipa et al., 2015). Therefore, we will consider the z dependence in the concentrations to be caused by the wall shape. In order to model the growth of the stalactite, we will at each time step compute the fluid thickness and velocities for the given radius and wall shape. From this we can calculate the chemical concentrations and hence the calcite flux. This allows us to grow the radius and wall shape. With the new radius and wall shape, we again calculate the new fluid properties, so we can calculate the new calcite flux and so on. This is explored further in chapter 5.

2.5 Computational Methods

For these problems, our spatial coordinate $z \in [0, L]$. In order to solve the equations numerically, we discretise z so that

$$z_i = \frac{(i-1)L}{n} \quad (2.35)$$

where n is the number of points and $i \in \{1, 2, \dots, n+1\}$. As our domain is periodic, $z_1 = z_{n+1}$. The fluid thickness at a point is denoted $h_i = h(z_i)$. For the spatial derivatives, we initially finite differences, however as our domain is periodic, we then used a pseudo-spectral method to improve the precision. We used second order finite centred finite

differences,

$$h'_i = \frac{n}{2L}(h_{i+1} - h_{i-1}) \quad (2.36)$$

$$h''_i = \frac{n^2}{L^2}(h_{i+1} - 2h_i + h_{i-1}) \quad (2.37)$$

$$h'''_i = \frac{n^3}{2L^3}(h_{i+2} - 2h_{i+1} + 2h_{i-1} - h_{i-2}) \quad (2.38)$$

$$h''''_i = \frac{n^4}{L^4}(h_{i+2} - 4h_{i+1} + 6h_i - 4h_{i-1} + h_{i-2}). \quad (2.39)$$

For the spatial derivatives, we used a pseudo-spectral method, following the steps of Alexander (2021). Here, we make use of MATLAB function `fft` to perform a fast Fourier transform, resulting in $\hat{h}_k = \text{fft}(h_k)$. In Fourier space the m^{th} derivative becomes

$$\hat{h}_k^{(m)} = (ik)^m \hat{h}_k. \quad (2.40)$$

This is then converted back into real space by using MATLAB function `ifft`.

For these problems, we need to calculate up to the fourth derivative, as seen by equations (1.2)-(1.5). For the wall and the initial condition we will mostly be using cosines, so if we have a wall $\eta = \cos z$, this results in $\eta_{zzzz} = \cos z$. We can test the accuracy of the numerical methods based off this, with the error defined as

$$E = \frac{1}{n} \left(\sum_{i=1}^n (\eta_{zzzz} - \eta_z)_i^2 \right)^{\frac{1}{2}}, \quad (2.41)$$

where again n is the number of points and $_i$ denotes the value at z_i .

Figure 2.7 shows the error for the different schemes. For both finite difference and pseudo-spectral, we see that increasing the number of grid points reduces the error. Increasing the number of grid points however also slows down the integration. In the finite difference case, the error increases again after 2^{10} points. From this figure, we see that the finite difference has a minimum error of 10^{-7} at $n = 2^{10}$. Meanwhile the pseudo-spectral error is always less than that of the machine error. For this reason we decided to use

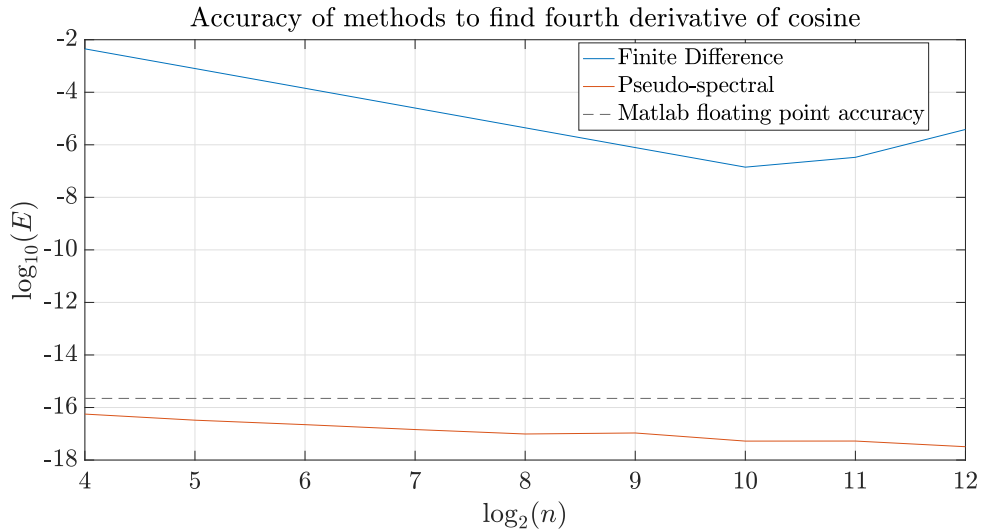


Figure 2.7: Numerical error of $(\cos z)_{zzzz}$ for the different differentiation methods, with 2^n points.

pseudo-spectral for the differentiation, with $n = 256$ grid points chosen as a compromise between speed and error.

To solve our equations, we made use of several MATLAB functions. For the steady state equations or other equations which can be written as

$$\mathbf{F}(h) = 0, \quad (2.42)$$

with h the fluid thickness, we use `fsolve`. `fsolve` takes this vector of equations and an initial guess to find the solution h . Here we can write the spatial derivatives of h as functions of h using the pseudo-spectral method outlined above. This outputs a vector for the fluid thickness h that satisfies the equations.

Time integration is done using MATLAB function `ode15s`. This takes the input F , where

$$h_t = F(t, h) \quad (2.43)$$

and an initial guess for the fluid thickness h . This solver was chosen as the equations we are solving are stiff. Here the fluid thickness at each time step is outputted.

For the Floquet analysis, we can cast the equation into the form

$$A\mathbf{h} = \omega\mathbf{h} \tag{2.44}$$

where A is a matrix, ω are eigenvalues, and \mathbf{h} the eigenvectors of the fluid thickness. We can then use MATLAB function `eig`, which takes the input A and outputs the eigenvalues ω and corresponding eigenvectors h .

Code written for this thesis can be found in the GitHub repository: <https://github.com/srh18/PhD-work>. The class `shape_solveh.m` was created to find and analyse solutions for different parameters.

Chapter 3

Hydrodynamics 1: Inertialess Flow

3.1 Introduction

Thin films flowing down cylinders with topography has applications to the geophysical world in the cases of icicles (Ueno, 2007; Ueno et al., 2009) and stalactites (Short et al., 2005b; Vesipa et al., 2015; Camporeale, 2017). However, these tend to model the hydrodynamics as a fluid flowing down a flat inclined plane, which could be missing some of the effects that the true geometry has on their growth.

In this chapter, we will be building on gravity driven thin film flows down cylinders, which were previously studied by Kalliadasis and Chang (1994); Craster and Matar (2006); Frenkel (1992). In these works, the surface tension also works to drive the flow. To these models, we will introduce surface topography, with an amplitude of similar size to the fluid thickness.

Flow over topography has previously been studied down an inclined plane (Tseluiko et al., 2013), where we see the effect of the topography in the surface tension terms. Experimentally, work has been done on the effects of flow over topography down an inclined pipe (Kuehner et al., 2021).

3.2 Governing Equations

For this problem, we will be considering a thin film flow under gravity down a cylinder that has a long wave disturbance to its surface. The cylinder and its disturbance are fixed in time. The amplitude of this disturbance is of the same order as the fluid thickness. Continuing on from section 2.2, where we have nondimensionalised the Navier Stokes equation (2.5)-(2.11) by using the scalings (2.14)-(2.16). This resulted in the nondimensional equations (2.20)-(2.26). As discussed in section 2.2, in this chapter we will work with a scaled Bond number $\text{Bo} = \frac{\mathcal{B}}{\epsilon^3} = \frac{\rho h_0^2 g}{\gamma \epsilon^3}$. We will also scale the pressure term using

$$P = \frac{\rho h_0 g}{\epsilon}, \quad (3.1)$$

so that the pressure terms appear more clearly at leading order in the momentum equations (2.21)-(2.22).

To leading order the equations (2.20)-(2.26) have now become

$$u_r + w_z - \eta_z w_r = 0 \quad (3.2)$$

$$p_r = 0 \quad (3.3)$$

$$w_{rr} - p_z + 1 = 0 \quad (3.4)$$

with boundary conditions

$$u(0) = w(0) = 0 \quad (3.5)$$

$$u(h) = h_t + w(h)(h_z + \eta_z) \quad (3.6)$$

$$w_r(h) = 0 \quad (3.7)$$

$$p(h) = -\frac{1}{\text{Bo}} \left(-\frac{1}{\epsilon R} + \frac{\eta + h}{R^2} + \eta_{zz} + h_{zz} \right). \quad (3.8)$$

From equation (3.3) we find that the pressure is a constant in r and therefore is equal to that given by the tangential stress balance (3.8). For the velocities we require the

pressure gradient, so differentiating with respect to z results in

$$p_z = -\frac{1}{\text{Bo}} \left(\frac{\eta_z + h_z}{R^2} + \eta_{zzz} + h_{zzz} \right) \quad (3.9)$$

From this we see that the pressure gradient comes from the balance between surface tension caused by the curvature of the cylinder and of that caused by the curvature of the wall.

We can then calculate w from equation (3.4), with the boundary conditions (3.5), (3.7), resulting in

$$w = (p_z - 1) \left(\frac{r^2}{2} - rh \right) \quad (3.10)$$

Substituting this into equation (3.2), using the no flux boundary condition (3.5), we get

$$u = \eta_z w - p_{zz} \left(\frac{r^3}{6} - \frac{r^2 h}{2} \right) + (p_z - 1) \frac{r^2 h_z}{2}. \quad (3.11)$$

Applying the velocities (3.10)-(3.11) into the kinematic condition (3.6) we get an evolution equation for the fluid thickness.

$$h_t + \frac{\partial}{\partial z} \left(\frac{h^3}{3} (1 - p_z) \right) = 0. \quad (3.12)$$

This shows that the fluid thickness is driven by gravity balanced by the surface tension found in the pressure gradient. Writing out the pressure gradient fully by substituting in equation (3.9), we get the equation

$$h_t + \frac{\partial}{\partial z} \left(\frac{h^3}{3} \left(1 + \frac{1}{\text{Bo}} \left(\frac{h_z + \eta_z}{R^2} + h_{zzz} + \eta_{zzz} \right) \right) \right) = 0. \quad (3.13)$$

For the smooth cylinder case, $\eta = 0$, this is the same as the equation reported in Kalliadasis and Chang (1994). For flow over topography on an inclined plane with no

inertia, Tseluiko et al. (2013) derives the equation

$$h_t + \frac{\partial}{\partial x} \left(\frac{2}{3} h^3 - \frac{2 \cot \theta}{3} h^3 (h + \eta)_x + \frac{1}{3 \text{Bo}} h^3 (h + \eta)_{xxx} \right), \quad (3.14)$$

where x is the coordinate in the direction of flow, and θ is the angle of the plane from the horizontal. We see that the term we have due to the azimuthal curvature is equivalent to that of their term due to the z -component of gravity. Due to the positive sign we have in our equation, this would be in the case where their angle $\theta > \frac{\pi}{2}$, describing fluid flowing down an overhanging wall.

3.3 Steady States

We can find steady states of the system by setting $h_t = 0$. This allows us to integrate equation (3.13) with respect to z to get

$$q = \frac{h^3}{3} \left(1 + \frac{1}{\text{Bo}} \left(\frac{h_z + \eta_z}{R^2} + h_{zzz} + \eta_{zzz} \right) \right) \quad (3.15)$$

where q is the constant flow rate. For the smooth cylinder case, $h = 1$ is a trivial solution of (3.15), which has the flow rate $q = \frac{1}{3}$.

3.3.1 Small amplitude wall

We consider the amplitude of the wall to be small, so $|\eta| = \delta \ll 1$. For this problem, we will assume $\delta > \epsilon$ so that the $O(\delta)$ terms are larger than the $O(\epsilon)$ terms. Due to the small wall perturbation, we expect this to cause a perturbation to the fluid thickness of a similar size. Setting $h = 1 + \delta \hat{h}$ and $\eta = \delta \hat{\eta}$, substituting into equation (3.15) and looking at the $O(\delta)$ terms, results in the equation

$$\hat{h}_{zzz} + \frac{\hat{h}_z}{R^2} + 3 \text{Bo} \hat{h} = -\frac{\hat{\eta}_z}{R^2} - \hat{\eta}_{zzz}. \quad (3.16)$$

In the case where we have a sinusoidal wall of the form $\hat{\eta} = \cos kz$, where $k = \frac{2\pi}{L}$, we can find a solution to (3.16) of the form

$$\hat{h} = A \cos(kz - \theta) \quad (3.17)$$

where

$$\tan \theta = \frac{3 \text{Bo} L^3 R^2}{2\pi(4\pi^2 R^2 - L^2)} \quad (3.18)$$

$$A = -\cos \theta. \quad (3.19)$$

For a positive amplitude we require $\cos \theta < 0$, hence the phase shift must be $\frac{\pi}{2} < \theta < \frac{3\pi}{2}$. There is a discontinuity in the phase shift at $L = 2\pi R$. However, at this wavelength, the wall terms cancel out. The wavenumber in this case $k = \frac{1}{R}$ and so

$$\frac{\eta_z}{R^2} + \eta_{zzz} = -\frac{k \sin k}{R^2} + k^3 \sin k = 0. \quad (3.20)$$

In this case we simply have the same equation as if there was no wall. Looking at the wavelengths just before and after, by setting $L = 2\pi R \pm \epsilon$ where $\epsilon \rightarrow 0$, we find that $L = 2\pi R - \epsilon$ gives $\theta \rightarrow \frac{3\pi}{2}$ and $L = 2\pi R + \epsilon$ gives $\theta \rightarrow \frac{\pi}{2}$. Both of these result in an amplitude tending to 0, as expected from the smooth cylinder case.

It is also interesting to note that as $L \rightarrow 0$ we would get $\tan \theta \rightarrow 0$, meaning that $\theta = \pi$. In this case, the fluid thickness disturbance is out of phase with the wall. It also has $A = 1$ so that if you looked at the surface of the fluid it would appear cylindrical. Looking at increasing $L > 2\pi R$, the phase shift and the amplitude will initially increase slightly, however the limit $L \rightarrow \infty$ again means that $\theta \rightarrow \frac{\pi}{2}$. This also tells us that the fluid disturbance is never larger than that of the wall disturbance as $A \leq 1$.

Figure 3.1 shows this more clearly as we see the resulting amplitudes and phase shift for $R = 0.5, 1, 2$. The Bond number here is set to 1 as it only appears as a scaling factor for $\tan \theta$. From subfigure (a) we see that for $L < 2\pi R$, the amplitude decays from 1 to 0.

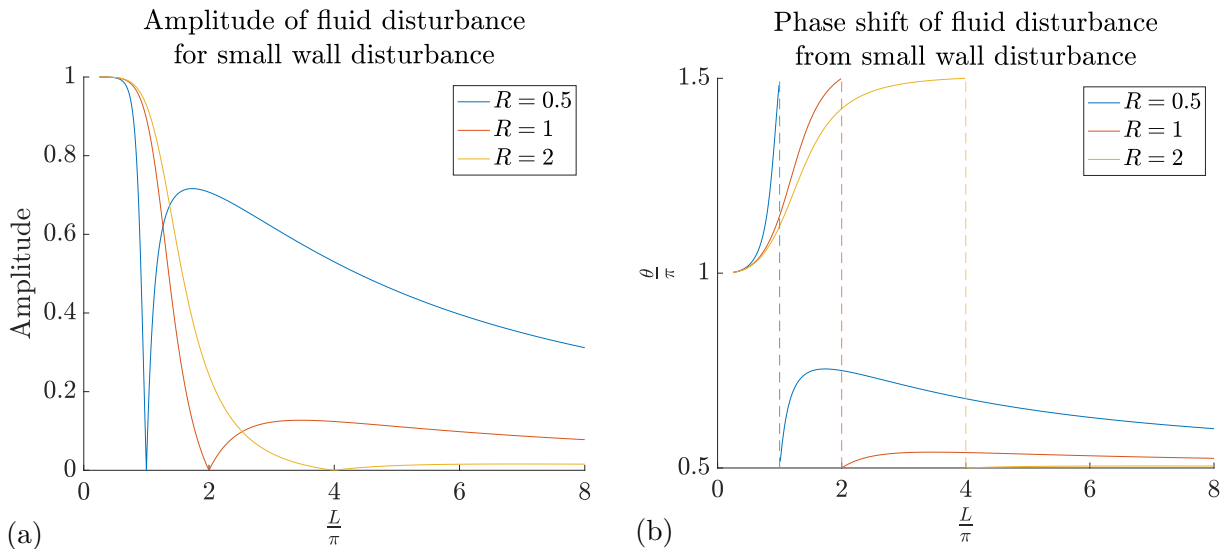


Figure 3.1: (a) The amplitude of the fluid disturbance against the wavelength for $R = 0.5, 1, 2$. (b) The phase shift of the fluid disturbance from the wall disturbance for $R = 0.5, 1, 2$.

For $L > 2\pi R$ on the other hand the amplitude remains a lot smaller, reaching only around a tenth of the wall amplitude for $R = 1$. It can also be seen in these cases that the wall amplitude decreases with increasing radius. Subfigure (b) shows the phase shift from the wall disturbance. We can see that for small wavelengths the fluid disturbance is out of phase with the wall as expected. The phase shift increases to $\theta = \frac{3\pi}{2}$ as $L \rightarrow 2\pi R$ and then drops to $\theta = \frac{\pi}{2}$. For $L > 2\pi$ the phase shift increases up until some point and slowly decreases again.

3.3.2 Numerical steady state solutions

For larger amplitude walls, we solve the equation numerically using MATLAB's function `fsolve`, as outlined in section 2.5. The domain is discretised into 256 grid points, with periodic boundary conditions. The derivatives are calculated using a pseudo spectral method. Steady state solutions can be found by imposing an initial flow rate, however to make it easier to compare to the dynamical solutions we have decided to fix the mass of the fluid. The mass can be calculated from the volume integral of the density. Back in the

dimensional variables this is

$$\tilde{m} = \int_0^{2\pi} \int_0^{\tilde{L}} \int_{\tilde{R}+\tilde{\eta}}^{\tilde{R}+\tilde{\eta}+\tilde{h}} \rho r \, dr \, dz \, d\theta. \quad (3.21)$$

At leading order this is now

$$\tilde{m} = 4\pi\rho \frac{R\tilde{h}_0^3}{\epsilon^2} \int_0^L h(z) \, dz. \quad (3.22)$$

So here we have the dimensional constant for mass $M = 4\pi\rho \frac{\tilde{h}_0^3}{\epsilon^2}$, where $\tilde{m} = Mm$. This gives

$$m = R \int_0^L h \, dz. \quad (3.23)$$

For a smooth cylinder which has the solution $h = 1$, this gives us that the $m = RL$.

As we seek solutions that have mean thickness of 1 independent of the wavelength of the wall, we have imposed the condition

$$\frac{1}{L} \int_0^L h \, dz = 1. \quad (3.24)$$

The flow rate q can be calculated as a result of this. While this is done to make it easier to compare numerical results, in an experimental set-up it may be easier to alter the flow rate.

As well as the flow rate q the results can be characterised by the norm

$$\|h_0\|_2 = \sqrt{\frac{1}{L} \int_0^L h_0^2 \, dz}. \quad (3.25)$$

For the smooth cylinder case, this gives $\|h_0\|_2 = 1$ and the small amplitude wall (3.17) gives

$$\|h_0\|_2 = \sqrt{1 + \frac{\delta^2 A^2}{2}}. \quad (3.26)$$

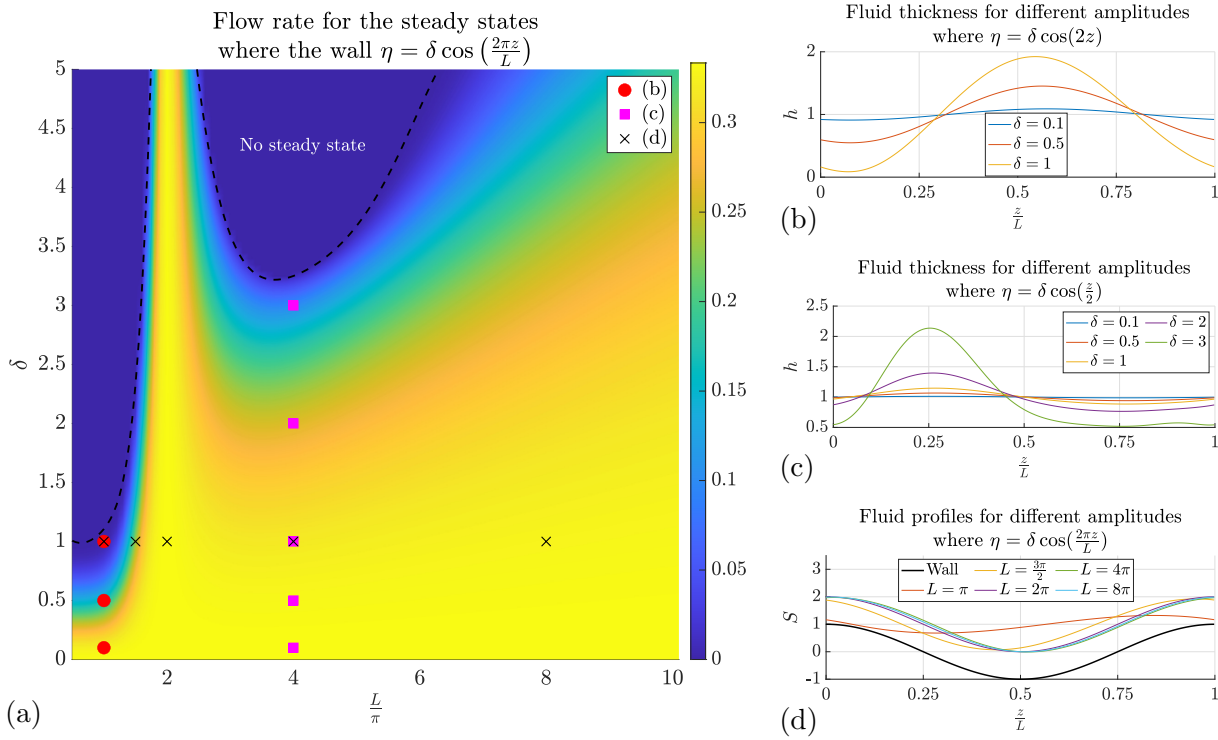


Figure 3.2: (a) Plot showing how the flow rate is affected by walls of different wavelengths and amplitudes. (b) and (c) show the fluid thickness for wavelengths of $L = \pi$ and $L = 4\pi$ respectively. (d) shows the fluid profile in relation to the wall for walls of amplitude $\delta = 1$.

From figure 3.2(a) we see how the flow rate is affected by different shaped walls. For these solutions, we have set the radius $R = 1$ and the Bond number $\text{Bo} = 1$. We see that increasing the amplitude decreases the flow rate. For the smooth cylinder case $\delta = 0$, we have $q = \frac{1}{3}$ and this is also true for the case where $L = 2\pi$ as this is where the wall terms cancel. Increasing the wavelength causes the flow rate to decrease more slowly. In the regions labelled “no steady state” the code did not converge. As we tend towards these regions, we see that the flow rate tends to 0. Solutions on the boundary have the fluid dewetting from the wall. This is because we have fixed the volume of the fluid to be L and so for walls where $\delta > 1$ we have the amplitude of the wall larger than the mean thickness of the fluid, resulting in the wall terms having a larger effect on the pressure gradient.

Figures (b) and (c) show the fluid thicknesses where the different pressure terms dominate. In (b) we have a wavelength of $L = \pi$ meaning the axial curvature term dominates the flow. In this scenario, we see that the maximum thickness is slightly downstream of the trough in the wall, and the amplitude of the oscillation of the fluid is

similar to that of the amplitude of the wall. This is in contrast to what we see in figure (c). Here the wavelength is $L = 4\pi$, where the azimuthal term dominates. Here we see the maximum fluid thickness occurring roughly halfway between the peak and the trough, with the amplitude of oscillation of fluid thickness only around 0.2 that of the amplitude of the wall. These results agree with the phase shift and amplitude suggested by the small amplitude wall (3.17). For the $\delta = 3$ we see the non-linearity appear, with a second smaller maximum around $z = 0.9L$.

Figure (d) shows the fluid profiles compared to the walls which they flow over for different wavelengths. Here the wall always has amplitude $\delta = 1$. We see that for the wavelengths $L > 2\pi$ that the fluid appears like it is just following the wall shape. This is because the amplitude of the fluid thickness is small. The $L = 2\pi$ case is included here, which has thickness $h = 1$ everywhere. This allows us to see that in the longer wavelength cases, the fluid is slightly thicker after the peak in the wall and slightly thinner just before the peak. This is in contrast to the $L < 2\pi$ cases, where the fluid can be viewed as trying to fill the wall trough, with the fluid thickest before the wall peak and thinnest just after.

3.3.3 Alternative wall shapes

We can also numerically calculate the fluid thickness for wall shapes that are not sinusoidal by using equation (3.15). We will first look at the steady state fluid thickness based on a wall that is a step, as in equation (2.30), described in section 2.3. Here we have taken $\xi = 0.01$. This makes the η_{zzz} term in (3.15) very large at the step up and down, where it is around $\frac{1}{L^3\xi^3}$. If this term is too large the code fails to converge, so to compensate for the large derivatives, we must also impose that the wall has a small amplitude or a long wavelength.

Figure 3.3 shows how a step wall affects the fluid flow. (a) shows the fluid profile and from this we can see that the fluid thins just before a bump, and thickens just before a drop. These results can also be seen in other thin film flows over steps (Kalliadasis et al., 2000; Tseluiko et al., 2008, 2013). This can also be seen in the fluid thickness's difference

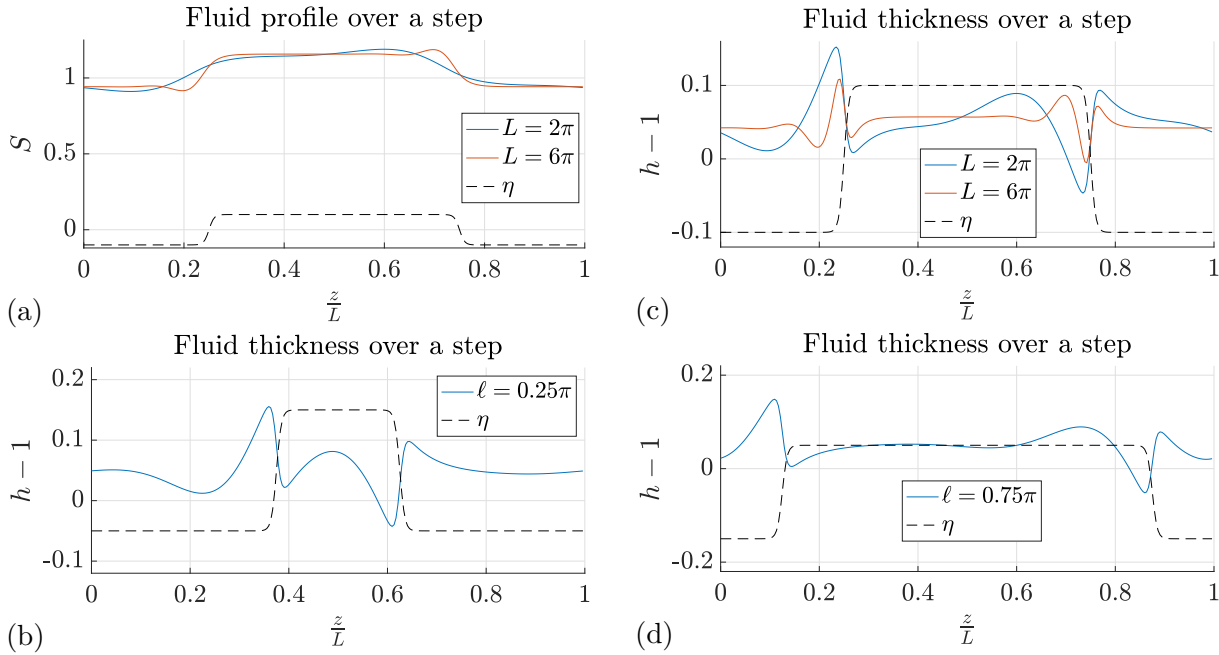


Figure 3.3: Steady state fluid thickness over a wall step. (a) and (c) show how different wavelengths affect the fluid thickness, with the step up and down being equal lengths. (a) shows the fluid profile, whereas (c) shows the difference of the fluid thickness from the mean. (b) has a narrow step up and (d) a narrow step down and are both with wavelength $L = 2\pi$.

from the mean, with it being negative before the step-up and positive just after. Increasing the wavelength makes these disturbances seem narrower, however if you factor L back in they are of a similar width. From (c) we additionally see the fluid thickening just before the step-up and thinning before the step-down. This has the effect of smoothing the fluid surface. From (b) we have narrowed the step-up, and we find that the fluid still thickens around 1 unit before the drop. For (d) we have narrowed the step-down, and we can see that the fluid is thinning about 1 unit before the step-up. From (b) and (d) where we have longer flat sections of the wall, we see that the fluid thickness remains close to the mean.

Instead of treating the wall as a step, we can model our wall as a sawtooth function defined by equation (2.31). In these cases, instead of both a step-up and a step-down, we simply have one or the other. Figure 3.4 shows how a sawtooth wall can affect the fluid flow. (a) shows the fluid profile, with (b) showing the corresponding fluid thickness. Here we see that the fluid thickness is mostly unaffected by the slope, apart from a small kink where the slope starts. This acts to smooth the transition as seen in the fluid profile.

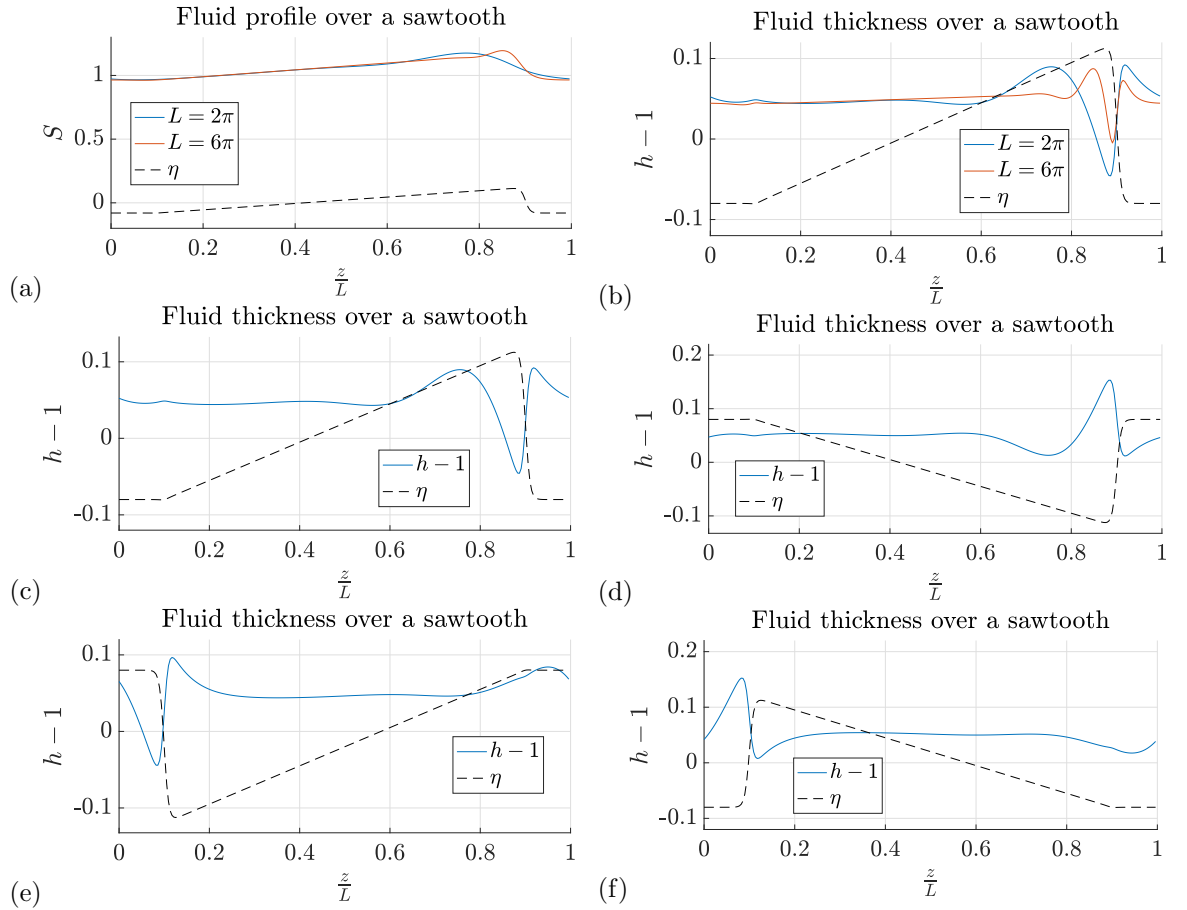


Figure 3.4: Steady state fluid thickness over a wall shaped like a sawtooth. (a) and (b) show how different wavelengths affect the fluid thickness. (a) shows the fluid profile, whereas (b) shows the difference of the fluid thickness from the mean. (c)-(f) show mean fluid thicknesses for different directions of step, all with wavelength $L = 2\pi$. In all cases $\ell = 0.8$.

Comparing the fluid thickness in (b) with that of the step-down shown in figure 3.3(b), we see that this produces the same results. Figures (c)-(f) shows the fluid thickness for the four possible sawtooth configurations. We again see that these can be used to model just a step-down in (c) and (e), and just a step-up for (d) and (f).

3.4 Stability Analysis

We can perform linear stability analysis by considering a small perturbation away from the smooth cylinder case

$$h = 1 + H e^{ikz - i\omega t} \quad (3.27)$$

where $|H| \ll 1$. Applying this to equation (3.13), with $\eta = 0$ results in

$$i\omega = ik + \frac{1}{3\text{Bo}} \left(k^4 - \frac{k^2}{R^2} \right). \quad (3.28)$$

Separating into real and imaginary parts, so that $\omega = \omega_r + i\omega_i$, this gives

$$\omega_r = k \quad (3.29)$$

$$\omega_i = \frac{1}{3\text{Bo}} \left(\frac{k^2}{R^2} - k^4 \right). \quad (3.30)$$

Therefore we are stable if $k < \frac{1}{R}$ and unstable for $k > \frac{1}{R}$. This means that $L = 2\pi R$ lies on the neutral stability curve.

Note that if the wall is

$$\eta = \cos\left(\frac{2\pi z}{L}\right) \quad (3.31)$$

then

$$\frac{\eta_z}{R^2} + \eta_{zzz} = 0 \quad (3.32)$$

at $L = 2\pi R$. Therefore equation (3.13) is identical in the case where $\eta = \cos\left(\frac{z}{R}\right)$ to that with $\eta = 0$. This means that in this case we also have a change of stability at $L = 2\pi R$. As the equations coincide at the point where the stability changes, we may expect the stability to change at this wavelength for any wall disturbance.

Including the wall term means that our steady state solution is no longer a constant. Assuming our solution to be periodic, we can apply Floquet Theorem. Here we consider a small perturbation from the steady state of the form

$$h = h_0(z) + H(z)e^{-\omega t} \quad (3.33)$$

where $|H(z)| \ll |h_0|$. Applying this to equation (3.13) results in

$$\omega H = \frac{\partial}{\partial z} \left(\frac{1}{\text{Bo}} h_0^3 \left(\frac{H_z}{R^2} + H_{zzz} \right) + h_0^2 H \left(1 + \frac{1}{\text{Bo}} \left(\frac{h_{0z} + \eta_z}{R^2} + h_{0zzz} + \eta_{zzz} \right) \right) \right) \quad (3.34)$$

We now solve this numerically by turning this into an eigenvalue problem. This is done by using finite difference to write the derivatives in terms of H , as discussed in section 2.5. The eigenvalue problem is then solved using MATLAB's function `eig`, which gives us the

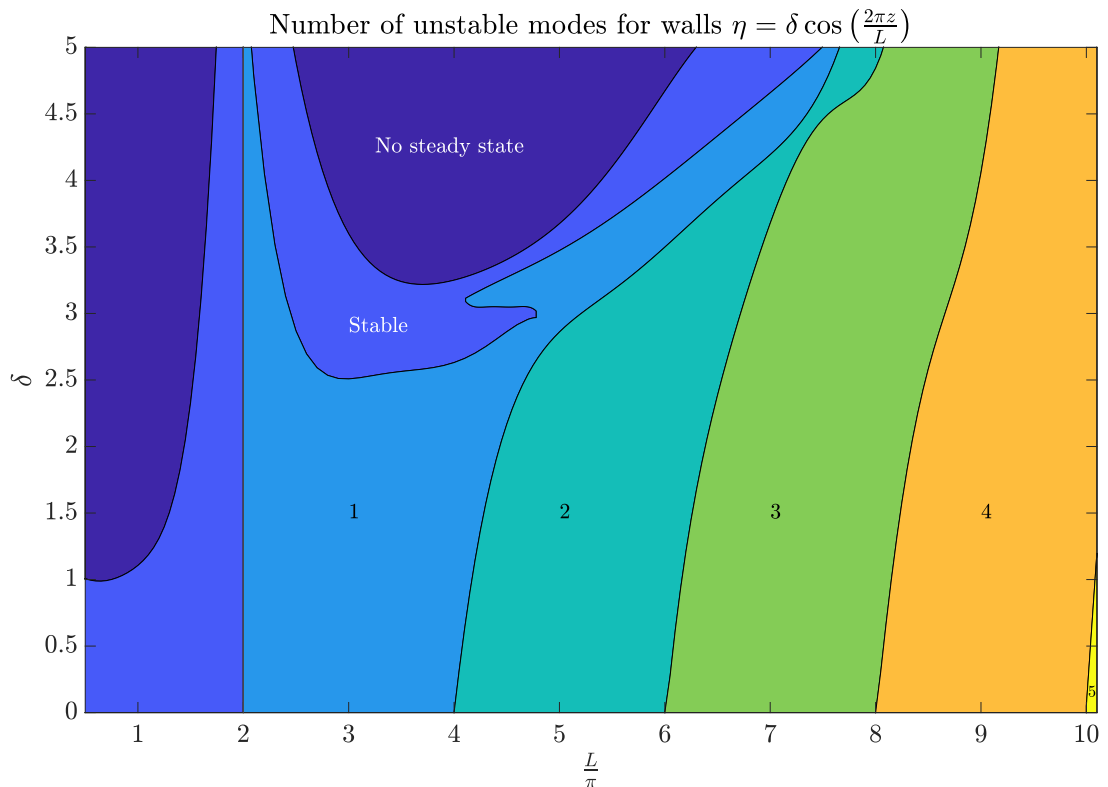


Figure 3.5: The number of unstable modes of the steady state for walls of the form $\eta = \delta \cos\left(\frac{2\pi z}{L}\right)$ where $R = \text{Bo} = 1$.

eigenvalues and corresponding eigenvectors. We can determine the number of unstable modes by looking at the eigenvectors where the eigenvalues have negative real part. The

real part of the eigenvectors is the growth rate. The imaginary part of these eigenvalues will tell us a wave speed for these eigenvectors.

Figure 3.5 shows the number of unstable modes of the steady states according to this Floquet analysis. As expected, there are only unstable modes for the case where $L > 2\pi R$. We see in the smooth cylinder case the additional modes appear for the multiples of 2π . Increasing the wall amplitude causes these higher modes to appear at longer wavelengths. The regions, in which no steady states were found, are shown here as in figure 3.2. We also see here that for a large enough amplitude, we do have a stable region for wavelengths $L > 2\pi$ corresponding to the lower flow rate. At larger amplitudes, the cases where there are fewer unstable modes occur roughly where the flow rate is smaller, as shown in figure 3.2.

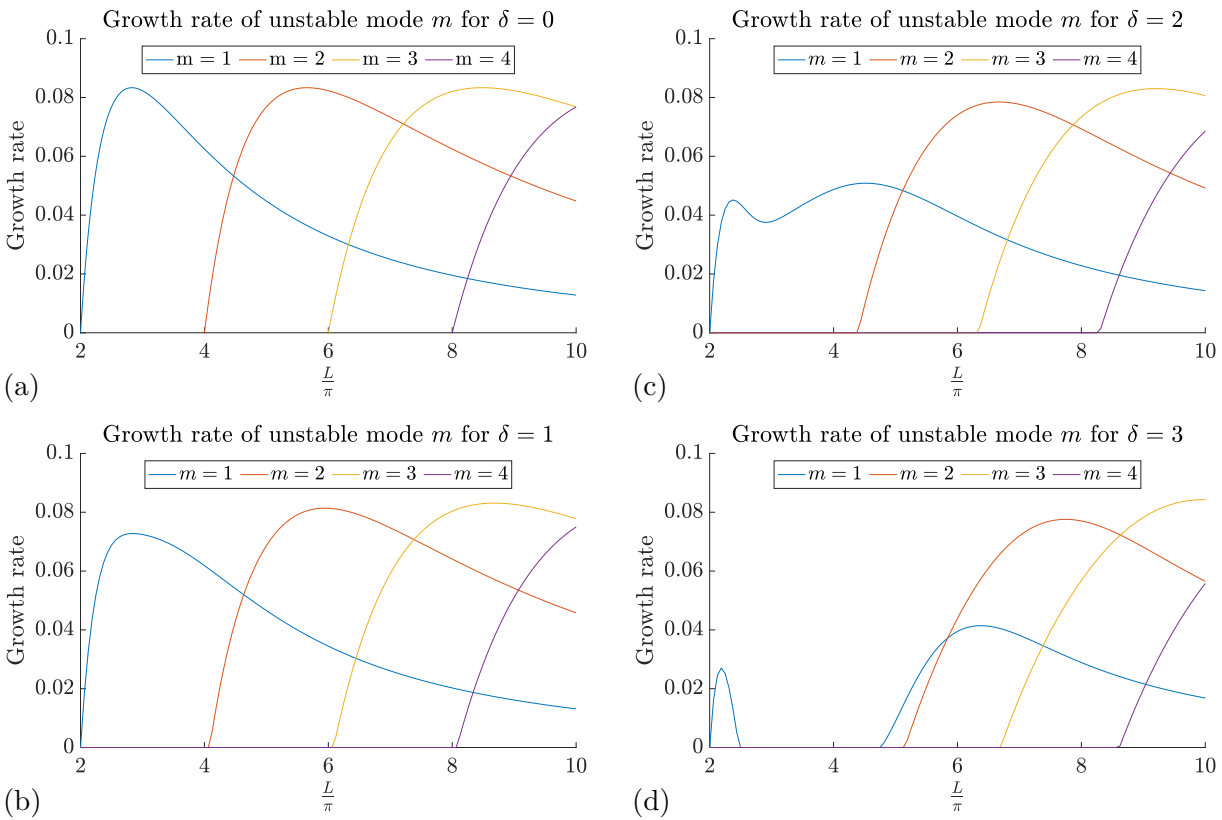


Figure 3.6: Growth rates of the first 4 unstable modes of the steady states from the Floquet analysis for different amplitude walls.

Figure 3.6 shows the growth rates (ω_r) of the first four unstable modes from the Floquet analysis. Increasing the amplitude of the wall has little effect on the growth rates, apart

from for the first unstable mode. As with figure 3.5, we see that increasing the wall amplitude makes the higher modes appear at longer wavelengths. From this figure, we also can see which mode is the most unstable at different wavelengths. Increasing the amplitude of the wall also causes the transition to occur at longer wavelengths.

3.5 Time Dependent Solutions

To solve equation (3.13) we have made use of the MATLAB function `ode15s`. In order to use this, we have split the domain z into 256 spatial steps, with spatial derivatives calculated using a pseudo-spectral technique, described in section 2.5. For these cases we integrated for 500 time units with the initial condition being

$$h_{\text{init}} = 1 + 0.1 \sin\left(\frac{2\pi z}{L}\right). \quad (3.35)$$

so that

$$\frac{1}{L} \int_0^L h_{\text{init}} \, dz = 1 \quad (3.36)$$

Here L is the same as the wavelength of the wall oscillation. We fixed the parameters $Bo = 1$ and $R = 1$ in order to primarily study the effect that the amplitude and wavelength of the wall had on the fluid thickness. As expected, the cases where $L < 2\pi$ settled to the steady state solution. Therefore, we will primarily be looking at the cases where $L > 2\pi$. Solutions were simulated for wavelengths of $L = 2\pi$ to $L = 10\pi$ at $\frac{\pi}{4}$ intervals, with amplitudes of $\delta = 0.1, 0.5, 1, 1.5, 2$. We also modelled the smooth cylinder equation $\eta = 0$ to see how the solutions compared. Larger amplitude ($\delta = 3, 4, 5$) solutions were also simulated between $L = 2\pi$ to $L = 10\pi$ at π intervals. This gave us a large range of results to compare.

From this initial condition (3.35), the fluid initially undergoes wave steepening. In shorter wavelength cases, generally where the $k = 1$ mode is the most unstable from the

Floquet analysis as seen in figure 3.6, the solution settles into a time periodic wave with a single dominant peak. Increasing the wavelength further, we found that the solutions could also form two or three peaked waves. These cases were sometimes quasi-periodic or non-periodic. To see if these eventually settled into a time periodic orbit, these solutions were further integrated up to 2000 time units.

An alternative type of solution also arises when the wall amplitude is sufficiently large. The large amplitude causes a much bigger pressure gradient from the increased surface tension. This slows the fluid down to such an extent that we lose the time periodic wave, and we see the fluid build up just past the peak of the wall, until finally gravity causes a drop to flow down to the next period and the process repeats. In the extreme case of this, the fluid dewets and is held in place by the pressure gradient.

We can classify the solutions by looking at the shape of the norm $\|h\|_2$ against time and by looking at the phase plane of $\|h\|_2$ and its time derivative. These results can be classified by looking at $\|h\|_2$. As with the steady states this is given by

$$\|h\|_2 = \sqrt{\frac{1}{L} \int_0^L h^2 dz}. \quad (3.37)$$

We can also consider the flow rate q as expressed in (3.15), however since we are in the time dependent regime the flow rate is no longer a constant in space. Therefore, we will consider the mean flow rate

$$Q = \frac{1}{L} \int_0^L q(z) dz. \quad (3.38)$$

The mean flow rate is a helpful indicator of when the transition into the dripping case occurs, as we can see it slowly approach 0.

Figure 3.7 shows some examples of the different types of solutions that were found. Here we have used $\|h\|_2$ to highlight the differences between the solution types. Figure (a) shows a time periodic solution, which can be seen by the phase plot being a closed loop. In this case, we find that the time it takes to go between peaks in $\|h\|_2$ is equal to the

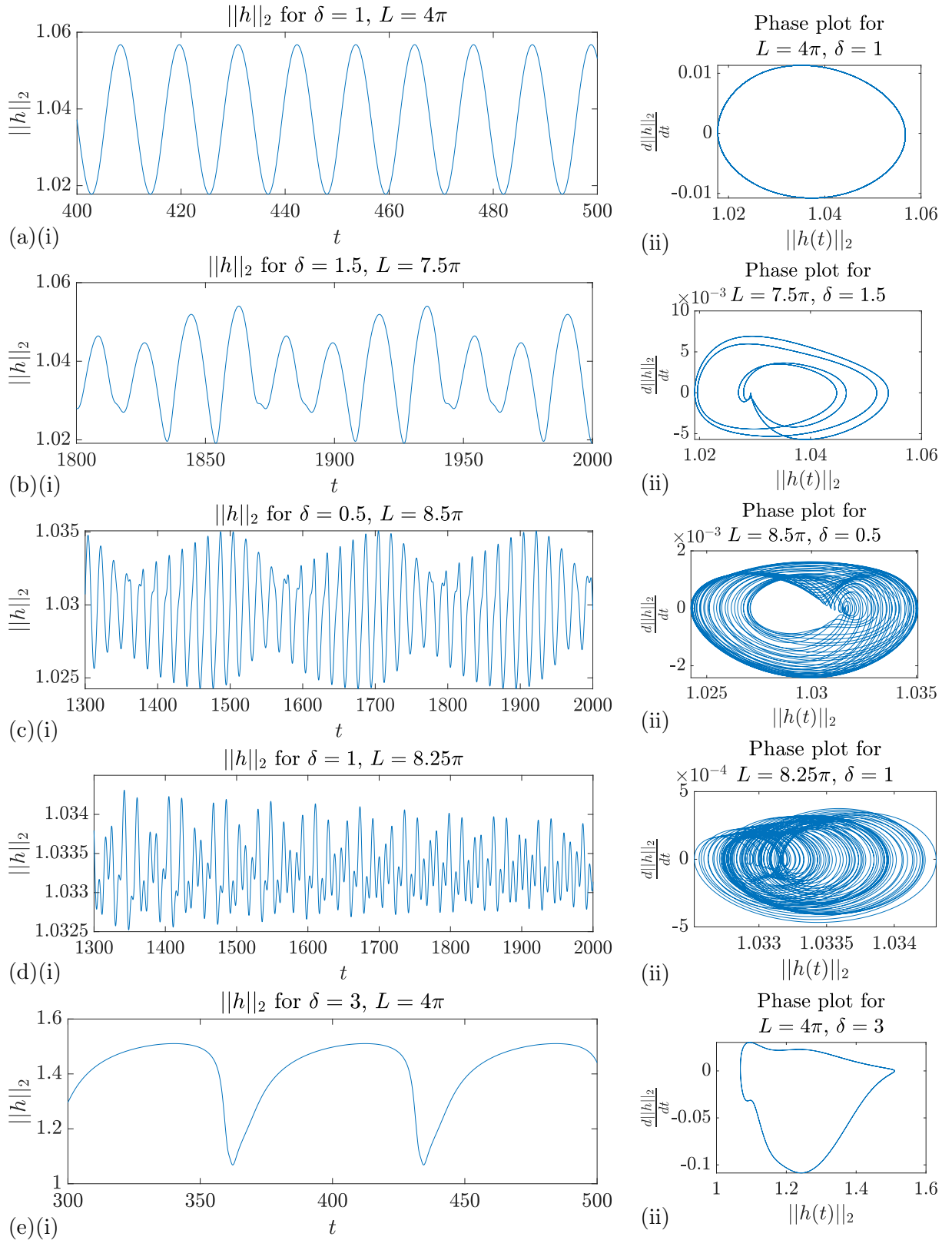


Figure 3.7: Plots used to classify the types of the solutions. (i) are plots of $\|h\|_2$ against time, and (ii) are phase plots of $\|h\|_2$ against its time derivative. (a) shows a time periodic solution. (b) has a time periodic solution where the period is different to the time it takes for a fluid peak to traverse 1 spatial period. (c) shows a quasi-periodic solution. (d) shows a non-periodic solution. (e) shows the case where the fluid produces a dripping motion.

time it takes a wave to travel one period. These occur for parameters that roughly match those for one unstable mode in figure 3.5.

Figure (b) is also time periodic as seen by the closed loop. Here the fluid peak travels a spatial period in the time between the consecutive maxima in $\|h\|_2$ where $\|h\|_2$ repeats every fourth period. This is probably a special case of the quasi-periodic wave, where this secondary frequency is an integer multiple of the wave frequency. Other periodic cases can arise where the fluid travels in a wave with 2 main peaks. In these cases, the time period of $\|h\|_2$ will be half of the traversal time, as it repeats once the first peak reaches the position of the second. This periodicity is further seen by looking at the map of the maximum $\|h\|_2$ in figure 3.8(a), where the maximum follows a path which makes a closed square.

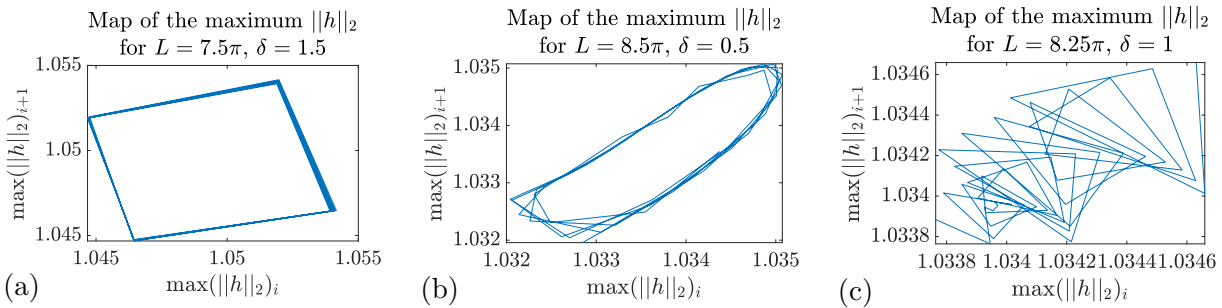


Figure 3.8: Map of the maximum $\|h\|_2$ of figure 3.7(b)-(d).

Figure 3.7(c) shows a quasi-periodic wave. Here we still have the oscillation from the fluid traversing a period. However there is also a secondary oscillation that is affecting the maxima of $\|h\|_2$. Here the oscillations have periods of around 17.5 and 210 time units, which means the shorter oscillation occurs about 12 times during the period of the longer oscillation. The quasi-periodicity is highlighted by the map of the maximum $\|h\|_2$ shown in figure 3.8(b). Here we see the path almost forms a loop.

Figure 3.7(d) shows a non-periodic solution, as there seems to be no coherent structure in either plot. This is further seen by the map of the maximum $\|h\|_2$ in figure 3.8(c), where the previous maximum has no obvious effect on the next one.

Figure 3.7(e) shows the dripping case. Here the fluid takes much longer to traverse a crenulation, with a period around 80 time units, compared to around 12 time units for (a).

We have called it the droplet case as here the fluid seemingly remains suspended, as can be seen by the broad maxima of $\|h\|_2$, and then quickly travels a period, as seen by the steep minima of $\|h\|_2$. This is also periodic as seen by the phase plot.

For the time periodic cases, we can calculate a wave speed by dividing the wavelength by the time it takes to traverse a period. By considering more periods, we calculate a more accurate mean speed. Similarly, we can calculate a mean speed for quasi-periodic and non-periodic waves by following a fluid peak over a long period of time.

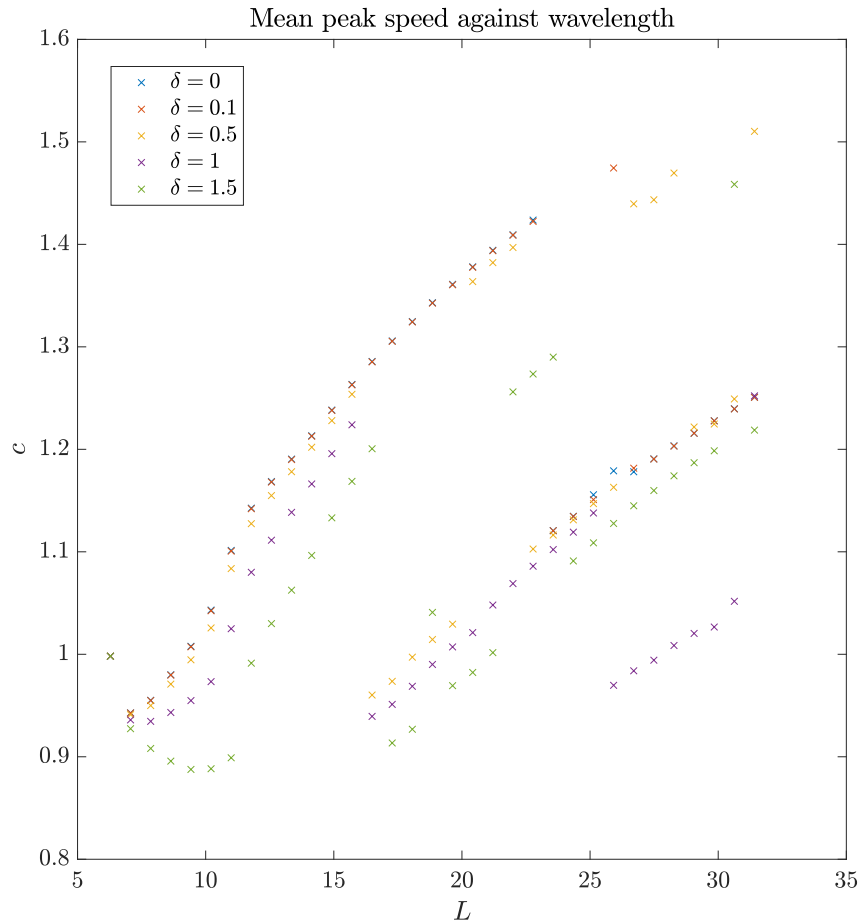


Figure 3.9: Speed of main peak in travelling wave for different wavelength and amplitude walls.

From figure 3.9 we can see that increasing the wavelength generally increases the wave speed. However, there are discontinuities where the wave speed suddenly drops. These discontinuities correspond to the solutions that form more than one main peak. Up until the first discontinuity there is one clear peak, after the first discontinuity there are two

peaks and after the second discontinuity there are three peaks. For longer wavelengths, the speeds may not follow the pattern. This is because this initial condition, seen in equation (3.35), can cause different contributions from the unstable modes. Increasing the amplitude of the wall decreases the mean speed of the travelling wave. The amplitude also affects the contributions of the unstable modes, with only the $\delta = 1$ case showing the three peak solutions.

As a consequence of the results in this figure, we considered solving equation (3.13) with different initial conditions, to see if we can force different contributions from the unstable modes. We will now look more closely at these types of solutions.

3.5.1 Time periodic waves

For the wavelengths where we expect one or two unstable modes, and where the amplitude of the wall hasn't significantly reduced the flow rate, we find that the solution eventually settles into a time periodic wave. With the initial conditions from equation (3.35), the solution starts with a wave steepening to appear more like its eventual shape. The time the wave takes to settle into its time periodic orbit can take up to 200 time units.

In figure 3.10 we look at the fluid thickness as the wave travels across one period for walls of amplitude $\delta = 1$. Subfigure (a) shows a section of $\|h\|_2$ between $t = 300$ and 320 for the cases in (b)-(d). Subfigures (b)-(d) show the fluid thickness. Here, the grey lines show the fluid thickness every 0.1 time units between the maxima of $\|h\|_2$. The fluid thickness at the times that have maximum and minimum $\|h\|_2$, and maximum and minimum mean flow rates Q are also highlighted in blue, red, yellow, and purple respectively.

From (a) we can see that the amplitude of oscillation has increased from the $L = 2.25\pi$ case to the $L = 4\pi$ case. However, the $L = 5.25\pi$ case has a smaller amplitude than both of them. We can see this from the fluid thicknesses, as the $L = 4\pi$ case has a much larger peak at the maximum of $\|h\|_2$ than at the minimum of $\|h\|_2$. This is different from the $L = 2.25\pi$ case where both fluid thicknesses have a fairly similar shape. In the case with $L = 5.25\pi$ we now have a solution that has 2 peaks and we can see that $\|h\|_2$ may oscillate

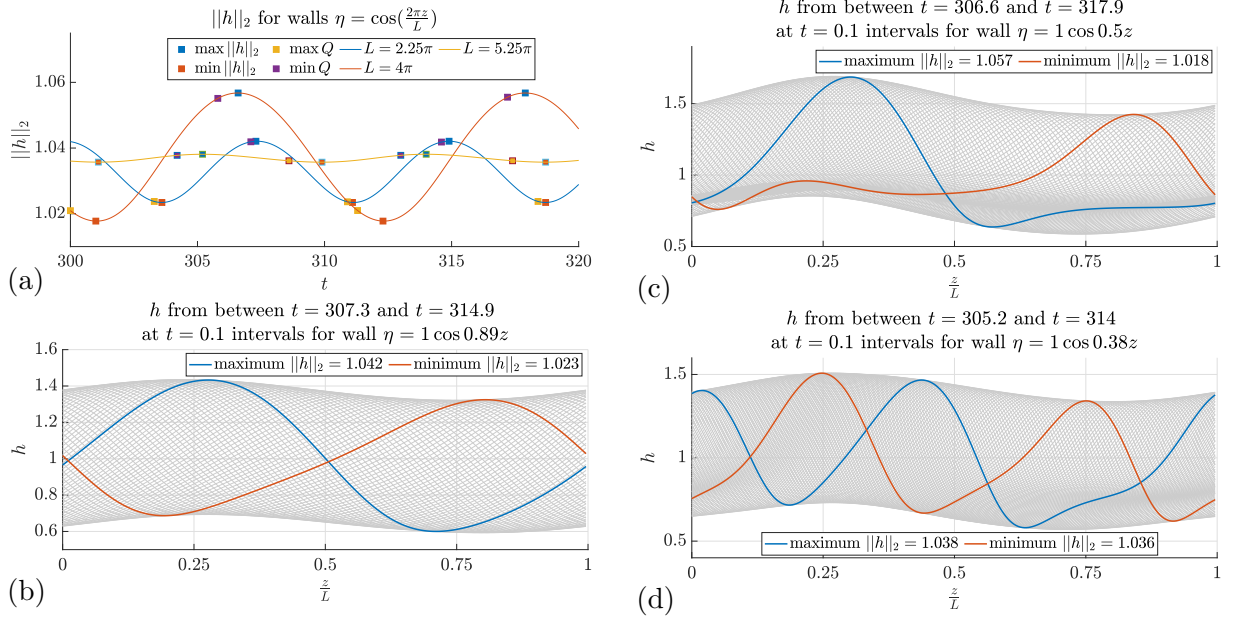


Figure 3.10: (a) Plot showing the $\|h\|_2$ for 20 time units from $t = 300$ (b), (c) and (d) show the fluid thickness for wavelengths of $L = 2.25\pi$, $L = 4\pi$ and $L = 6\pi$ respectively where the amplitude of the wall is $\delta = 1$ for all cases. The grey curves are taken every 0.1 time unit between the consecutive maximums highlighted in (a). The fluid thickness at the maximum and minimum flow rates and $\|h\|_2$ are highlighted.

less than the other cases, as when one of the peaks obtains the maximum thickness, the other peak is at the minimum thickness. From this figure, we also see that the maximum mean flow rate occurs close to the minimum $\|h\|_2$ and vice versa.

The grey lines show the path that the maximum and minimum fluid thicknesses trace out. In these cases, we see that the maximum thickness is obtained around $\frac{z}{L} = 0.25$, noting here that the peak in the wall is located at $\frac{z}{L} = 0$. These all follow a similar shape to the steady state solutions. The $L = 2.25\pi$ case flow is fairly sinusoidal, whereas increasing the wavelength makes the fluid thickness appear more non-linear.

We can also see how long it takes for the fluid peak to traverse the period. For the $L = 2.25\pi$ case, this takes 7.6 time units, resulting in an average speed of $c = 0.93$. The $L = 4\pi$ case takes 11.3 time units before it has reached the same state, resulting in a speed of $c = 1.1$. The $L = 5.25\pi$ case may seem at first to be going a lot faster, taking only 8.8 time units to get to the next peak in $\|h\|_2$. This is however only the time it takes for one peak to get to the position of the other peak, and so this peak will complete a period at

the next maximum of the $\|h\|_2$. This gives a mean speed of $c = 0.94$.

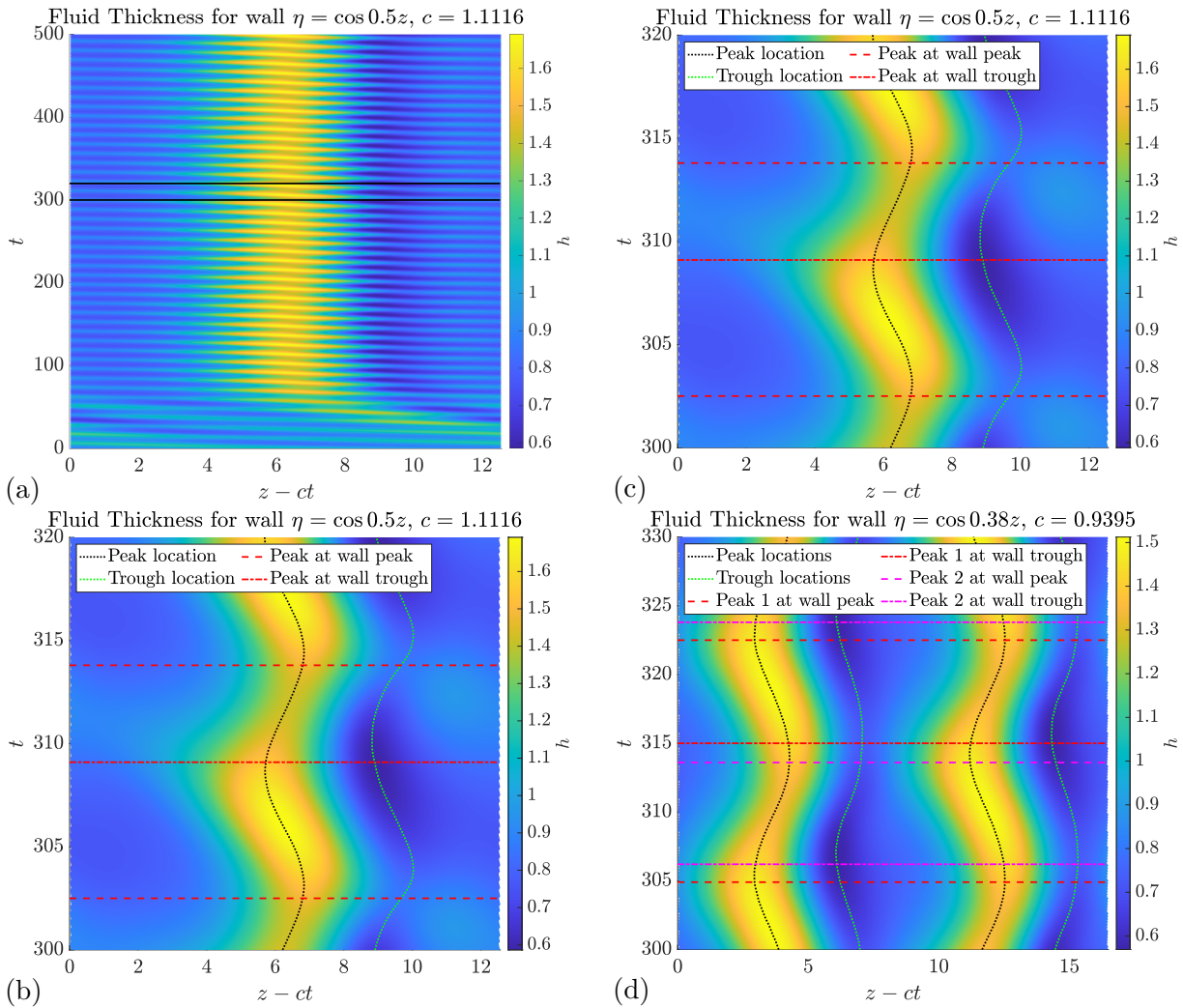


Figure 3.11: Colour plots showing the fluid thickness moving in a frame that travels at the mean wave speed. (a) shows all 500 time units for the $L = 4\pi$ case. (b), (c) and (d) show the fluid thickness for wavelengths of $L = 2.25\pi$, $L = 4\pi$ and $L = 6\pi$ respectively where the amplitude of the wall is $\delta = 1$ for all cases. These have been taken from $t = 300$ and show at least one period. The location of the peaks and troughs of the fluid thickness is highlighted, as well as the time at which the fluid thickness peak travels above the peaks and troughs of the wall.

Figure 3.11 shows the waves from figure 3.10 but now viewed from a frame of reference which moves at the mean speed c . The fluid thickness is represented by colour, with the peak being yellow and the trough being blue. These figures show how the wave speed differs from the mean speed, as a wave travelling at a constant speed will remain in the same position when viewed in this frame.

Subfigure (a) shows the dynamics from the initial condition up to $t = 500$, where

(b)-(d) take a section from $t = 300$ to show how the speed changes across a period. From (a) we can see that the peak initially travels at a slower speed, and accelerates into this mean speed as shown by the vertical yellow line. Subfigures (b) and (c) show similar dynamics, with the fluid peak travelling faster than the mean speed after the trough and slower after the peak. Between the wall peak and the wall trough, the fluid is effectively flowing down an overhanging wall, where between the trough and the peak the fluid is now flowing down a slope. In (d) we still have this effect occurring which makes the 2 different peaks, speed up and slow down, seemingly out of phase.

3.5.2 Branching solutions

For longer wavelengths where the Floquet analysis shows multiple unstable modes, we find that different initial conditions can be attracted into different solutions. Solutions have been found with one, two or three dominant peaks, corresponding to the first 3 unstable modes. Examples of such solutions are shown in figure 3.12, where again we are in a frame

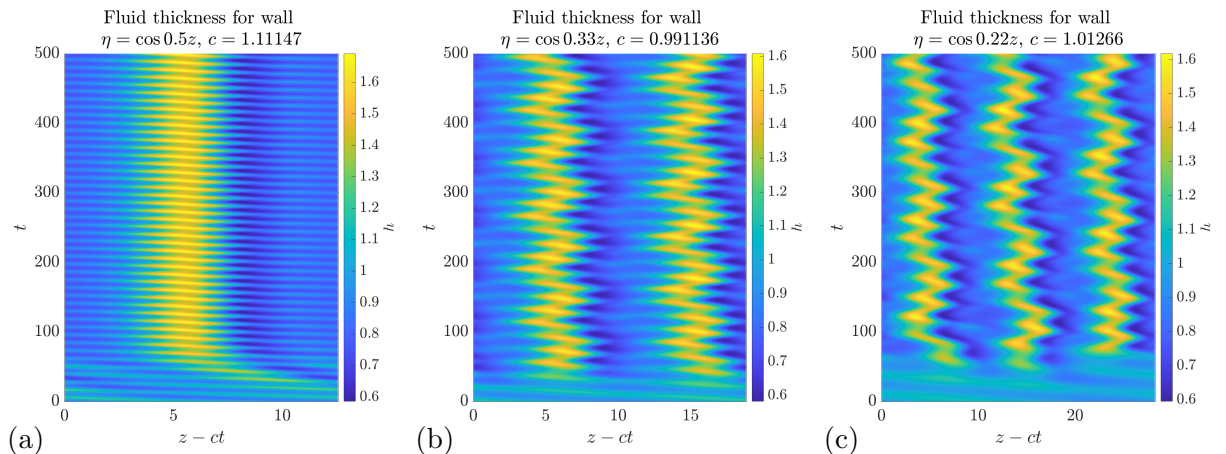


Figure 3.12: The fluid thickness for the travelling in a frame of reference that tracks the waves. (a) is the $\delta = 1, L = 4\pi$ showing a single peak (b) is the $\delta = 1, L = 6\pi$ showing a double peak (c) is the $\delta = 1, L = 9\pi$ showing a triple peak.

of reference which travels at the mean speed of the peak.

To find solutions that favoured different unstable modes, we chose our initial conditions in one of two ways. In cases where the desired solution shape occurred at a wavelength $\frac{\pi}{4}$ longer or shorter than we wanted, this solution was scaled to the required wavelength

and used as the initial condition. Alternatively, for the longer wavelength cases, where we wanted a case with multiple peaks, we used multiple periods of a lower wavelength case. For example, if we were looking for a two peak solution of the $L = 8\pi$ case, we could use the solution of the $L = 4\pi$ repeated as our initial condition.

This method showed that many solution branches were possible, as the solution could settle into different attractors, which both have the same number of peaks in the fluid thickness. To highlight this, we have taken the case with the wall amplitude $\delta = 1$ and wavelength $L = 9\pi$.

Figure 3.13 shows 5 different solutions that arise for the cases where the wall has wavelength $L = 9\pi$ and amplitude $\delta = 1$. Subfigures (a)-(c) resulted in time periodic solutions, whereas (d) and (e) were non-periodic. This can be seen by the fluid thickness, which are shown over a longer time frame for the non-periodic cases.

Case (a) exhibits one main peak, and from the Fourier spectrum we see that the first Fourier mode is the largest. However, there are still significant contributions from modes 2 – 5. Subfigures (b) and (c) both show 2 significant peaks. The difference here is that for (b) the peaks are of similar shapes and spaced almost equidistantly apart. In (c) the peaks are much closer together. A third smaller peak forms slowly in the gap, but as it travels slower than the other two peaks, the leading peak quickly catches it and incorporates it. This would suggest why (b) has a strong contribution from the second Fourier mode, while (c) has a strong contribution from the third mode. We also see that the Fourier modes in (b) vary only slightly compared to the other cases.

Cases (d) and (e) both have their strongest contribution from the third mode and much weaker contributions from the first and second modes, which could suggest the first two modes help keep the solution to be time periodic. (d) seems to oscillate less than (e) and this may be due to (e) having a much more varied fourth Fourier mode.

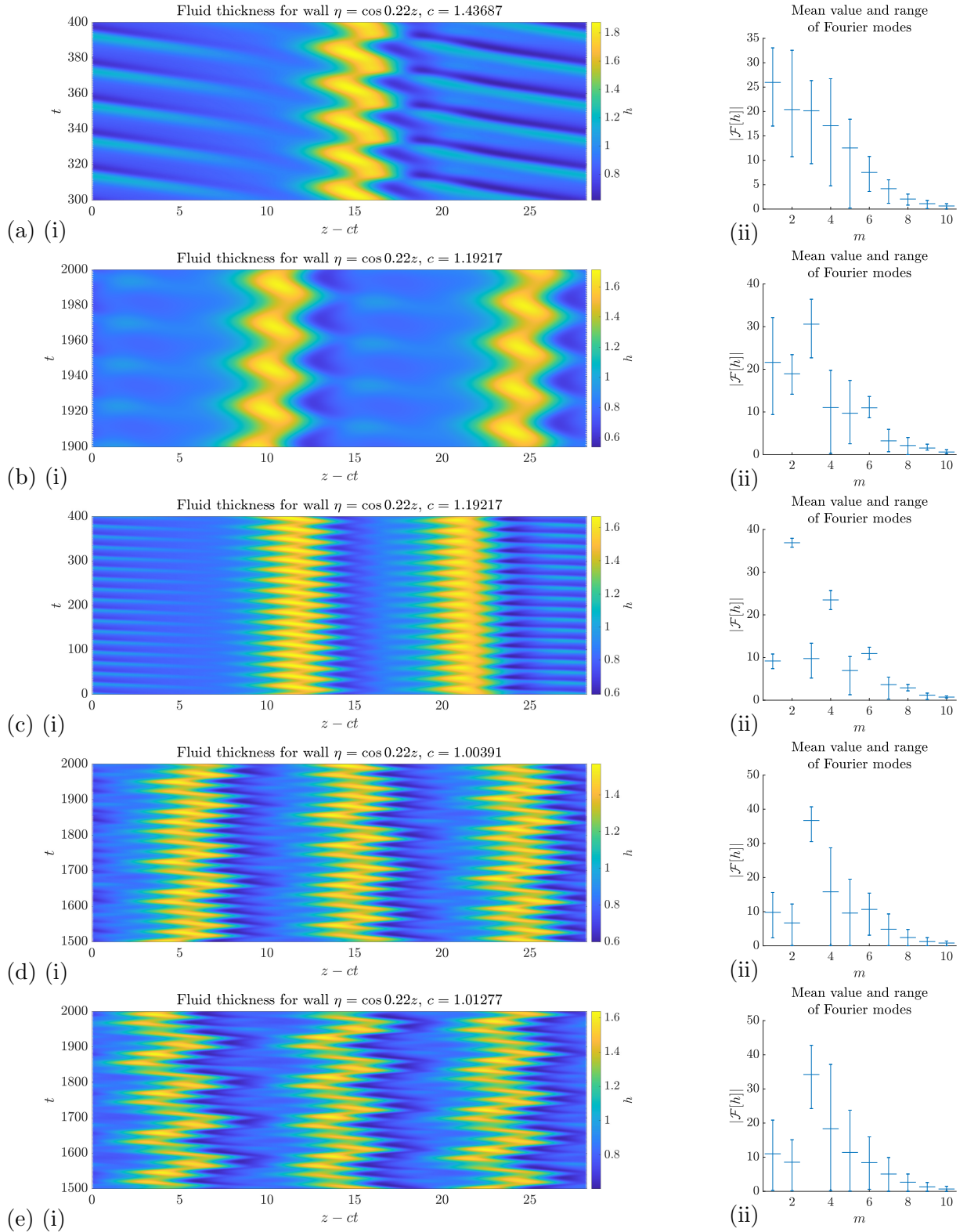


Figure 3.13: Example solutions that occur for wall wavelength $L = 9\pi$ with wall amplitude being $\delta = 1$. (a)-(c) are time periodic solutions, with (d)-(e) being non-periodic solutions. Subfigures (i) show the fluid thickness over time in a frame that moves with the mean speed of the wave. Subfigures (ii) show the time averaged size of the first 10 Fourier modes of the fluid thickness, as well as the range.

3.5.3 Dripping cases

Looking at larger amplitude walls, generally where the steady states are stable according to the Floquet analysis, or where no steady states were found as shown in figure 3.5, we can still find the dynamics using the same initial condition (3.35). Here the fluid builds up before suddenly being released, in a sort of dripping motion. In the extreme case of this, the fluid is held in place.

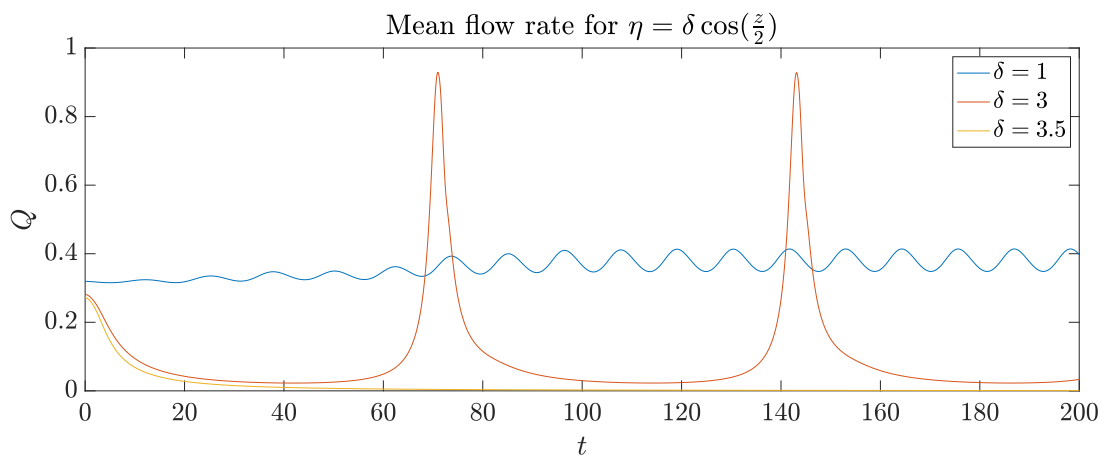


Figure 3.14: Mean flow rates for a periodic travelling wave ($\delta = 1$), a dripping case ($\delta = 3$), and where the fluid is held in place ($\delta = 3.5$).

Figure 3.14 highlights this by showing the mean flow rate (3.38). Here the $\delta = 1$ case is a time periodic solution, where the flow rate oscillates gently. The $\delta = 3$ case is the dripping case, where we see for around 60 time units the mean flow rate is quite small, and then spikes. The $\delta = 3.5$ case is where the fluid is held in place, as can be seen by the mean flow rate tending to 0.

The dripping case roughly occurs where the Floquet analysis suggested the steady state was stable, within the region with one unstable mode, as shown by figure 3.5. From figure 3.15, we see that the bulk of the fluid is held just after the peak in the wall for long periods of time. Figure (a) shows the peak of the fluid slowly move to the right. As this happens we also see that the small layer of fluid, between the wall trough and peak, gets thinner as time advances. Figure (b) shows the 5 time units where the fluid quickly traverses the period. Also shown is the fluid profile 5 time units before and after. From

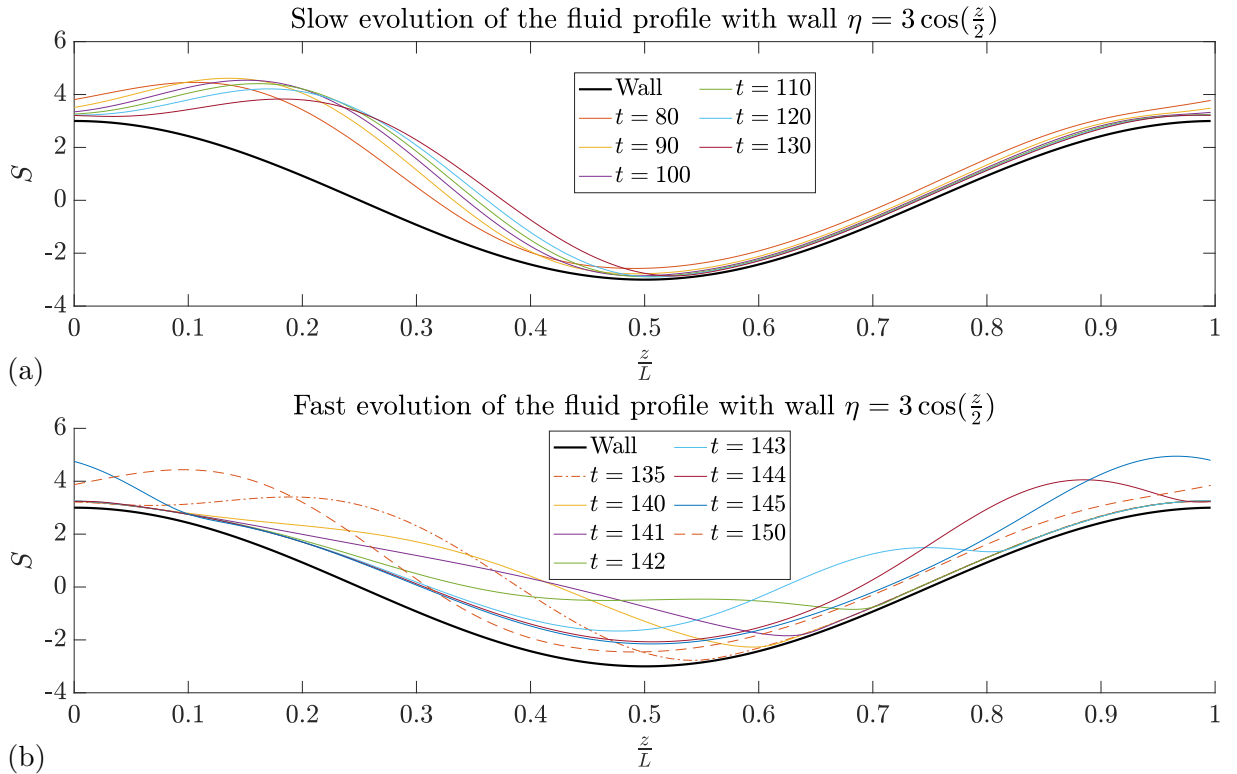


Figure 3.15: Fluid profiles for a dripping case where the wall is $\eta = 3 \cos(\frac{z}{2})$. (a) shows the 50 time unit period where the fluid moves slowly from the wall peak. (b) shows a 5 time unit period where most of the fluid traverses the wall period.

this we see the peak collapses. In front of the collapsing peak, the fluid pinches the wall. The wave follows this pinch point until it reaches the wall maximum, where a thin layer of fluid separates it from the wall again. The fluid is then held just after the maximum again and the process then repeats.

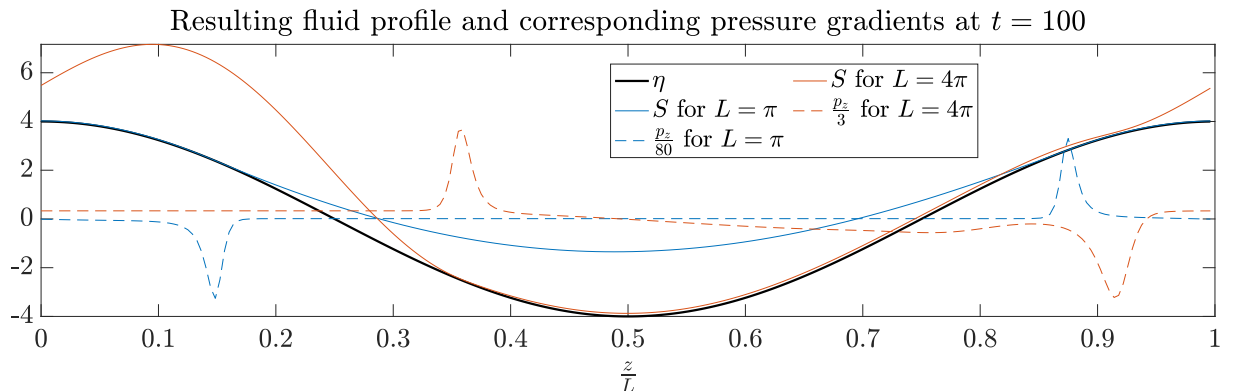


Figure 3.16: Fluid profiles that result from simulating the flow with low mean flow rates.

For cases with larger amplitude, generally where no steady state was found, as shown

by figure 3.5, the fluid remains held in space. These are the cases where the flow rate tends to 0 in figure 3.14. Figure 3.16 shows the cases where the wall amplitude $\delta = 4$. We find that for wavelengths $L < 2\pi$ the fluid thins over the peaks and ends up mostly in the trough, however for wavelengths $L > 2\pi$ the fluid builds up just after the wall peak and thins in the wall trough. This has been shown using the $L = \pi$ and $L = 4\pi$ cases. Also in this figure we have plotted the corresponding pressure gradients that have been scaled down, so that they appear on the same axis. In both cases we see that the fluid is held up behind a sharp positive pressure gradient, and is also contained before the negative pressure gradient.

3.6 Relationship Between the Steady State and the Time Dependent Solutions

For stalactites, the chemical deposition occurs at a much longer timescale than the fluid dynamics (Short et al., 2005b). Because of this Vesipa et al. (2015); Camporeale (2017), make use of the quasi-steady approximation, taking the steady state fluid thickness. However for these cases where the steady state is unstable it is more appropriate to take a mean fluid thickness.

The mean fluid thickness is given by

$$\bar{h}(z) = \frac{1}{T} \int_t^{t+T} h(z, \tau) d\tau \quad (3.39)$$

where t is chosen to be when the fluid thickness has settled into its orbit. For the periodic cases, T is chosen to be the time period of that wave. Otherwise T is chosen to be as large as possible for a better average.

Figure 3.17 shows the difference between the time average and the steady state. Figure (a) shows the result for cases (a), (b) and (e) from figure 3.13. These only differ by less than 2% from the steady state, despite having very different structures. Here we also see

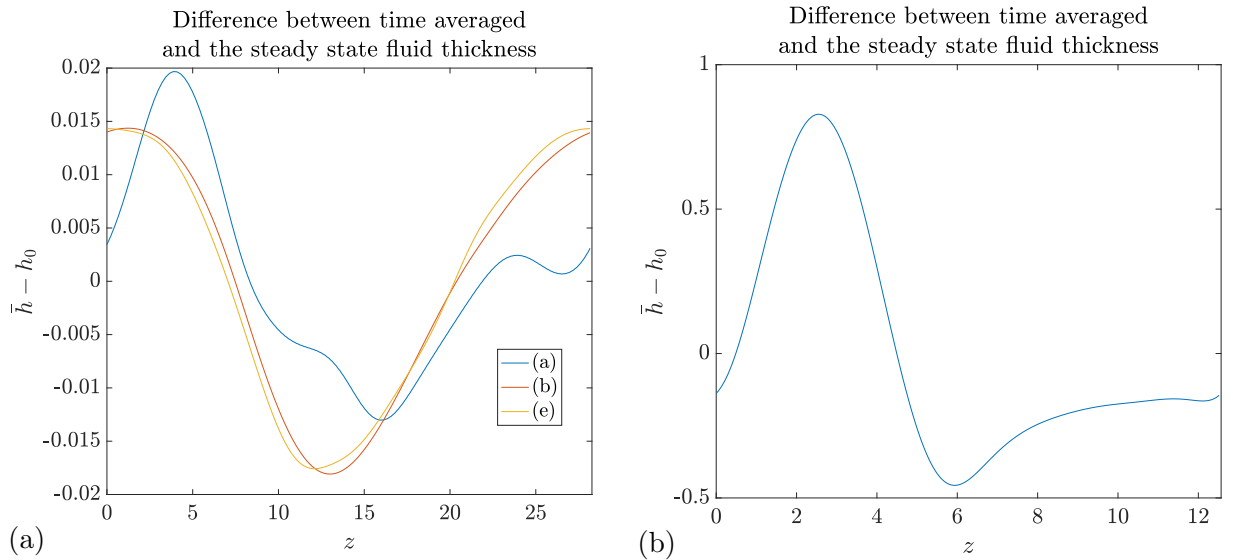


Figure 3.17: The difference between the time averaged fluid thickness and the steady state. (a) shows cases from figure 3.13. (b) shows the example of the dripping case from 3.15.

that even though (e) is non-periodic, it has a very similar time average to the time periodic case (b). All the cases seem to suggest that the time averaged thickness is generally thicker around the wall maximum and thinner around the wall minimum than the steady state.

While for these cases the steady state thickness gives a pretty good approximation to the time averaged thickness, this is not the case for the cases where the droplet forms, as can be seen in subfigure (b). In these cases, there are long periods of time with the fluid held in place by the pressure gradient, this causes the average to approximate that shape.

3.7 Conclusions

In this chapter we have looked at a gravity driven, thin film flow down a cylinder, which has a wall perturbation of similar order to the fluid thickness. We have considered the pressure gradient to be of a similar size to gravitational acceleration, so that the wall shape comes into the equation at leading order. We derived an equation for the dynamics of the fluid thickness.

Studying the steady states, we found $L = 2\pi R$ was a critical wavelength for both the stability and shape. The steady states were stable for $L < 2\pi R$ regardless of the

wall amplitude. In these cases, the fluid peak was occurring just downstream of the wall minimum. These cases also generally had larger amplitude disturbances to the fluid thickness, being of a size similar to that of the wall amplitude. The $L > 2\pi R$ cases generally had the fluid thickest between the wall maximum and the wall minimum. For these cases, the amplitude of the disturbance to the fluid thickness was much smaller. Performing Floquet analysis, we found that increasing the amplitude of the wall caused the additional unstable modes to only appear at longer wavelengths.

We then numerically integrated the equation to find the dynamics of the film thickness. The Floquet analysis generally gave a good indication for how the film thickness would evolve in time. The stable cases settled to the steady state, and we found that the unstable cases either settled into time periodic orbits, quasi-periodic orbits or non-periodic solutions. We found time periodic orbits where the Floquet analysis showed that there was only one unstable mode. For the cases with more unstable modes, we found that multiple solutions could exist, where these could be any of these cases depending on how the unstable modes interacted. Interestingly, taking the time average of these solutions approximated the steady state solution. A special case was found for larger amplitude walls, where the pressure gradient could hold the fluid in place. The fluid would then either perform a dripping motion or was held in place.

Chapter 4

Hydrodynamics 2: Effects of Inertia

4.1 Introduction

Thin film flows down cylinders is an important area to study for both natural phenomena and those that arise in the industrial setting. The topography and the cylindrical geometry can alter the effect that the surface tension has on the dynamics of the fluid. Previous works when considering a flow down a cylinder tend to consider that the radius is a similar length scale to that of the fluid thickness, such as by Craster and Matar (2006). An alternative approach views the radius as being much larger than that of the fluid thickness (Frenkel, 1992; Kalliadasis and Chang, 1994). Both of these approaches lack terms that can occur if the size of the radius is the same length scale as the capillary length.

In order to capture the effects, we will follow the work of Frenkel (1993) for our smooth cylinder scenario. Here inertial effects and shear due to the cylindrical geometry appear at the same order as the surface tension. In this work, we will see how adding topography onto a cylinder will affect the flow of a thin film. The wavelength of the topography will be a similar value to that of the radius.

Topographical effects on thin films has been studied in works by Kalliadasis et al. (2000); Tseluiko et al. (2013, 2008). Other works that have looked at topographically patterned cylinders include that of Parrish et al. (2021), however, this focuses on rotating

cylinders and gravity is not perpendicular to the radius.

Flow down corrugated cylinders could be important for the formation of geological features such as stalactites. Previous works to model stalactites consider flow down an inclined plate (Short et al., 2005b; Vesipa et al., 2015; Camporeale, 2017), however this may ignore some effects that the geometry has on the growth of stalactites.

4.2 Governing Equations

As in chapter 3, we will be considering a thin film flow under gravity down a cylinder that has a long wave disturbance to its surface. The cylinder and its disturbance are fixed in time. The amplitude of this disturbance is of the same order as the fluid thickness. Continuing on from section 2.2, where we have nondimensionalised the Navier Stokes equation (2.5)-(2.11) by using the scalings (2.14)-(2.16). This resulted in the nondimensional equations (2.20)-(2.26). As discussed in section 2.2, in this chapter we will work with a scaled Bond number $Bo = \frac{B}{\epsilon^2} = \frac{\rho h_0^2 g}{\gamma \epsilon^2}$. This Bond number is ϵ times smaller than that studied in chapter 3. Here we will scale the pressure term using

$$P = \rho h_0 g \quad (4.1)$$

to make it clearer to see where it appears in the momentum equations (2.21)-(2.22). Under these scalings the equations (2.20)-(2.26) are

$$u_r + w_z - \eta_z w_r + \epsilon \frac{u}{R} = O(\epsilon^2) \quad (4.2)$$

$$\epsilon u_{rr} - p_r = O(\epsilon^2) \quad (4.3)$$

$$w_{rr} + 1 + \epsilon \left(\frac{w_r}{R} - p_z - \text{Re}(w_t + u w_r + w(w_z - \eta_z w_r)) \right) = O(\epsilon^2) \quad (4.4)$$

$$u = 0, w = 0 \quad \text{at } r = 0 \quad (4.5)$$

$$u = h_t + w(\eta_z + h_z) \quad \text{at } r = h \quad (4.6)$$

$$w_r(h) = O(\epsilon^2) \quad (4.7)$$

$$p(h) = \frac{1}{\text{Bo}} \left(\frac{1}{\epsilon R} - \frac{\eta + h}{R^2} - (\eta_{zz} + h_{zz}) \right) \quad (4.8)$$

4.2.1 Smooth cylinder case

We begin by looking at flow down a cylinder of constant radius. This will be known as the smooth cylinder case, as here there are no crenulations, so $\eta = 0$. To solve equations

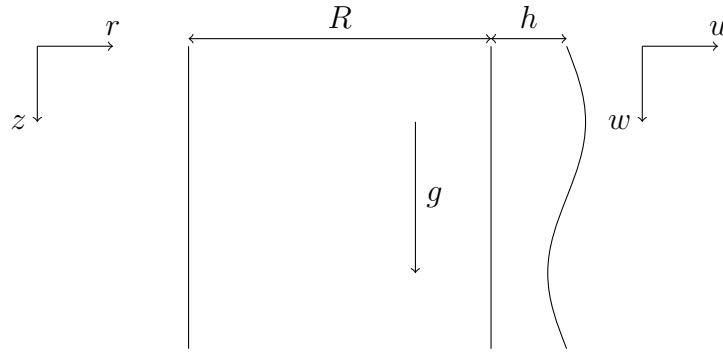


Figure 4.1: Geometry of the smooth cylinder problem

(4.2)-(4.8), we expand our variables in powers of ϵ by writing them of the form $y = y_0 + \epsilon y_1$. We can then find the leading order velocities by looking at the leading order equations. Equations (4.4), (4.5), and (4.7) become

$$\frac{\partial^2 w_0}{\partial r^2} + 1 = 0, \quad w_0(0) = 0, \quad \frac{\partial w_0}{\partial r} \Big|_h = 0, \quad (4.9)$$

which results in

$$w_0 = hr - \frac{r^2}{2}. \quad (4.10)$$

Substituting this into equation (4.2) we get the leading order equation for the radial velocity

$$\frac{\partial u_0}{\partial r} + h_z r = 0. \quad (4.11)$$

Applying the boundary condition (4.5) results in

$$u_0 = -h_z \frac{r^2}{2}. \quad (4.12)$$

Finally applying the leading order velocities (4.10), (4.12) to the kinematic condition (4.6) we get the leading order evolution equation for the fluid thickness

$$h_t + h_z h^2 = 0. \quad (4.13)$$

Equation (4.13) leads to wave steepening and so higher order terms are required to regularise the dynamics (Craster and Matar, 2009). Therefore to see the effects that the Reynolds and Bond numbers have on the fluid thickness, we look at equations (4.2)-(4.8) at $O(\epsilon)$. Equation (4.4) at $O(\epsilon)$ gives

$$\begin{aligned} \frac{\partial^2 w_1}{\partial r^2} &= \text{Re} \left(\frac{\partial w_0}{\partial t} + u_0 \frac{\partial w_0}{\partial r} + w_0 \frac{\partial w_0}{\partial z} \right) - \frac{1}{R} \frac{\partial w_0}{\partial r} + \frac{\partial p_0}{\partial z} \\ &= \text{Re} h h_z \left(\frac{r^2}{2} - h r \right) + \frac{1}{R} (r - h) + \frac{\partial p_0}{\partial z}. \end{aligned} \quad (4.14)$$

where to resolve the time derivative we can solve this with the boundary conditions (4.5), and (4.7) at $O(\epsilon)$

$$w_1(0) = 0 \quad (4.15)$$

$$w_{1r}(h) = 0 \quad (4.16)$$

resulting in

$$w_1 = \text{Re} h h_z \left(\frac{r^4}{24} - \frac{h r^3}{6} + \frac{h^3 r}{3} \right) - \frac{\partial p_0}{\partial z} \left(h r - \frac{r^2}{2} \right) + \frac{1}{R} \left(\frac{r^3}{6} - \frac{h r^2}{2} + \frac{h^2 r}{2} \right). \quad (4.17)$$

Again we find the radial velocity by integrating the continuity equation (4.2)

$$u_1 = - \int_0^h \frac{\partial w_1}{\partial z} + \frac{u_0}{R} dr, \quad (4.18)$$

with the condition $u_1(0) = 0$ from equation (4.5), which results in

$$\begin{aligned} u_1 = & - \operatorname{Re}(hh_z)_z \left(\frac{r^5}{120} - h \frac{r^4}{24} + h^3 \frac{r^2}{6} \right) - \operatorname{Re} h h_z^2 \left(h^2 \frac{r^2}{2} - \frac{r^4}{24} \right) \\ & + \frac{\partial^2 p_0}{\partial z^2} \left(h \frac{r^2}{2} - \frac{r^3}{6} \right) + \frac{\partial p_0}{\partial z} h_z \frac{r^2}{2} - \frac{1}{R} \left(-h_z \frac{r^3}{6} + h h_z \frac{r^2}{2} \right) + \frac{h_z}{6R} r^3. \end{aligned} \quad (4.19)$$

Substituting the leading order and first order velocities (4.10), (4.12), (4.17), (4.19) in the kinematic condition (4.6), results in the evolution equation for the fluid thickness

$$h_t + h_z h^2 + \epsilon \frac{\partial}{\partial z} \left(\frac{h^4}{12R} + \frac{2}{15} \operatorname{Re} h^6 h_z - \frac{h^3}{3} \frac{\partial p_0}{\partial z} \right) = 0. \quad (4.20)$$

The leading order pressure gradient can be found from equation (4.3) at leading order, which tells us that pressure is a constant with respect to r . This constant can be found from the tangential stress condition (4.8), resulting in the pressure gradient

$$\frac{\partial p_0}{\partial z} = - \frac{1}{\operatorname{Bo}} \left(\frac{h_z}{R^2} + h_{zzz} \right). \quad (4.21)$$

Substituting the pressure gradient into equation (4.20), gives us

$$h_t + h_z h^2 + \epsilon \frac{\partial}{\partial z} \left(\frac{h^4}{12R} + \frac{2}{15} \operatorname{Re} h^6 h_z + \frac{h^3}{3 \operatorname{Bo}} \left(\frac{h_z}{R^2} + h_{zzz} \right) \right) = 0. \quad (4.22)$$

This equation is also found by Frenkel (1993). Here we see that we have terms relating to the radius, inertia and surface tension. We can look at increasing the radius of our cylinder so that it appears as a plane. This is calculated by taking the limit $R \rightarrow \infty$. Doing this, we get the Benney equation down a vertical plane (Benney, 1966; Joo et al., 1991).

4.2.2 Wall with topography

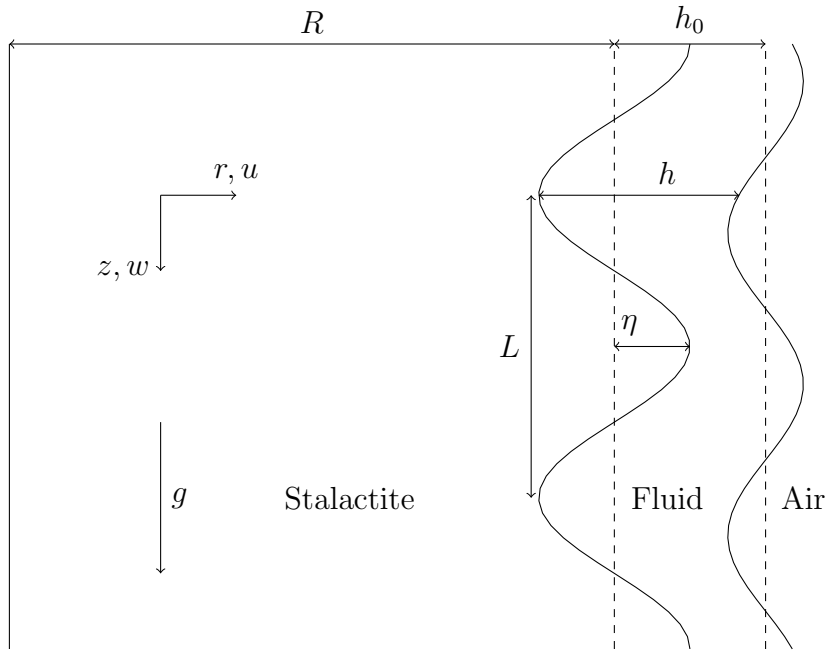


Figure 4.2: Geometry of the problem with a wall disturbance

We now say that the cylinder is not of constant radius, but instead is disturbed by some function η , where η has an amplitude that is roughly the same length as the fluid thickness. We also have that the wavelength of η is a similar length to the radius. Looking at the leading order terms of equations (4.2)-(4.8), we see η appear only in (4.2) and (4.8). Therefore w_0 is the same as the smooth cylinder case. From equation (4.8) the pressure gradient is now.

$$\frac{\partial p_0}{\partial z} = -\text{Bo} \left(\frac{h_z + \eta_z}{R^2} + h_{zzz} + \eta_{zzz} \right). \quad (4.23)$$

The new radial velocity (with a hat) can be expressed in terms of the smooth cylinder radial velocity (4.12) (without a hat) as

$$\hat{u}_0 = u_0 + \eta_z w_0. \quad (4.24)$$

Looking at $O(\epsilon)$ terms of equations (4.2)-(4.8), we find again w_1 is written as in equation (4.17), with the pressure gradient now being equation (4.23). Again we find the radial

velocity at this order has been modified from the smooth cylinder case (4.19) to give

$$\hat{u}_1 = u_1 + \eta_z \hat{w}_1 - \int \eta_z \frac{w_0}{R} dr. \quad (4.25)$$

Substituting equations (4.10), (4.17), (4.23), (4.24), (4.25) into the kinematic condition (4.6), we find that the $\eta_z \frac{\partial w_1}{\partial r}$ terms cancel. However, the $\int \eta_z \frac{w_0}{R} dr$ remains, leaving us with

$$h_t + h_z h^2 + \epsilon \frac{\partial}{\partial z} \left(\frac{h^4}{12R} + \frac{2}{15} \text{Re} h^6 h_z + \frac{h^3}{3 \text{Bo}} \left(\frac{h_z + \eta_z}{R^2} + h_{zzz} + \eta_{zzz} \right) \right) + \epsilon \frac{\eta_z h^3}{3R} = 0. \quad (4.26)$$

4.2.3 Conservative form

Equation (4.26) is not in conservative form. It is useful to transform the equation into conservative form in order to make it easier to solve numerically. We can transform it into conservative form by finding the mass density

$$\begin{aligned} m &= \int \tilde{r} d\tilde{r} = \int_0^h \frac{R}{\epsilon} + \eta + r dr \\ &= \frac{hR}{\epsilon} + h\eta + \frac{h^2}{2}. \end{aligned} \quad (4.27)$$

If we let $H = \frac{\epsilon}{R}m$, so that from equation (4.27) we get

$$H = h + \frac{\epsilon}{R} \left(h\eta + \frac{h^2}{2} \right). \quad (4.28)$$

We can find the dynamics of this new variable by taking the time derivative of H and substituting in h_t from equation (4.26). Again we will truncate the equation to only look at terms that are order 1 and ϵ . This results in the equation

$$H_t + \frac{\partial}{\partial z} \left(\frac{H^3}{3} + \epsilon \left(\frac{2}{15} \text{Re} H^6 H_z + \frac{H^3}{3 \text{Bo}} \left(\frac{H_z + \eta_z}{R^2} + H_{zzz} + \eta_{zzz} \right) - \frac{H^3(H + 4\eta)}{6R} \right) \right) = 0. \quad (4.29)$$

If we now consider the flow rate at $O(\epsilon^{-1})$ and $O(1)$, which is calculated from

$$\hat{q} = \int_0^h \left(\frac{R}{\epsilon} + \eta + r \right) (w_0 + \epsilon w_1) dr \quad (4.30)$$

substituting in the velocities (4.10), (4.17) and integrating gives us

$$\frac{\epsilon \hat{q}}{R} = \frac{H^3}{3} + \epsilon \left(\frac{2}{15} \text{Re } H^6 H_z + \frac{H^3}{3 \text{Bo}} \left(\frac{H_z + \eta_z}{R^2} + H_{zzz} + \eta_{zzz} \right) - \frac{2}{3R} H^3 \eta - \frac{1}{6R} H^4 \right). \quad (4.31)$$

So equation (4.29) can be rewritten as

$$m_t + \hat{q}_z = 0. \quad (4.32)$$

If we scale out the $\frac{\epsilon}{R}$ by setting $q = \frac{\epsilon \hat{q}}{R}$, we have

$$H_t + q_z = 0. \quad (4.33)$$

Comparing equation (4.29) with the smooth cylinder equivalent, equation (4.22), we see that the wall introduces additional surface tension terms and a term due to the first order correction of gravity. Setting $\eta = 0$, we recover equation (4.22). We can compare our equation with that found by Tseluiko et al. (2013), which models topography down an inclined slope. If we consider a vertical plane, by taking $R \rightarrow \infty$ in our equation and $\theta = \frac{\pi}{2}$ in the equation from Tseluiko et al. (2013), we find that these equations are equivalent. Also, to note is that the term in our equation from the surface tension due to the azimuthal curvature of the cylinder, appears to have a similar effect as that of gravity on a fluid flowing on the underside of a sloping ceiling in Tseluiko et al. (2013)'s equation. The final wall term of (4.29) is an additional shear term caused by the fluid flowing down a cylinder. The difference between this equation (4.29) and the one derived in chapter 3, equation (3.13), is that here the surface tension terms are now $O(\epsilon)$, which means in this chapter we also see the effects of inertia, and a correction to gravity. To retain equation (3.13)

from equation (4.29), we can set $\text{Bo} = \epsilon \hat{\text{Bo}}$. As ϵ is small, the other $O(\epsilon)$ terms do not significantly affect the fluid thickness and so only the leading order terms are retained.

While equation (4.29) is easier to solve numerically than equation (4.26), we wish to show our results using the more physical property of the fluid thickness. To get back the fluid thickness, we must solve the quadratic of equation (4.28). Here we take the positive root, as the fluid thickness can not be negative. We find

$$h = -\left(\eta + \frac{R}{\epsilon}\right) + \sqrt{\left(\eta + \frac{R}{\epsilon}\right)^2 + \frac{2RH}{\epsilon}}. \quad (4.34)$$

As the first term in the root is $O(\epsilon^{-2})$ it is ϵ^{-1} larger than the second term. Therefore, we can Taylor expand the root, to find that

$$h = H - \frac{\epsilon}{R} \left(H\eta + \frac{H^2}{2} \right). \quad (4.35)$$

4.3 Steady States

We can find steady states of the system by setting $H_t = 0$ in equation (4.33). This tells us that the flow rate doesn't depend on z as now $q_z = 0$. Therefore, we have

$$q = \frac{H^3}{3} + \epsilon \left(\frac{2}{15} \text{Re} H^6 H_z + \frac{H^3}{3 \text{Bo}} \left(\frac{H_z + \eta_z}{R^2} + H_{zzz} + \eta_{zzz} \right) - \frac{H^3(H + 4\eta)}{6R} \right). \quad (4.36)$$

We can see that for a constant radius (i.e $\eta = 0$), a constant fluid thickness is a solution to equation (4.22). Setting the steady state fluid thickness $h_0 = 1$, we find from equation (4.28) that $H = H_0 = 1 + \frac{\epsilon}{2R}$. In this case, we find that the flow rate from equation (4.36) is $q = \frac{1}{3} \left(1 + \frac{\epsilon}{R} \right) + O(\epsilon^2)$.

4.3.1 Small ϵ

As ϵ is small, we can perform an asymptotic expansion on the fluid thickness. Therefore we let $h = h_0 + \epsilon h_1$ then from equation (4.28), we find

$$H = h_0 + \epsilon \left(h_1 + \frac{h_0}{2R} (2\eta + h_0) \right) + O(\epsilon^2) \quad (4.37)$$

Substituting this into equation (4.36), with $q = \frac{1}{3} \left(1 + \frac{\epsilon}{R} \right)$, we find that from the leading order terms $h_0 = 1$ and from the $O(\epsilon)$ terms that

$$h_1 = -\frac{1}{3R^2 \text{Bo}} (\text{Bo} R \eta + \eta_z + R^2 \eta_{zzz}). \quad (4.38)$$

For a sinusoidal wall of the form,

$$\eta = \delta \cos kz \quad (4.39)$$

we would expect the fluid disturbance to be of the form

$$h_1 = A \cos(kz - \theta), \quad (4.40)$$

where $k = \frac{2\pi}{L}$. Substituting equations (4.40) and (4.39) into equation (4.38), the phase shift is found to be

$$\tan \theta = \frac{8\pi^3 R^2 - 2\pi L^2}{R \text{Bo} L^3} \quad (4.41)$$

and the amplitude is

$$A = -\frac{\delta}{3R} \sec \theta. \quad (4.42)$$

Here the amplitude depends on the phase shift. As $A > 0$ by definition, this means that $\sec \theta < 0$ and so $\theta \in \left(\frac{\pi}{2}, \frac{3\pi}{2} \right)$. Looking at the phase shift, we see that for $L > 2\pi R$ the fluid

maximum is downstream of the wall maximum $\theta < \pi$, and for $L < 2\pi$ $\theta > \pi$. In the limits $L \rightarrow 0$, we have $\theta = \frac{3\pi}{2}$, which means that in this limit $A \rightarrow \infty$. In the limit $L \rightarrow \infty$, we find $\theta \rightarrow \pi$ and so $A \rightarrow \frac{\delta}{3R}$.

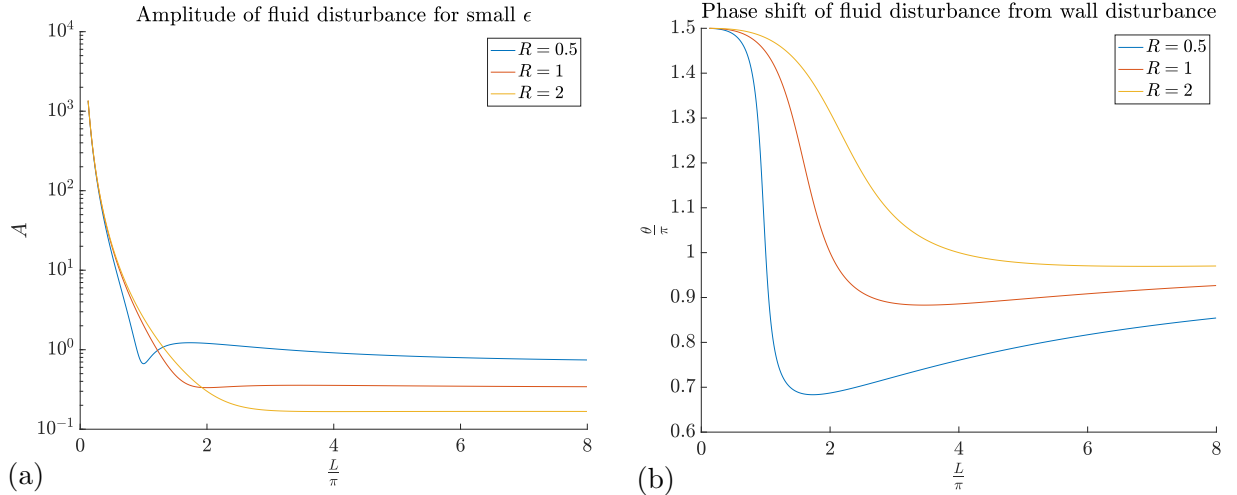


Figure 4.3: How the wavelength affect the amplitude (a) and the phase shift (b) for small ϵ

Figure 4.3 further shows how the wavelength of the wall affects the amplitude and phase shift of the fluid disturbance. From (a) we see that like in chapter 3 the amplitude of the fluid disturbance is more significant for the $L < 2\pi R$ case. However, unlike in chapter 3 the phase shift reduces from $\theta = \frac{3\pi}{2}$ as we increase the wavelength. Increasing the wavelength for $L > 2\pi R$ the phase shift initially continues to decrease, up until some point where it increases back up to $\theta = \pi$. These figures also shows that in the longer wavelength cases that for smaller R the fluid is generally shifted more upstream, and has a bigger amplitude. For small L , we see that the amplitude grows very large, however for equation (4.36) to hold we are assuming $L = O(1)$.

4.3.2 Small amplitude walls

If we start with the smooth cylinder case, we can find a steady state to the fluid thickness h_0 from equation (4.22). Adding a small perturbation to the wall, so that

$$\eta = \delta\hat{\eta} \quad (4.43)$$

where $\delta \ll h_0$, then we would expect the steady state fluid thickness to be of the form

$$h = h_0 + \delta \hat{h}. \quad (4.44)$$

We also expect the perturbation to H to be of this form

$$H = H_0 + \delta \hat{H} \quad (4.45)$$

From equation (4.28), we find by comparing leading order terms in δ that

$$H_0 = h_0 + \frac{\epsilon h_0^2}{2R} \quad (4.46)$$

and comparing $O(\delta)$ terms gives

$$\hat{H} = \left(\hat{h} + \frac{\epsilon h_0}{R} (\cos kz + \hat{h}) \right). \quad (4.47)$$

Note ϵ terms are also considered small, however they are part of the smooth cylinder steady state and so are retained. Overall we are looking at how this wall perturbation causes a perturbation to the fluid thickness. Looking at the smooth cylinder case (4.22), we see that $h_0 = 1$ is a steady state. If we consider this to be steady state we perturb, then $H_0 = 1 + \frac{\epsilon}{2R}$ is also a constant. Substituting equations (4.43), (4.45) into (4.36), the leading order cancels as it is a steady state, and at $O(\delta)$ we find

$$\hat{H} + \epsilon \left(\frac{2}{15} \text{Re } H_0^4 \hat{H}_z + \frac{H_0}{3 \text{Bo}} \left(\frac{\hat{H}_z + \eta_z}{R^2} + \hat{H}_{zzz} + \eta_{zzz} \right) - \frac{2H_0}{3R} (\hat{H} + \hat{\eta}) \right) = 0. \quad (4.48)$$

For a wall $\hat{\eta} = \cos(kz)$ we look for periodic solutions. We can expect \hat{H} to take the form

$$\hat{H} = A \cos(kz - \theta) \quad (4.49)$$

where A is the amplitude relative to the wall amplitude and θ represents the phase shift.

These are given as

$$A = 5\epsilon \left(\frac{(4R^2 \text{Bo}^2 + (k - k^3 R^2)^2)}{225 \text{Bo}^2 R^4 + 150\epsilon \text{Bo}^2 R^3 + \epsilon^2(25R^2 \text{Bo}^2 + k^2(5 + (2 \text{Bo Re} - 5k^2)R^2)^2)} \right)^{\frac{1}{2}}, \quad (4.50)$$

$$\tan \theta = \frac{\text{Bo } kR(15R - 15k^2 R^3 + \epsilon(15 + (4 \text{Bo Re} - 15k^2)R^2))}{30 \text{Bo}^2 R^3 + \epsilon(10 \text{Bo}^2 R^2 - k^2(k^2 R^2 - 1)((5k^2 - 2 \text{Bo Re})R^2 - 5))}. \quad (4.51)$$

To get the phase shift, the branch of arctan is chosen so that the amplitude $A > 0$. This is calculated by making use of

$$\hat{H} = A \cos(kz - \theta) = a \cos kz + b \sin kz \quad (4.52)$$

where $a = A \cos \theta$, $b = A \sin \theta$. So if $a < 0$, we know $\cos \theta < 0$ and so $\theta \in (\frac{\pi}{2}, \frac{3\pi}{2})$. When finding other steady states, we use these small amplitude walls as an initial guess of the fluid thickness for Matlab's function `fsolve`.

From \hat{H} we can calculate the fluid thickness. We would expect the fluid thickness to also be of the form

$$\hat{h} = B \cos(kz - \varphi). \quad (4.53)$$

Making use of the definition of \hat{H} in equation (4.47), we find

$$\tan \varphi = \frac{RA \tan \theta}{RA - \epsilon \sec \theta}, \quad (4.54)$$

$$B = \frac{AR \sin \theta}{(R + \epsilon) \sin \varphi}. \quad (4.55)$$

For small ϵ we find to leading order that

$$\tan \theta = \frac{k - k^3 R^2}{2 \text{Bo } R} \quad (4.56)$$

$$\begin{aligned}
 A &= \frac{\epsilon}{3 \text{Bo} R^2} \sqrt{4R^2 \text{Bo}^2 + (k - k^3 R^2)^2} \\
 &= \frac{2\epsilon}{3R} \sec \theta.
 \end{aligned}
 \tag{4.57}$$

Using equations (4.54)-(4.55), we can find the corresponding amplitude and phase shift for the fluid thickness at small ϵ

$$\tan \varphi = -2 \tan \theta \tag{4.58}$$

$$= \frac{k - R^2 k^3}{\text{Bo} R}, \tag{4.59}$$

$$B = -\frac{\epsilon}{3R} \sec \varphi. \tag{4.60}$$

Here we have recovered the fluid disturbance that we found for small ϵ , described by equations (4.41)-(4.42). Noting in this limit, the Reynolds number no longer has any effect.

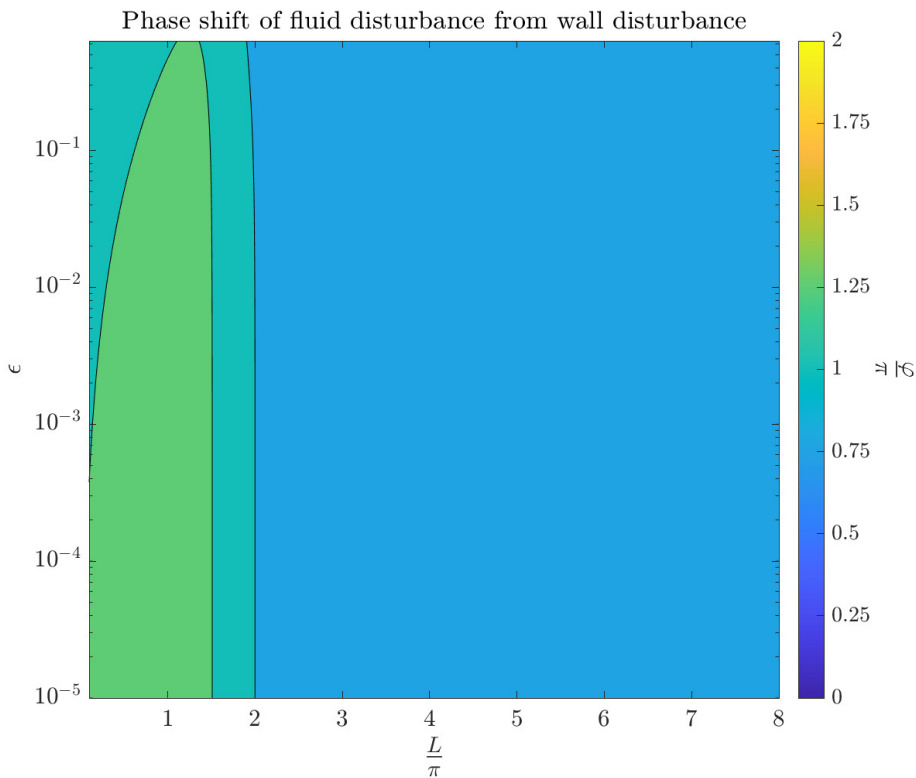


Figure 4.4: Phase shift of the fluid thickness disturbance from the wall disturbance, depending on the wavelength L and ϵ . Here $\text{Re}, R, \text{Bo} = 1$.

Figure 4.4 shows the phase shift φ of the fluid thickness from the wall. Here the Reynolds number, Bond number and radius are set to 1. The contour lines occur at $\frac{3\pi}{4}$ and π . We can see that $L = 2\pi R$ is an important boundary, like in chapter 3. This line has been slightly deflected left of $2\pi R$ as can be seen for $\epsilon > 0.1$. Looking at equation (4.51), we find that at $L = 2\pi R$

$$\tan \theta = \frac{2\epsilon \text{Re}}{15R - 10\epsilon} \quad (4.61)$$

which is the effect of the inertial term. Like in chapter 3 we see that for $L > 2\pi R$ we have $\frac{\pi}{2} < \varphi < \pi$, meaning the fluid is thickest after the wall peak. For $L < 2\pi R$ the opposite is true with $\pi < \varphi < \frac{3\pi}{2}$, resulting in the fluid being thickest before the wall peak. However, now $\theta = \pi$ at the boundary and decreases across it. This is as a result of the additional wall term at this order. To recover the results from chapter 3, we take $\text{Bo} = \epsilon \mathcal{B}$. If we then take equation (4.51) at leading order, we recover equation (3.18).

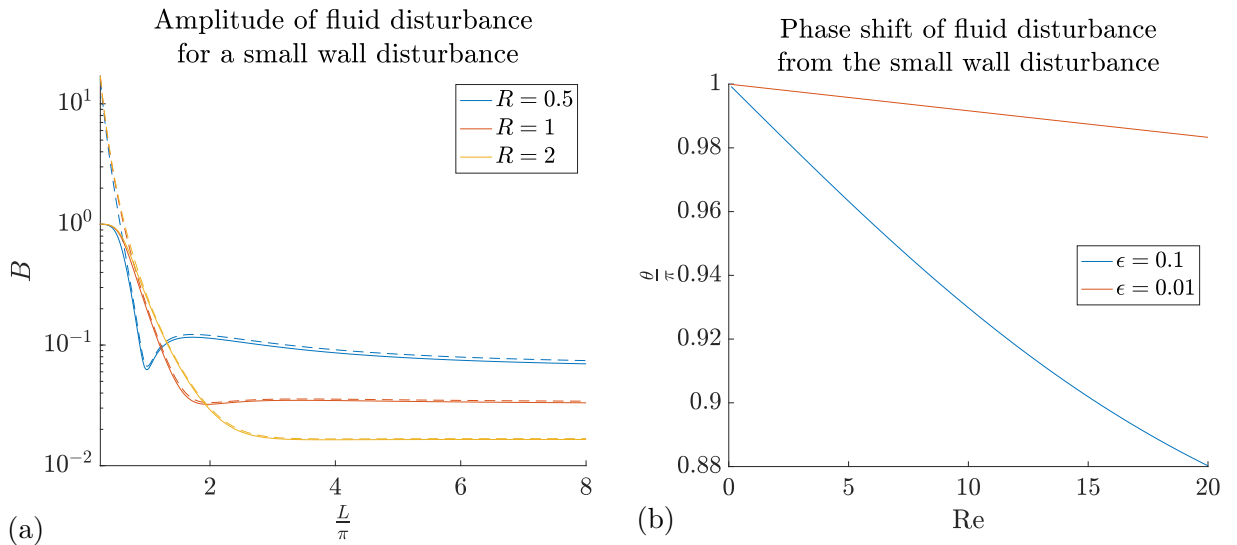


Figure 4.5: How the parameters affect the fluid disturbance. (a) shows the effect of the wavelength on the amplitude for different radii, here $\text{Re}, \text{Bo} = 1$ and $\epsilon = 0.1$. The dotted lines are the small ϵ approximation from equations (4.41)-(4.42) (b) shows how the phase shift is deflected from π when $L = 2\pi, R = 1, \text{Bo} = 1$.

Figure 4.5 shows how the wavelength and the Reynolds number can affect the fluid disturbance. From (a) we have the amplitude of the fluid thickness, against the wall wavelength. The dotted lines in this figure are the amplitude of the small ϵ approximation

described by equations (4.41)-(4.42). We see that the amplitude is generally less than the small ϵ approximation, as $O(\epsilon^2)$ terms must act to decrease the amplitude. We also see in this case that the amplitude does not exceed 1, meaning the fluid disturbance is never larger than the wall disturbance. However, for small wavelengths, the small ϵ approximation has the fluid disturbance being around 10 times that of the wall amplitude. For $L > 2\pi$ the amplitudes settle to $O(\epsilon)$, as here $\epsilon = 10^{-1}$. We also see that increasing the radius decreases the amplitude. Figure (b) shows how the Reynolds number contributes to the phase shift in the case where $R = 1, L = 2\pi$, as highlighted in equation (4.61). As this depends on ϵ we do need a fairly large ϵ to see the effect. Here we see that the fluid is deflected to be thickest just before the wall trough.

4.3.3 Nonlinear steady solutions

We can also seek steady solutions (H^*) of equation (4.29) numerically. The fluid thickness that relates to these steady state solution will be denoted by h^* . From equation (4.33), we see that for steady states we need to find

$$q_z = 0 \tag{4.62}$$

meaning that we wish to solve

$$q = q_0 \tag{4.63}$$

where q_0 is some constant. In order to find the constant flow rate, we impose the condition that the total volume of the fluid is fixed. As we wish to see the disturbance to the fluid thickness, we set

$$\frac{1}{L} \int_0^L h^* dz = 1. \tag{4.64}$$

This however means that solutions with different amplitude walls will have a different mass, as integrating H from equation (4.28) gives

$$\frac{1}{L} \int_0^L H^* dz = 1 + \frac{\epsilon}{RL} \int_0^L \eta h^* + h^{*2} dz \quad (4.65)$$

To numerically solve equation (4.29), we follow steps described in section 2.5. We have split the domain z into 256 spatial steps and our derivatives are calculated using a pseudo-spectral technique. We have imposed periodic boundary conditions and have used (4.49) as an initial guess. This is then solved using MATLAB function `fsolve`. Solving this equation gives us H^* which is related to the mass density, however we wish to find the more physical property of fluid thickness. Therefore, we convert H^* back into the fluid thickness by making use of equation (4.34).

For this problem, as we wish to see the nonlinear effects of equation (4.36), we set $\epsilon = 0.1$. Again we will set the wall to be

$$\eta = \delta \cos\left(\frac{2\pi z}{L}\right). \quad (4.66)$$

In these examples we will set $R = 1$, so that the fluid thickness does not vary substantially between results. As the fluid thickness is not changing, the Bond number and Reynolds number should also stay constant, and so these will also be set to 1.

To examine the effect of the wall disturbance, we will consider: the amplitude of the disturbance to the fluid thickness, which is defined as

$$A = \frac{h^*_{\max} - h^*_{\min}}{2} \quad (4.67)$$

and the phase shift of the fluid disturbance from the wall disturbance, which is defined as the normalised distance of the maximum thickness away from the wall maximum

$$\theta = 2\pi \frac{z_{\max}}{L}. \quad (4.68)$$

Noting that since the wall is a cosine, the wall maximum is located at $z = 0$.

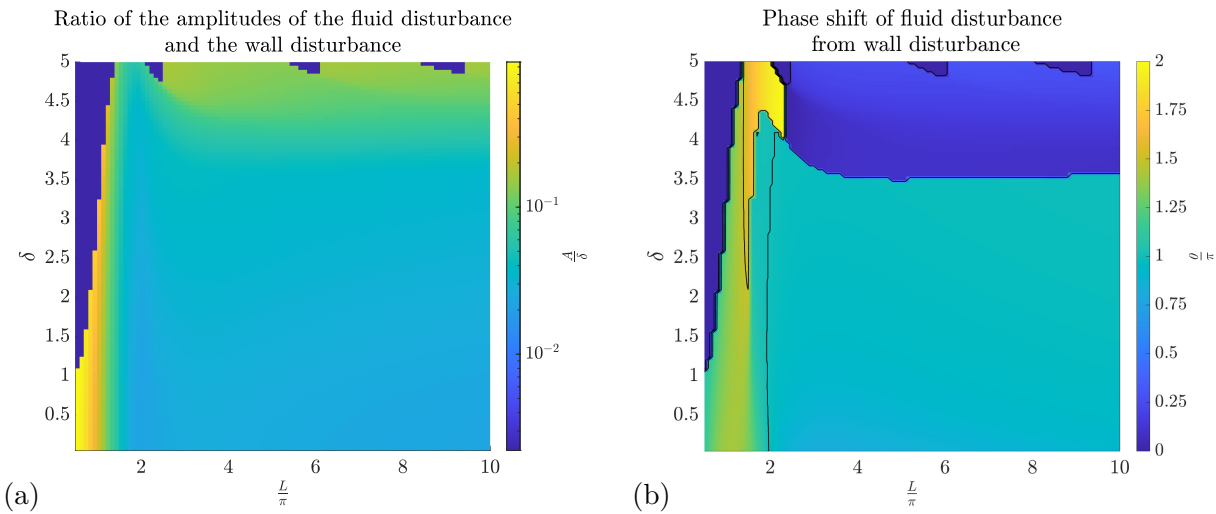


Figure 4.6: How the wall shape affect the disturbance to the fluid thickness. (a) shows the amplitude of the fluid disturbance compared to the amplitude of the wall. (b) shows the phase shift of the fluid disturbance from the wall disturbance.

Figure 4.6 shows how walls with different amplitudes and wavelengths affect the disturbance to the fluid thickness. In both plots, the dark blue region is where no steady state solutions were found. Subfigure (a) shows the ratio between the amplitude of the fluid and the amplitude of the wall. We can see that this value is always less than 1, so we know the fluid disturbance is smaller than the wall disturbance. We see for the vast majority of wavelengths and amplitude this ratio is around 3×10^{-2} , with larger amplitude disturbances occurring for small L or large δ . We also see a faint blue line around $L = 2\pi$, showing that the amplitude of the fluid along this line is even smaller.

Subfigure (b) shows the phase shift of the fluid disturbance from the wall disturbance. Contours have been overlaid to show every $\frac{\pi}{2}$. For $\delta > 3.5$ and $L > 2\pi$ we have a region where $0 < \theta < \frac{\pi}{2}$. Here it is typically closer to 0 than $\frac{\pi}{2}$, showing that the fluid is thickest just after the wall maximum. For $L > 2\pi$ and $\delta < 3.5$ we have a region where $\frac{\pi}{2} < \theta < \pi$, although again it typically is closer to π . For $L < 2\pi$ and $\delta < 4.5$ we have a region where $\pi < \theta < \frac{3\pi}{2}$. Here the phase shift can be seen to increase as L increases up to 1.5π and then decreases down to π as L increases to 2π . For $L < 2\pi$ and $\delta > 4.5$ we find the region where $\frac{3\pi}{2} < \theta < 2\pi$. This region contains a thin section around $L = 1.5\pi$ where the

amplitude can be as small as 2.

The boundary between the fluid being thickest upstream of the wall maximum ($\theta > \pi$) and the fluid thickest downstream ($\theta < \pi$) starts at $L = 2\pi$ for $\delta = 0$ and then shifts to higher wavelengths for greater amplitudes. This boundary exists due to the wall effect inside the pressure term

$$\frac{\eta_z}{R^2} + \eta_{zzz} = \delta \frac{4\pi^2}{L^2} \left(\frac{4\pi^2}{L^2} - \frac{1}{R^2} \right) \sin \left(\frac{2\pi z}{L} \right). \quad (4.69)$$

For $L < 2\pi R$ equation (4.69) is positive and for $L > 2\pi R$ (4.69) is negative. This term vanishes for $L = 2\pi R$ in which case the only difference of equation (4.36) from the smooth cylinder equation (4.22) is the term

$$-\epsilon \frac{\partial}{\partial z} \left(\frac{2H^3\eta}{3R} \right). \quad (4.70)$$

This term is what shifts the boundary to the right.

Increasing the amplitude of the wall will amplify the nonlinear effects of equation (4.36). As the amplitude of the fluid disturbance is generally small, we will look at plots of the fluid thickness rather than the fluid profile. Figure 4.7 looks at the normalised fluid disturbance for different amplitude walls. Figure (a) has a wavelength of $L = \pi$. Here we see that the amplitude of the fluid disturbance is roughly 0.2δ . Increasing the wall amplitude shifts the maximum fluid thickness left, but also the minimum fluid thickness right. For $\delta = 2$ we see that the minimum has been slightly flattened. The normalised amplitude of the fluid disturbance also increases as the wall increases.

For (b) the wavelength is $L = \frac{3\pi}{2}$. The amplitude of the disturbance here is around 0.04, much smaller than the $L = \pi$ case. In this case, increasing the wall amplitude from $\delta = 0.1$ to 2 decreases the fluid maximum. For the larger wall amplitudes the disturbance shows the nonlinear effects with the $\delta = 2$ case having quite a flat maximum and the $\delta = 4$ case exhibiting a secondary peak at $z = 0.5L$. In both these cases, the fluid is thickest for $z > \frac{3}{4}L$.

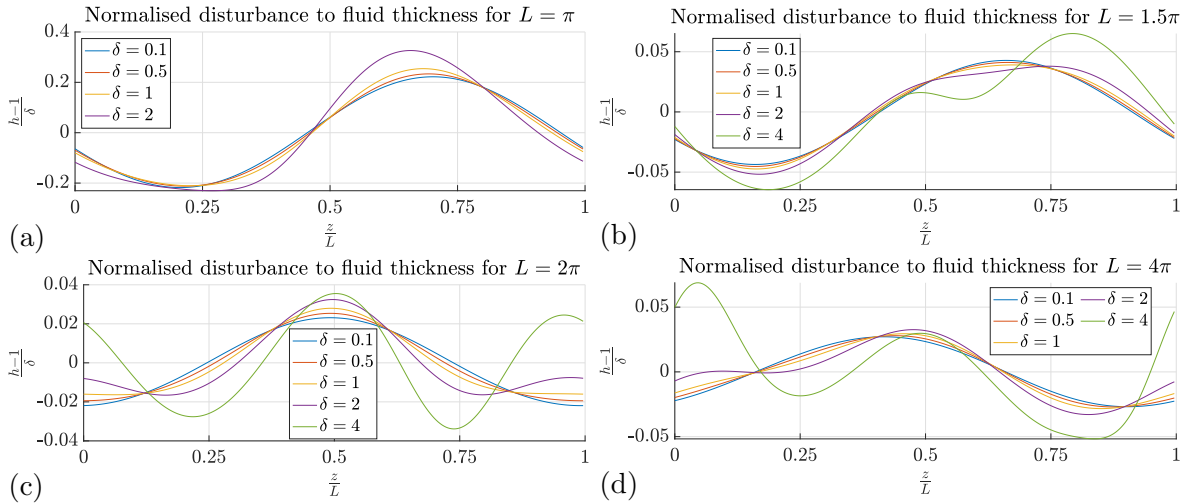


Figure 4.7: Normalised disturbance to the fluid thickness for different amplitude walls. Here $R = \text{Bo} = \text{Re} = 1$. The subplots have wavelengths (a) $L = \pi$, (b) $L = \frac{3\pi}{2}$, (c) $L = 2\pi$ and (d) $L = 4\pi$.

For (c) the wavelength is $L = 2\pi$. Here the maximum fluid thickness increases with wall amplitude again. Increasing the wall amplitude, we see a secondary fluid maximum form. For the $\delta = 4$ case we have the fluid thickest in the wall trough but also thicker just before the wall peak.

For (d) the wavelength is $L = 4\pi$. The small amplitude results are generally quite similar to the $L = 2\pi$ results with the maximum shifted slightly more left. For the $\delta = 4$ case, we again have 2 peaks, at the minimum of the wall and just after the maximum of the wall. In this case, the dominant peak is the one just after the wall maximum.

We will now vary the other parameter to see their effect on the fluid thickness. If the parameter is not being varied, we have $\text{Re} = \text{Bo} = \delta = R = 1$, $\epsilon = 0.1$. Again we will look at the cases $L = \pi, 2\pi, 4\pi$ to see the effect of the parameters where the different pressure terms dominate. While the Bond number and the Reynolds number depend on the fluid thickness, if we were to have a fixed fluid thickness then changing the Bond number can be viewed as using a fluid with a different surface tension. Similarly, changing the Reynolds number can be viewed as using a fluid with a different viscosity.

In figure 4.8 we look at varying the Reynolds and Bond numbers. In (a) we show the effect of the Reynolds number on the fluid thickness. The values of 0.3, 1, 3, 10 were

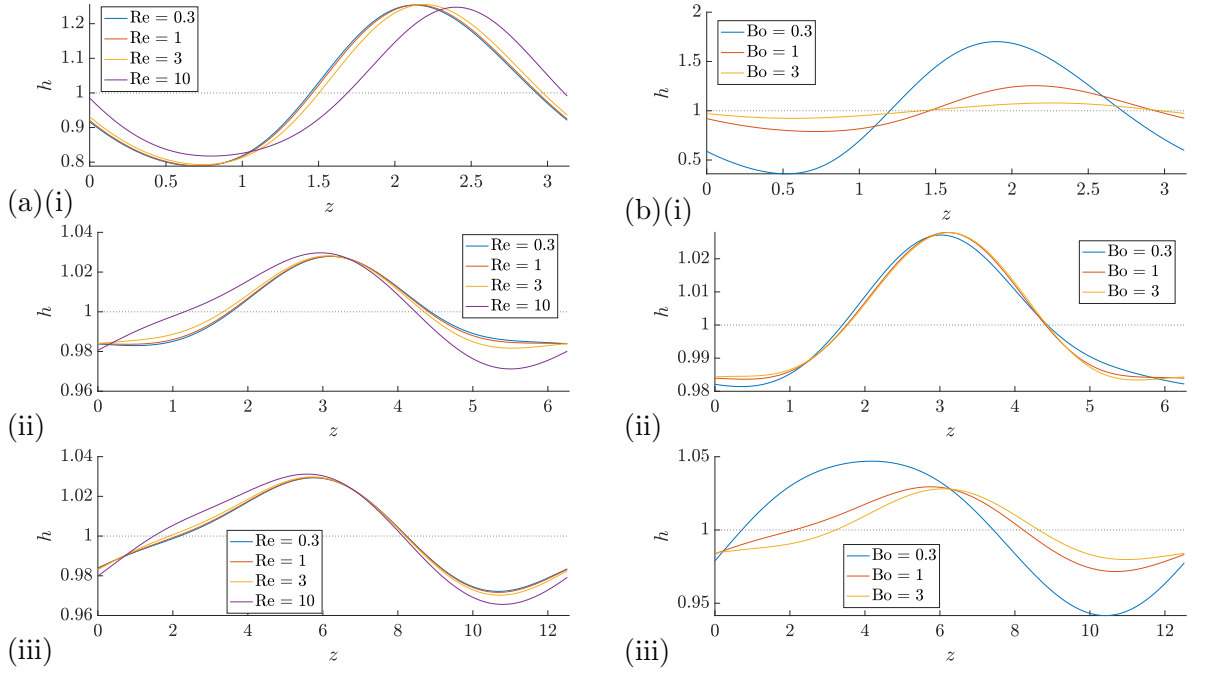


Figure 4.8: Fluid thickness for different (a) Reynolds numbers and (b) Bond numbers. The subplots have wavelengths (i) $L = \pi$, (ii) $L = 2\pi$ and (iii) $L = 4\pi$.

chosen as these are approximately $\epsilon^{0.5}$, ϵ^0 , $\epsilon^{-0.5}$, ϵ^{-1} . We see here that the Reynolds number generally does not have much of an effect on the fluid thickness, with the amplitude remaining similar. In the $L = \pi$ case, we see that $\text{Re} = 10$ causes a noticeable phase shift, with the fluid becoming thicker more downstream.

In (b) we see how the Bond number affects the fluid thickness. Here we see that for the $L = 2\pi$ case the fluid thickness hardly changes. In this case, as the wall terms cancel, the only terms that depend on the Bond number are the derivatives of the fluid thickness. As the fluid thickness has a small amplitude disturbance, these derivatives are negligible. In the other two cases, we see that for smaller Bond numbers, we have a larger amplitude fluid disturbance. We also see that increasing the Bond number shifts the maximum thickness so that it is more downstream.

The parameters R and ϵ both depend on the dimensional wavelength, so changing these can also be viewed as changing L . However, these parameters will also change if the mean fluid thickness \tilde{h}_0 changes, so we can view this as changing the fluid thickness. Figure 4.9 shows how changing the radius and ϵ affect the flow. In (a) we look at changing

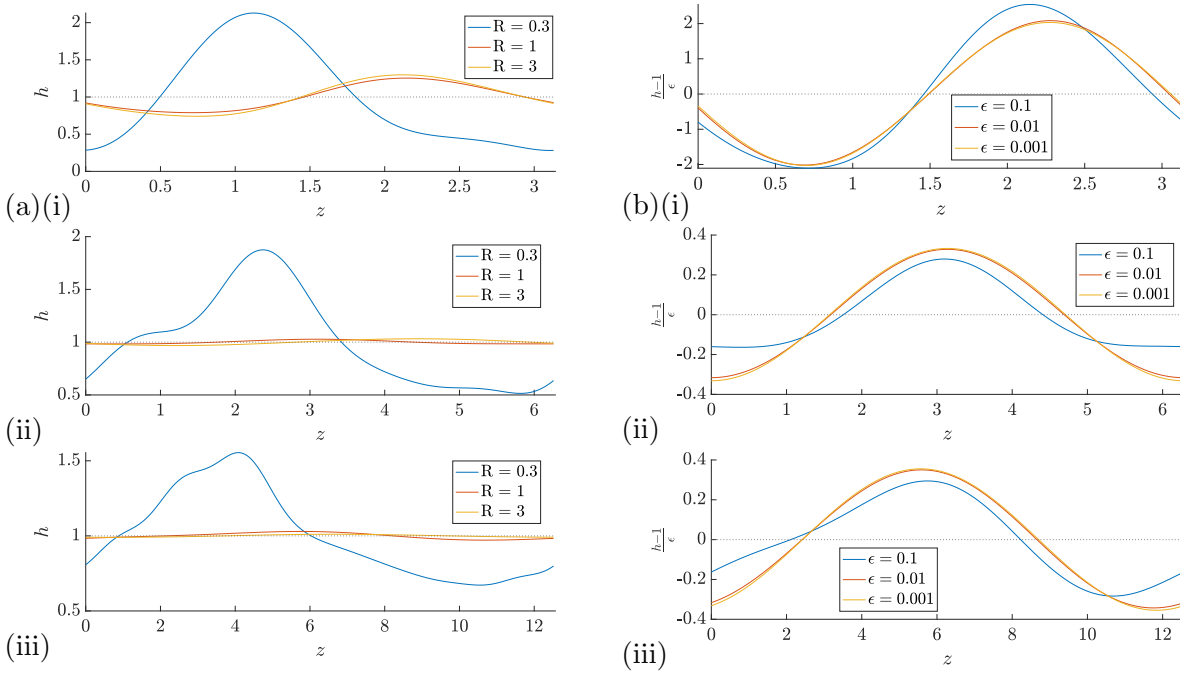


Figure 4.9: Fluid thickness for different (a) radii and (b) ϵ . The subplots have wavelengths (i) $L = \pi$, (ii) $L = 2\pi$ and (iii) $L = 4\pi$

the radius. Here we see that the smaller the radius, the larger the amplitude of the fluid disturbance. However, in the $L = \pi$ case, we find that $R = 3$ leads to a larger amplitude than $R = 1$. Due to R appearing in equation (4.69) figures (i)-(iii) no longer show where the different wall terms dominate. $\frac{\eta_z}{R^2}$ is always the dominant term for $R = 0.3$ and η_{zzz} is the dominant term for $R = 3$. This is why the fluid maximum always appears downstream of the wall maximum for $R = 0.3$ and always upstream for $R = 3$. We see that for smaller R the fluid thickness appears more nonlinear, with a secondary minimum and maximum appearing for small L , and a very wide minimum for larger L .

In (b) we see the effect of ϵ on the fluid thickness. We have normalised the amplitude to make the solutions more directly comparable. For $L = \pi$ we see that the amplitude is larger for bigger ϵ and the fluid disturbance is shifted to the right. However, in the $L = 2\pi, 4\pi$ cases the smaller ϵ is, the larger the amplitude. For small ϵ the shape of the fluid disturbance appears more sinusoidal as suggested in section 4.3.1.

4.4 Linear Stability Analysis

For the smooth cylinder case, we can perform linear stability analysis. The smooth cylinder equation is

$$h_t + \frac{\partial}{\partial z} \left(\frac{h^3}{3} + \epsilon \left(\frac{2}{15} \text{Re} h^6 h_z + \frac{h^3}{3 \text{Bo}} \left(\frac{h_z}{R^2} + h_{zzz} \right) - \frac{h^4}{12R} \right) \right) = 0. \quad (4.71)$$

By taking a small perturbation of the fluid thickness, so that $h = 1 + He^{ikz-i\omega t}$ where $|H| \ll 1$, we find

$$\omega = ik^2\epsilon \left(\frac{1}{3 \text{Bo} R^2} + \frac{2}{15} \text{Re} - \frac{k^2}{3 \text{Bo}} \right) + k \left(1 - \frac{\epsilon}{3R} \right). \quad (4.72)$$

Separating into real and imaginary parts, so $\omega = \omega_r + i\omega_i$, we obtain

$$\omega_r = k \left(1 - \frac{\epsilon}{3R} \right) \quad (4.73)$$

$$\omega_i = k^2\epsilon \left(\frac{1}{3 \text{Bo} R^2} + \frac{2}{15} \text{Re} - \frac{k^2}{3 \text{Bo}} \right). \quad (4.74)$$

This will be stable if $\omega_i < 0$, so this tells us that the inertia and the surface tension due to the azimuthal curvature are destabilising the fluid, and the surface tension due to axial curvature stabilises the fluid.

The neutral stability curve lies on

$$k_0 = \sqrt{\frac{1}{R^2} + \frac{2}{5} \text{Bo} \text{Re}}, \quad (4.75)$$

with solutions stable if $k > k_0$ and unstable if $k < k_0$. The phase speed is $\frac{\omega_r}{k}$ and so we see that increasing the radius works to slow the speed at which the disturbance to the fluid thickness travels.

In the case where we have a wall disturbance, the steady state solution is no longer a

constant. Therefore, we now consider a small perturbation of the form

$$H = H^*(z) + \hat{H}(z)e^{-\omega t} \quad (4.76)$$

where $|\hat{H}(z)| \ll 1$. This can be substituted into (4.29).

$$\begin{aligned} \omega \hat{H} = & \frac{\partial}{\partial z} \left(H^{*2} \hat{H} + \epsilon \left(\frac{2}{15} \operatorname{Re} \left(6H^{*5} H^*_z \hat{H} + H^{*6} \hat{H}_z \right) + \frac{H^{*3}}{3\operatorname{Bo}} \left(\frac{\hat{H}_z}{R^2} + \hat{H}_{zzz} \right) \right) \right) \\ & + \epsilon \frac{\partial}{\partial z} \left(\frac{H^{*2} \hat{H}}{\operatorname{Bo}} \left(\frac{H^*_z + \eta_z}{R^2} + H^*_{zzz} + \eta_{zzz} \right) - \frac{H^{*2} \hat{H}}{3R} (2H^* + 6\eta) \right). \end{aligned} \quad (4.77)$$

Here we compute the spatial derivatives of \hat{H} using finite differences. Then our equation becomes an eigenvalue problem, which can be solved by using MATLAB's function `eig`, as outlined in section 2.5. This returns the eigenvalues and corresponding eigenvectors,

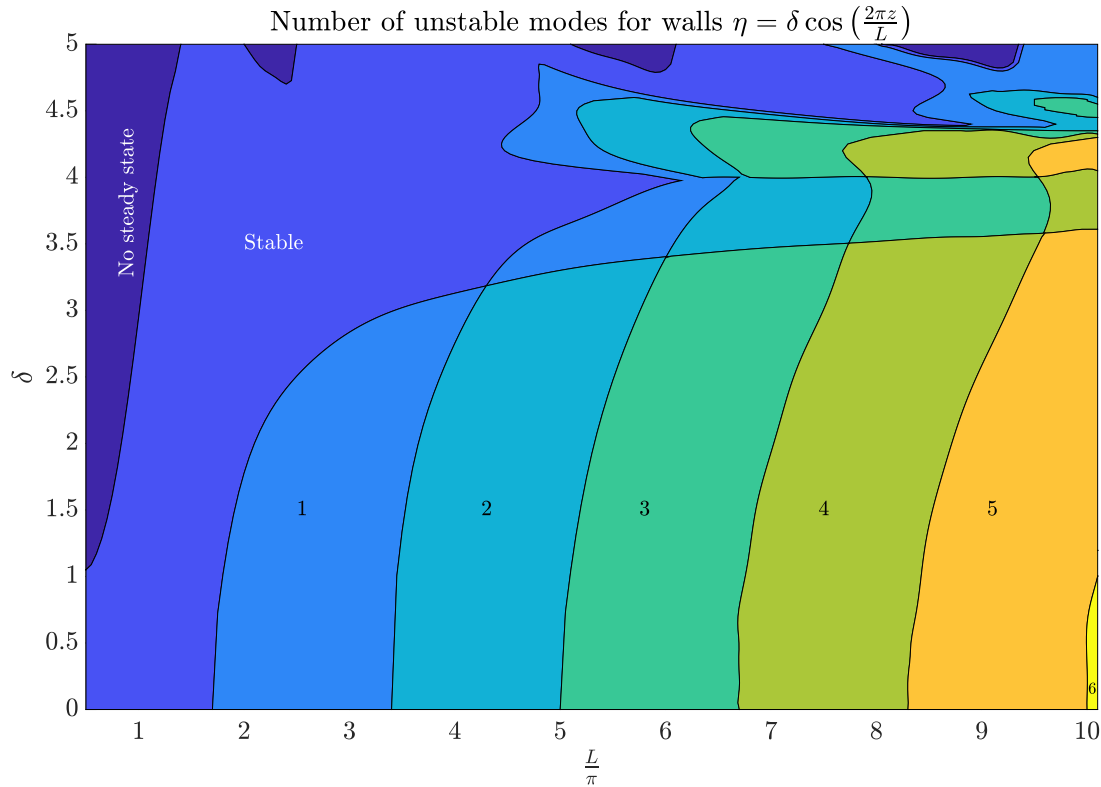


Figure 4.10: The number of unstable modes of the steady state for walls of the form $\eta = \delta \cos\left(\frac{2\pi z}{L}\right)$ where $R = \operatorname{Bo} = \operatorname{Re} = 1$, $\epsilon = 0.1$.

allowing us to determine the number of unstable modes by looking at the eigenvalues which have negative real part. The imaginary part of these eigenvalues will tell us a wave

speed for these eigenvectors.

Figure 4.10 shows the number of unstable modes for walls of different amplitude and wavelength. We see that increasing the amplitude of the wall causes the unstable modes to appear at longer wavelengths. There is a section between $\delta = 3$ and $\delta = 4$, where the steady states are seemingly more stable, with there being one fewer unstable mode than those with smaller amplitude, or an amplitude between 4 and 4.5. Increasing the amplitude to 5 we find certain wavelengths where no solution can be found. If we look at the $\delta = 0$ cases, we see that the m^{th} unstable modes occur at $L = 2\pi m \sqrt{\frac{5}{7}}$ as expected from equation (4.75). This equation suggests that increasing the radius will mean that additional unstable modes will appear at longer wavelengths. However, if the Bond number or the Reynolds number is increased we would expect to find unstable modes appearing at shorter wavelengths.

4.5 Time Dependent Solutions

We wish to see how the fluid thickness evolves in time. To do this, we will be solving (4.29) and converting back to the fluid thickness by using (4.34). Equation (4.29) is used instead of (4.33) in order to conserve mass in the system. As described in section 2.5, we have discretised z into 256 spatial steps, using a pseudo-spectral technique for the spatial derivatives. For the temporal integration, MATLAB routine `ode15s` has been used. For these calculations, we have considered $\epsilon = 0.1$, $R = \text{Bo} = \text{Re} = 1$. Again for these simulations we take a sinusoidal wall

$$\eta = \delta \cos\left(\frac{2\pi z}{L}\right). \quad (4.78)$$

For these simulations we consider the initial fluid thickness to be

$$h_0 = 1 + 0.1 \sin\left(\frac{2\pi z}{L}\right). \quad (4.79)$$

From this and equation (4.34), we calculate the initial value for H . Solutions were simulated for wavelengths between $L = \pi$ and $L = 10\pi$ and amplitudes from $\delta = 0$ to $\delta = 5$. We have initially solved most cases for 500 time units to get a basic understanding of the solutions. Certain cases were integrated further to 2000 time units to get a more complete understanding of the dynamics.

From this we found that the Floquet analysis, as seen in figure 4.10, gives a good approximation of the behaviour. The boundaries between the regions are less clear for the regions with larger δ . Similar to the discussion in chapter 3, we find that where the Floquet analysis suggests the steady state is stable, the solution will oscillate down to this steady state. Where there is one unstable mode the solution generally becomes a time periodic wave, and if there are more unstable modes then we get quasi-periodic or non-periodic solutions. To characterise the solutions we make use of the norm

$$\|H\|_2 = \sqrt{\frac{1}{L} \int_0^L H^2 dz}. \quad (4.80)$$

Here we are using $\|H\|_2$ instead of $\|h\|_2$, as this better relates the norm to the mass of the fluid.

4.5.1 Different regimes

Figure 4.11 shows some examples of the different types of solutions. Here we have used $\|H\|_2$ to highlight the differences between the solution types. Subfigures (a) shows a solution where the steady state is stable. Here we can see that the solution has a decaying oscillation in the $\|H\|_2$ which is shown on the phase plot as an inwards spiral. Once the oscillation decays, we find that the solution is the same as that of the steady state. These solutions can be found where the Floquet analysis shown in figure 4.10 gives no unstable modes. Increasing δ does increase the wavelength at which the first unstable mode appears, however the wavelength does not increase sharply after $\delta = 2.5$, as figure 4.10 suggests, but instead increases at much the same rate as before. The closer the parameters are to

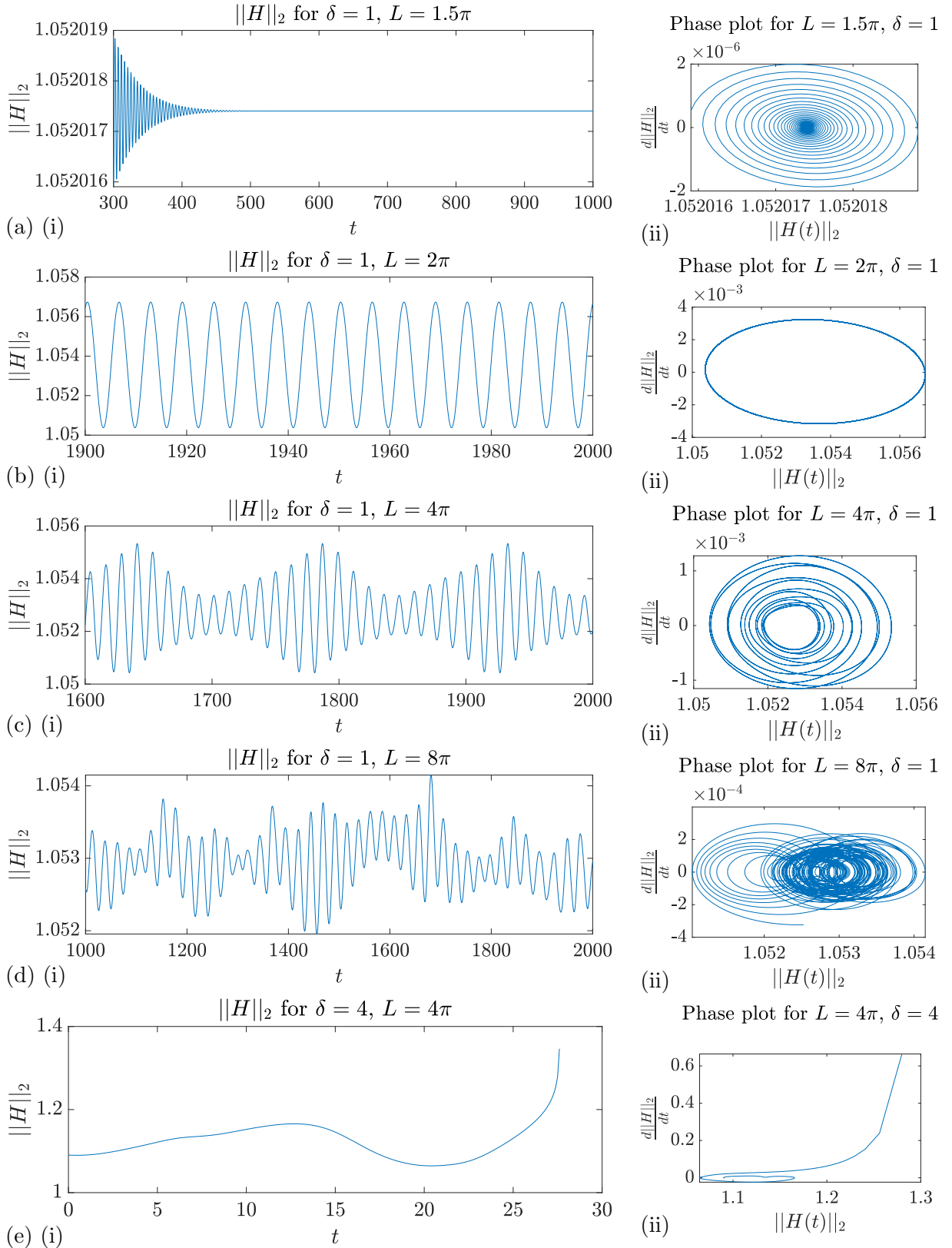


Figure 4.11: Plots used to classify the types of the solutions. (i) are plots of $\|H\|_2$ against time and (ii) are phase plots of $\|H\|_2$ against its time derivative. (a) shows a stable steady state. (b) shows a time periodic solution. (c) shows a quasi-periodic solution. (d) shows a non-periodic solution. (e) shows the case where the solution blows up.

the stability boundary, the slower the decay to the steady state.

Subfigure (b) shows a time periodic solution, which can be seen by the phase plot being a closed loop. In this case, we find that the time it takes to go between the peaks of $\|h\|_2$ is equal to the time it takes a wave to travel one period. These occur for parameters that roughly match those for one unstable mode in figure 4.10.

Figure 4.11(c) shows a quasi-periodic wave. The phase plot here is still a closed loop, however it now has a much more complicated path. While there is the usual oscillation in the $\|H\|_2$, from the fluid traversing a period, there is also a much slower secondary oscillation. In this case, we have the faster oscillation with a time period of 12.2 time units. The slower oscillation takes 146 time units.

Subfigure (d) shows a non-periodic solution, as there seems to be no coherent structure in either plot. Subfigure (e) shows a case where the solution blows up, as here the wave undergoes sharp steepening which causes the solver to no longer conserve mass. Similar behaviour is experienced when modelling the Benney equation (1.2) for large Reynold's numbers (Craster and Matar, 2009). Here the blow up occurs for large δ , typically with longer wavelengths. If we increase δ then blow up will occur at shorter wavelengths. This probably occurs due to the large nonlinearity, of h^3 and h^6 terms. Here we have the fluid creating a peak which just keeps growing.

4.5.2 Time periodic waves

Here we wish to look at how time periodic plots evolve over one period. For this, we will look at walls with different amplitudes and wavelengths. Figure 4.12 shows how the fluid thickness evolves over a period. In all these figures, the grey lines show the fluid thickness plotted every 0.1 time units. These show the path of the thickest part and thinnest part of the fluid. Interestingly, for all of these cases, the paths follow the shape of the steady state fluid thickness. Taking the mean of the fluid thickness over this period results in the steady state fluid thickness.

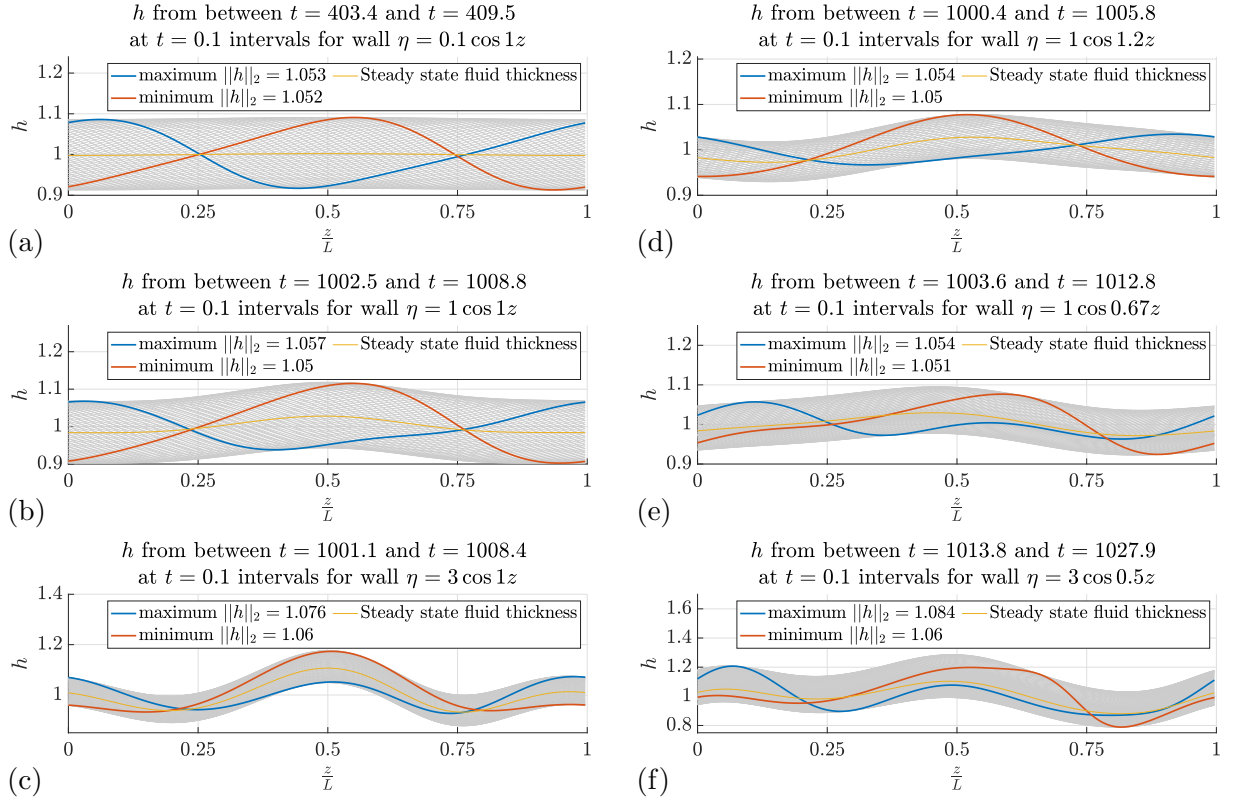


Figure 4.12: Fluid thickness for different shaped walls over a period for time periodic waves. (a)-(c) have a wavelength of 2π (d) has 1.73π (e) has 3π and (f) has 4π . (a) has amplitude 0.1, (b), (d) and (e) have amplitude 1 and (c) and (f) have amplitude 3. The grey lines show the fluid thickness every 0.1 time units. The fluid thicknesses with the maximum and minimum $\|H\|$ are shown, as well as the steady state fluid thickness.

Looking at subfigures (a), (b) and (c) we can compare the results for a wavelength of 2π . Here (a) has amplitude 0.1, (b) has amplitude 1 and (c) has amplitude 3. We see that increasing the amplitude the band around the steady state decreases in size. Increasing the amplitude also slows down the wave, with the time taken to traverse a period taking $t = 6.1$, 6.3 and 7.3 time units for $\delta = 0.1$, 1 and 3 respectively. Subfigures (b), (d) and (e) all have amplitude 1 and so can be used to compare the different wavelengths. (d) has wavelength 1.73π and is close to the steady state boundary, (b) has wavelength $L = 2\pi$ and (e) has wavelength 3π . Increasing the wavelength seems to introduce smaller secondary waves in the fluid thickness. Here, the band around the steady state is largest for the $L = 2\pi$ case. The waves travel at speeds 1.009 , 1.007 and 1.0210 for $L = 1.73\pi, 2\pi, 3\pi$. (f) shows the case where $\delta = 3$ and $L = 4\pi$. This case is still time periodic, however, for $\delta = 1$ we have a quasi-periodic solution. With both the $\delta = 3\pi$ cases, we see that the

wave travels with 2 peaks, one around the wall maximum and the other around the wall minimum. This still matches the shape of the steady state. For the $L = 4\pi$ case we see that the wave shows the nonlinearity with it having a fairly flat maximum in the minimum $\|H\|_2$. The wave speed for (c) is 0.865, where the wave speed for (f) is 0.889, suggesting there isn't a clear relationship between wave speed and wavelength.

Figure 4.13 shows the fluid thickness in a frame of reference that moves at the mean speed of the wave c . Here we can further see the difference between time periodic, quasi-periodic and non-periodic waves. In these figures, the maximum fluid thickness is yellow,

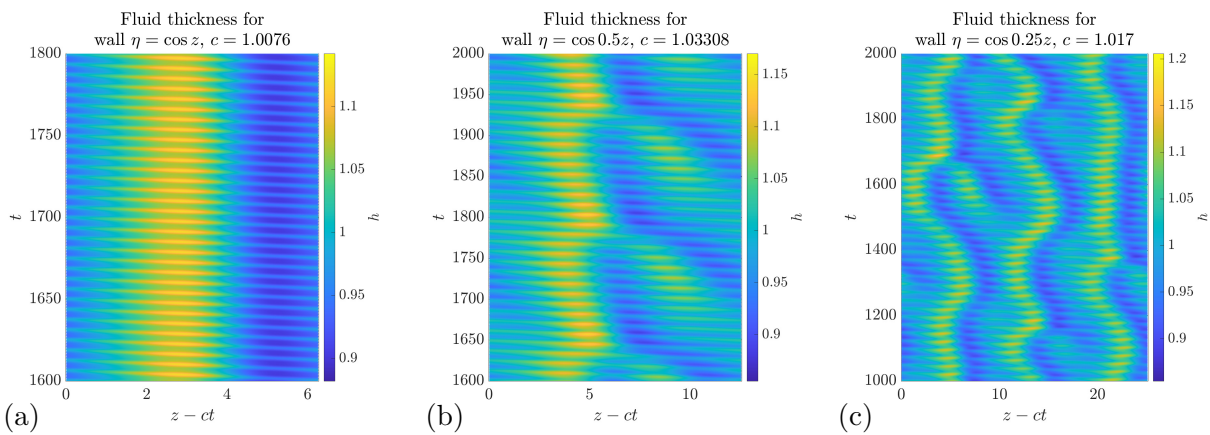


Figure 4.13: Colour plots that show the fluid thickness moving in a frame that travels at the mean wave speed. (a) shows a time periodic wave, (b) shows a quasi periodic wave and (c) shows a chaotic wave.

and the minimum thickness is the deepest blue. The maximum thickness oscillates in size over a period, as can be seen by the changing intensity of yellow. In these cases, one ripple is equivalent to the fluid travelling a period. Figure (a) shows the time periodic wave which can be seen by the maximum peak not oscillating in space. Figure (b) is a quasiperiodic wave as we can see the maximum peak oscillates in space, with the wave travelling at a slower speed than the mean for around 130 time units and then speeding up for 20 time units. Figure (c) has 3 peaks that seem to travel around the mean speed, slowing down and speeding up with no regularity.

4.6 Conclusions

In this chapter, we have looked at gravity driven thin flow down a cylinder with topography. We have derived an evolution equation for the film thickness, which incorporates inertial and capillary forces. The difference between this equation and that of chapter 3 is that here the Bond number is $O(\epsilon^2)$. From this equation, we have looked at the steady states that arise. Like in chapter 3 $L = 2\pi R$ is an important wavelength for determining the shape of the steady states. However, in this case the key wavelength is slightly less than $2\pi R$ as it is shifted left by the effects of inertia. Similar to the findings of chapter 3, the amplitude of the fluid disturbance is again generally larger for wavelengths of $L < 2\pi$ than those with $L > 2\pi$. The phase shift here however decreases from $\theta = \frac{3\pi}{2}$ to π as L increases to $2\pi R$, where in chapter 3, the phase shift increases from π to $\frac{3\pi}{2}$. Similarly, for $L > 2\pi$ the phase shift decreases from π , before increasing and tending to π as the wavelength increases. In chapter 3 the phase shift increased from $\frac{\pi}{2}$ before decreasing and tending back towards $\frac{\pi}{2}$. This is due to the extra wall term in equation (4.29) compared to equation (3.13).

Additionally, we have two extra parameters Re, ϵ to vary here. We looked at the effect of changing the wall amplitude, Reynolds number, Bond number and radius had on the steady states. Here we found that the Reynolds number didn't have much of an effect. Focusing on changing the wall wavelength and amplitude, we performed Floquet analysis to determine the stability of the steady states. For the smooth cylinder case, we found that the neutral stability curve was at $k = \sqrt{\frac{1}{R^2} + \frac{2}{5} \text{Bo} \text{ Re}}$, where increasing the amplitude helps stabilise the steady state. Here the inertia plays a key role in stabilising the fluid, and without it the neutral stability curve is at $L = 2\pi R$ as in chapter 3.

We then looked into numerically integrating the equation. Here again we found that the Floquet analysis provided a good prediction for the type of solution that occurs. We found that the stable cases settled into the steady states. Our solutions settled into time periodic, quasi-periodic and chaotic waves as more unstable modes appeared. In the large amplitude case, we found the numerical solution blows up. Taking a time average of the

numerical solutions, we again found that they approximated the steady state.

Chapter 5

Deposition

5.1 Introduction

Deposition is an important geological process shaping the world around us. Stalactites grow as a result of calcite being deposited on the surface from a supersaturated liquid film. The precipitation of calcite from this film is studied by Plummer et al. (1978); Buhmann and Dreybrodt (1985); Kaufmann and Dreybrodt (2007). Short et al. (2005b,a) made use of the deposition to model the shape of stalactites.

In this chapter, we will look into how crenulations on the surface of stalactites form. Previous works looking into the growth of crenulations include Camporeale and Ridolfi (2012); Vesipa et al. (2015); Camporeale (2017), however in these works they approximate the fluid to be flowing down an inclined plane, instead of down a cylinder, which better approximates the shape of stalactites. Here we will look to rectify this by using flow down cylinders, as derived in chapters 3 and 4.

5.2 Underlying Chemistry

5.2.1 Chemical reactions

In this chapter we will be looking at the chemicals listed in table 5.1.

| Symbol | Name |
|---------------------------|------------------------------|
| Ca^{2+} | calcium |
| CaCO_3 | calcium carbonate or calcite |
| CO_2 | carbon dioxide |
| CO_3^{2-} | carbonate |
| H^+ | hydrogen |
| HCO_3^- | bicarbonate |
| H_2CO_3^0 | carbonic acid |
| H_2O | water |
| OH^- | hydroxide |

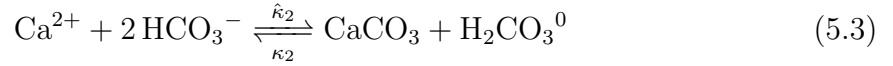
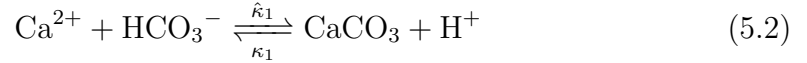
Table 5.1: Names of chemicals and their symbols.

Stalactites grow when the calcite, which is supersaturated in the fluid, is deposited onto the surface as carbon dioxide is degassed due to lower carbon dioxide pressure in the cave's air. The stoichiometry of the reaction is given by



which tells us that one calcium ion and two bicarbonate ions react to become calcium carbonate, carbon dioxide and water (Kaufmann and Dreybrodt, 2007). Note that this reaction is reversible, and the other direction occurs when the calcite is dissolved by the rain water initially. Calcite is produced as a result of several reactions which occur

simultaneously (Plummer et al., 1978), these are



where κ_i are the rate constants for the dissolution reactions and $\hat{\kappa}_i$ are the rate constants for the precipitation reactions. The neutrally charged carbonic acid, from equation (5.3), will quickly reach an equilibrium by dissociating into hydrogen and bicarbonate ions.



where K_5 is the equilibrium constant. In this section rate constants will be lowercase, and equilibrium constants, for instantaneous reactions, will be upper case.

From these equations Plummer et al. (1978) formulated what is known as the PWP equation for calcite dissolution

$$\tilde{F} = \kappa_1(\text{H}^+) + \kappa_2(\text{H}_2\text{CO}_3^*) + \kappa_3 - \kappa_4(\text{Ca}^{2+})(\text{HCO}_3^-) \quad (5.6)$$

where \tilde{F} is the rate of calcite dissolution in mol/(cm²s). The round brackets denote the activities of the chemicals. The activities are related to the concentration through an ion activity coefficient γ_i , where chemical X_i has activity $(X_i) = \gamma_i[X_i]$, with square brackets denoting the concentration. κ_4 is derived from the backwards rate constants of (5.2)-(5.4).

$$\kappa_4 = \hat{\kappa}_1 + \hat{\kappa}_2(\text{HCO}_3^-) + \hat{\kappa}_3(\text{OH}^-) \quad (5.7)$$

The rate constants depend on the temperature of the reaction and can be found in table 5.2.

As mineral surfaces slightly inhibit precipitation onto them, Dreybrodt (1999) modified

the PWP equation to be used for precipitation. They found that the rate of precipitation was

$$\tilde{F} = \kappa_1(\text{H}^+) + \kappa_2(\text{H}_2\text{CO}_3^*) + \kappa_3 - f\kappa_4(\text{Ca}^{2+})(\text{HCO}_3^-), \quad (5.8)$$

where experiments found f to be a factor of about 0.8. As we are now looking at precipitation we expect F in this case to be negative.

Precipitation occurs when there is a low carbon dioxide pressure, in waters with a pH=8-10 (Dreybrodt, 2012). These conditions mean that (5.4) is the dominant reaction, with the effects of (5.2) and (5.3) being small. We can therefore approximate the modified PWP equation (5.8) as

$$\tilde{F} = \kappa_3 - f\hat{\kappa}_3(\text{OH}^-)(\text{Ca}^{2+})(\text{HCO}_3^-). \quad (5.9)$$

Vesipa et al. (2015) reduces the PWP equation (5.6) further by making use of the electro-neutrality condition

$$2[\text{Ca}^{2+}] + [\text{H}^+] = [\text{HCO}_3^-] + 2[\text{CO}_3^{2-}] + [\text{OH}^-]. \quad (5.10)$$

There they note in typical karst waters that only the calcium and bicarbonate concentrations are significant, so $2[\text{Ca}^{2+}] = [\text{HCO}_3^-]$.

This gives them a calcite flux of

$$\tilde{F} = \varrho_0 + \varrho_1[\text{Ca}^{2+}] + \varrho_2[\text{CO}_2] + \varrho_3[\text{Ca}^{2+}]^2 \quad (5.11)$$

for some constants ϱ_i . This calcite flux modifies the wall of the stalactite through the relation

$$\tilde{R}_t + \tilde{\eta}_t = -\rho_c \tilde{F}, \quad (5.12)$$

where ρ_c is the molar volume of calcite (Vesipa et al., 2015). We have a negative sign

here, as \tilde{F} is the rate of change of calcium ions in solution. As the calcium is reacting to make calcite $\tilde{F} < 0$ and therefore the wall is growing. The growth of the wall here is split into the growth of the radius and the growth of the wall perturbation, where the mean calcite flux increases the radius, and the difference from the mean gives the growth of the crenulations. In Vesipa et al. (2015) the mean flux was set to 0 as there it is related to a slow translation of the wall, which has no effect on the fluid dynamics. Here however, as the mean flux causes the radius to grow, this will in turn affect the mean fluid thickness as well as the shape of the fluid disturbance.

5.2.2 Chemical transport

The precipitation of calcite is driven by the carbon dioxide pressure in the atmosphere. The transport of the chemicals is described by the convection-diffusion-reaction equations (Dreybrodt, 2012; Buhmann and Dreybrodt, 1985). We use these to describe the transport of calcium and carbon dioxide within the fluid layer.

$$\frac{\partial \tilde{c}_i}{\partial t} + \tilde{\mathbf{u}} \cdot \tilde{\nabla} \tilde{c}_i = D_i \tilde{\nabla}^2 \tilde{c}_i + \tilde{q}_i, \quad (5.13)$$

where \tilde{c}_i denotes the concentration, with the subscripts $i = 1, 2$ referring to calcium and carbon dioxide respectively. Here $\tilde{\mathbf{u}}$ is the velocity of the fluid, D_i denotes the diffusion coefficients and \tilde{q}_i is the reaction rate.

We also have boundary conditions, which are based on Fick's first law of diffusion (Fick, 1855). This tells us that the flux of calcium at the wall is F , which can be calculated from the PWP equation (5.8). We have no calcium ions leaving the fluid, and therefore the flux at the fluid-air interface is 0. For every mole of calcium deposited, we must also have a mole of carbon dioxide outgassed. The number of moles can be calculated by multiplying the flux by the surface area of the boundary that is crossed. As we are on a cylinder, the surface area of the fluid-air interface is larger than the surface area of the stalactite.

Overall we find

$$(\tilde{R} + \tilde{\eta})\tilde{F} = -(\tilde{R} + \tilde{\eta} + \tilde{h})\tilde{F}_{\text{CO}_2} \quad (5.14)$$

We also have no flux of carbon dioxide at the wall. Finally, the carbon dioxide at the fluid-air interface must be proportional to that of the atmospheric carbon dioxide. This is known as Henry's law. These boundary conditions are written as

$$-D_1 \frac{\partial \tilde{c}_1}{\partial \tilde{r}} \Big|_{\tilde{R}+\tilde{\eta}} = \tilde{F} \quad (5.15)$$

$$-D_2 \frac{\partial \tilde{c}_2}{\partial \tilde{r}} \Big|_{\tilde{R}+\tilde{\eta}} = 0 \quad (5.16)$$

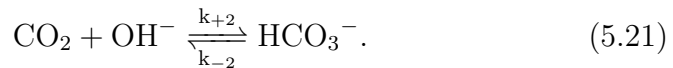
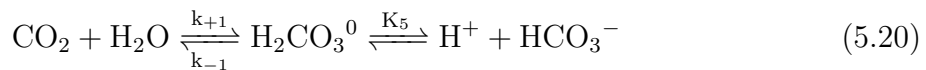
$$-D_1 \frac{\partial \tilde{c}_1}{\partial \tilde{r}} \Big|_{\tilde{S}} = 0 \quad (5.17)$$

$$-D_2 \frac{\partial \tilde{c}_2}{\partial \tilde{r}} \Big|_{\tilde{S}} = \tilde{F}_{\text{CO}_2} \quad (5.18)$$

$$\tilde{c}_2(\tilde{S}) = \mathcal{H}[\text{CO}_2]_{\text{atm}} \quad (5.19)$$

where \mathcal{H} is Henry's constant and $[\text{CO}_2]_{\text{atm}}$ is the atmospheric concentration of carbon dioxide. As there are five boundary conditions for two second order differential equations, the flux of carbon dioxide across the fluid air interface can be used to calculate the calcite flux. The wall evolution equation (5.12) comes about as the wall must grow at a speed proportional to the rate at which calcite is deposited.

For this problem, the conversion of carbon dioxide to bicarbonate is the rate limiting process (Kaufmann and Dreybrodt, 2007). Here the key reactions are



The second part of (5.20) is an instantaneous reaction, so here K_5 denotes the equilibrium constant (Dreybrodt, 2012). The other chemical reactions of the system (5.2)-(5.4) can be assumed to be in equilibrium, as they occur much faster than the reactions (5.20)-(5.21)

(Buhmann and Dreybrodt, 1985). Therefore, the reaction rate for calcium is

$$\tilde{q}_1 = 0 \quad (5.22)$$

and the reaction rate for carbon dioxide is

$$\tilde{q}_2 = k_-[\text{HCO}_3^-] - k_+\tilde{c}_2 \quad (5.23)$$

where the rate constants are defined by

$$k_- = k_a[\text{H}^+] + k_{-2} \quad (5.24)$$

$$k_+ = k_{+1} + k_{+2}[\text{OH}^-] \quad (5.25)$$

and here $k_a = \gamma_{\text{H}^+}\gamma_{\text{HCO}_3^-}\frac{k_{-1}}{K_5}$. These rate constants are derived from laboratory experiments and have been listed in table 5.2.

| Parameter | Value | Unit of Constant |
|-------------------------|---|------------------------------------|
| $\log_{10} k_{+1}$ | $330 - 111 \log_{10} T - 17300/T$ | s^{-1} |
| $\log_{10} k_{-1}$ | $13.6 - 3620/T$ | s^{-1} |
| $\log_{10} k_{+2}$ | $13.6 - 2900/T$ | $\text{l}(\text{mol s})^{-1}$ |
| $\log_{10} k_{-2}$ | $14.0 - 5310/T$ | s^{-1} |
| $\log_{10} K_2$ | $5150/T - 564000T^{-2} - 0.0325T + 38.9 \log_{10} T - 108$ | mol l^{-1} |
| $\log_{10} K_W$ | $22.8 - 4790/T - 0.0104T - 7.13 \log_{10} T$ | $\text{mol}^2 \text{l}^{-2}$ |
| $\log_{10} \mathcal{H}$ | $108 - 6920/T + 0.0199T - 40.5 \log_{10}(T) + 669000T^{-2}$ | $\text{mol}/(\text{l atm})$ |
| K_5 | 1.71×10^{-4} | mol l^{-1} |
| $\log_{10} \kappa_1$ | $0.198 - 444/T$ | cm s^{-1} |
| $\log_{10} \kappa_2$ | $2.84 - 2180/T$ | cm s^{-1} |
| $\log_{10} \kappa_3$ | $-5.86 - 317/T$ | $\text{mmol cm}^{-2}\text{s}^{-1}$ |

Table 5.2: Rate and equilibrium constants. Here T is the temperature in Kelvin (Kaufmann and Dreybrodt, 2007; Buhmann and Dreybrodt, 1985).

Cave temperatures stay fairly constant, with daily and seasonal oscillations of outside temperature largely dampened (Smithson, 1991; Bourges et al., 2006). The temperature in Poole’s Cavern, Buxton, UK being $6 - 7^\circ\text{C}$ (Smithson, 1991), and the temperature in Orgnac’s cave ranging from $10 - 12^\circ\text{C}$ (Bourges et al., 2006). An appropriate temperature for the rate constants therefore would be 285K . Table 5.3 shows the values of the rate constants at this temperature.

| Rate Constant | value |
|---------------|---|
| k_{+1} | $8.15 \times 10^{-3} \text{ s}^{-1}$ |
| k_{-1} | 7.36 s^{-1} |
| k_{+2} | $0.930 \text{ l}(\text{mol s})^{-1}$ |
| k_{-2} | $2.92 \times 10^{-5} \text{ s}^{-1}$ |
| k_a | $4.31 \times 10^3 \text{ l}(\text{mol s})^{-1}$ |
| K_2 | $3.43 \times 10^{-11} \text{ mol l}^{-1}$ |
| K_w | $3.48 \times 10^{-15} \text{ mol}^2 \text{ l}^{-2}$ |

Table 5.3: Rate constants for conversion of carbon dioxide to bicarbonate at 285 K .

For this problem we are losing carbon dioxide to the atmosphere, so in order for the overall reaction (5.1) to return to equilibrium, more carbon dioxide must be produced. This also creates calcium carbonate, which is precipitated. From equation (5.23) we can calculate the rate at which carbon dioxide is produced for different pH, partial pressure of carbon dioxide and calcium concentration. The pH tells us the concentration of hydrogen ions by the formula

$$\text{pH} = -\log_{10}([\text{H}^+]). \quad (5.26)$$

The carbon dioxide concentration can be approximated from the partial pressure using Henry’s law

$$[\text{CO}_2] = \mathcal{H}p_{\text{CO}_2}, \quad (5.27)$$

To find the bicarbonate concentration, we make use of the electro-neutrality condition (5.10). Here we also make use of the conversion of carbonate to bicarbonate, which as a

faster reaction than (5.20), (5.21) will be in equilibrium. The concentrations are related by

$$[\text{H}^+][\text{CO}_3^{2-}] = K_2[\text{HCO}_3^-] \quad (5.28)$$

with K_2 the equilibrium constant. We can also eliminate hydroxide ions by making use of the equilibrium constant of water $[\text{H}^+][\text{OH}^-] = K_w$. Using these equations we can write bicarbonate in terms of calcium and hydrogen ions

$$[\text{HCO}_3^-] = \frac{1}{[\text{H}^+] + 2K_2} (2[\text{Ca}^{2+}][\text{H}^+] + [\text{H}^+]^2 - K_w). \quad (5.29)$$

This expression is used by Short et al. (2005b) to find the reaction rate of carbon dioxide and hence the growth rate at different pH. Vesipa et al. (2015) further simplifies the expression for bicarbonate by considering the equilibrium constant for calcite

$$[\text{Ca}^{2+}][\text{CO}_3^{2-}] = K_C. \quad (5.30)$$

From this Vesipa et al. (2015) approximates the bicarbonate as

$$[\text{HCO}_3^-] = \alpha_1[\text{Ca}^{2+}] + \alpha_2 \quad (5.31)$$

for constants α_i . The water in caves is typically slightly alkaline, with pH 7-9 (Sasowsky and Dalton, 2005; White, 1976). Figure 5.1, shows the rate constants for the carbon dioxide produced as seen in equation (5.23). Here we see that for our typical cave temperature of 12°C, the rates are about 1.5 times smaller than at 20°C as used by Short et al. (2005b). We also see that at pH 8 $k_+ = 1 \times 10^{-2}$ is much larger than $k_- = 2 \times 10^{-4}$. This means we need to have significantly more bicarbonate, and therefore also more calcium, than carbon dioxide in order for the reaction to produce carbon dioxide.

Partial pressures of carbon dioxide in soils, which influences the partial pressure in the cave water, vary seasonally. Typical values of the partial pressure are between $10^{-3} - 10^{-1}$ atm, with the higher values occurring in tropical regions during the summer (Fairchild

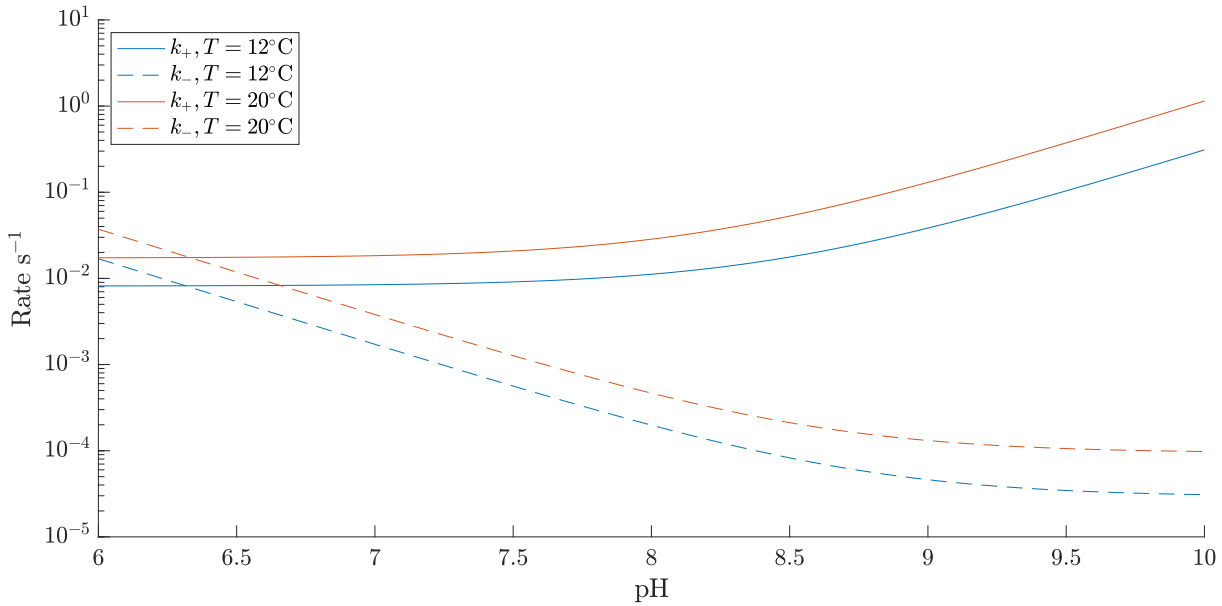


Figure 5.1: Values for the rates k_+ and k_- for different pH, at temperatures of 12°C and 20°C .

et al., 2012). The carbon dioxide pressure in caves is similar to that of the atmosphere at around 5×10^{-4} atm, however in poorly ventilated caves this can reach up to 6% atm (Ford and Williams, 2013). In order for calcite to be deposited, we require the soil partial pressure to be bigger than that of the cave. Calcium concentrations in cave waters were found to be 100-200 mg/L in caves in Grotte de Villars, France (Baker et al., 2000; Pitty, 1971). The atomic mass of calcium is 40g/mol, making the molar calcium concentration to be 2.5-5 mmol/L. This is within the range that Buhmann and Dreybrodt (1985) used experimentally.

Figure 5.2 shows the rate at which CO_2 is produced as a function of the partial pressure. Here we have used $\text{pH} = 8$, and a temperature of 12°C , with calcium concentrations of 2 and 5 mol/m³. We can see that by increasing p_{CO_2} , the rate at which CO_2 is produced decreases. For large enough partial pressures, the rate becomes negative, at which point the reaction is reversed and therefore calcium will be dissolved instead of precipitated. These higher partial pressures are what we may expect in soils, where we would expect the calcium to be dissolved. We also see that for smaller initial calcium concentrations, there is a smaller reaction rate. For smaller concentrations, we also start to dissolve more calcium at lower partial pressures. Initially, the water in the soil will have a much smaller

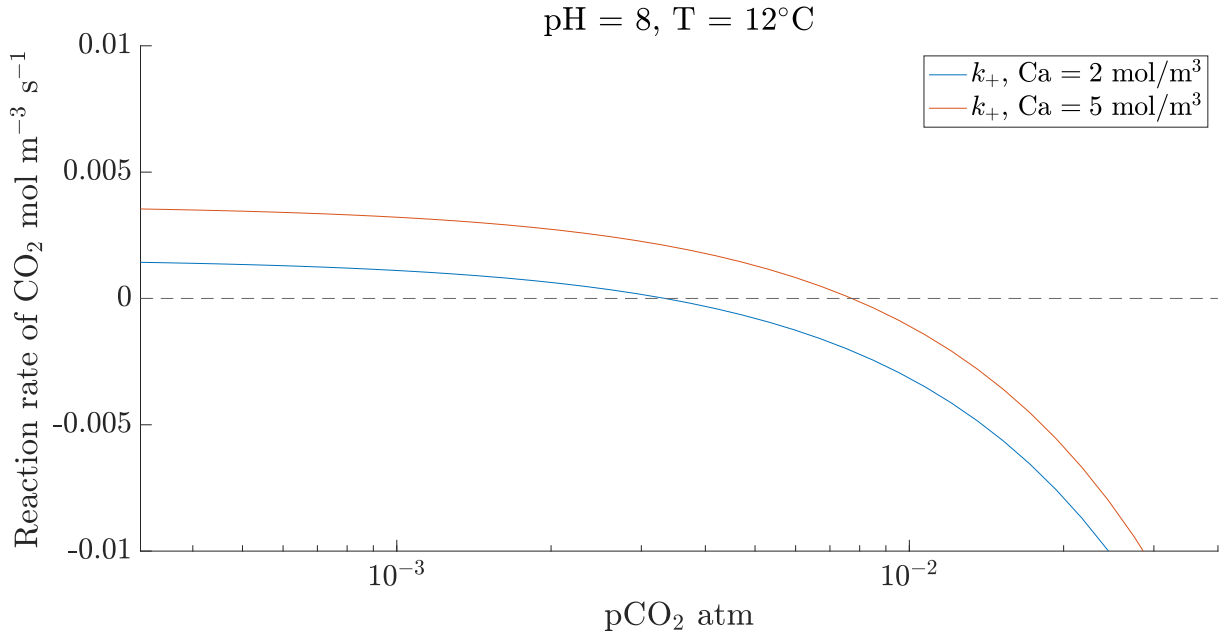


Figure 5.2: Rate at which carbon dioxide is produced dependent on the partial pressure of Carbon dioxide. The rate was calculated from equation (5.23), where the bicarbonate concentration is calculated using equation (5.29), at a temperature of 12°C and a pH of 8. This was done for initial calcium concentrations of 2 and 5 mol/m³.

calcium concentration. If it stays near the bedrock long enough to reach equilibrium, so that the reaction rate will be 0, then if the pH, temperature and calcium concentration are known, the p_{CO_2} of the soil can be calculated. For a cave atmosphere with $p_{\text{CO}_2} = 1 \times 10^{-3}$ atm, we have a reaction rate of the order 10^{-3} mol m⁻³ s⁻¹.

We will now scale equation (5.13) using the scaling derived in section 2.2.1. Here the nondimensional coordinates are

$$\tilde{r} = \tilde{h}_0 \left(\frac{R}{\epsilon} + \eta(z) + r \right) \quad (5.32)$$

$$\tilde{z} = \tilde{h}_0 \frac{z}{\epsilon}. \quad (5.33)$$

The velocities are scaled by $W = \frac{g\tilde{h}_0^2}{\nu}$ and the calcium concentration is scaled by the mean calcium concentration $\tilde{c}_1 = \mathcal{C}_1 c_1$. The carbon dioxide is scaled by the partial pressure $\tilde{c}_2 = \mathcal{C}_2 c_2$ where $\mathcal{C}_2 = \mathcal{H} p_{\text{CO}_2}$. The calcite flux is $\tilde{F} = \frac{\tilde{h}_0}{\tau \rho_c} F$, where τ is the time it takes to deposit a layer of calcite of thickness equivalent to that of the fluid. We also seek an equilibrium solution, so the partial time derivative will be zero (Short et al., 2005b).

Equation (5.13) becomes

$$\epsilon \text{Pe}_1 \left((u - \eta_z w) \frac{\partial c_1}{\partial r} + w \frac{\partial c_1}{\partial z} \right) = \left(\frac{\partial^2 c_1}{\partial r^2} + \frac{\epsilon}{R} \frac{\partial c_1}{\partial r} \right) + O(\epsilon^2) \quad (5.34)$$

$$\epsilon \text{Pe}_2 \left((u - \eta_z w) \frac{\partial c_2}{\partial r} + w \frac{\partial c_2}{\partial z} \right) = \left(\frac{\partial^2 c_2}{\partial r^2} + \frac{\epsilon}{R} \frac{\partial c_2}{\partial r} \right) + \kappa_c (\phi - c_2) + O(\epsilon^2) \quad (5.35)$$

where $\text{Pe}_i = \frac{\tilde{h}_0 W}{D_i} = \frac{\tilde{h}_0^3 g}{\nu D_i}$ is the Péclet number. $\kappa_c = \frac{k_+ \tilde{h}_0^2}{D_2}$ and $\phi = \frac{k_- [\text{HCO}_3^-]}{k_+ c_2}$. The boundary conditions (5.15)-(5.19) become

$$\xi_1 \frac{\partial c_1}{\partial r} \Big|_0 = -F \quad (5.36)$$

$$\frac{\partial c_2}{\partial r} \Big|_0 = 0 \quad (5.37)$$

$$\frac{\partial c_1}{\partial r} \Big|_h = 0 \quad (5.38)$$

$$\xi_2 \frac{\partial c_2}{\partial r} \Big|_h = - \left(1 - \frac{\epsilon h}{R} \right) F \quad (5.39)$$

$$c_2(h) = 1 \quad (5.40)$$

where $\xi_i = \frac{D_i c_i \tau \rho_c}{\tilde{h}_0^2}$. Finally we also have the growth rate of the stalactite from equation (5.12)

$$\frac{R_t}{\epsilon} + \eta_t = F. \quad (5.41)$$

For $\text{pH} = 8$, $T = 12^\circ\text{C}$, the bicarbonate concentration is approximately twice the calcium concentration, so we consider $\phi = \alpha c_1$ with $\alpha = \frac{2k_- c_1}{k_+ c_2}$. For a partial pressure of carbon dioxide $p_{\text{CO}_2} = 10^{-3}$ atm and calcium concentration $[\text{Ca}] = 2 \text{ mol m}^{-3}$ we find that $\text{mean}(\phi) \sim 3c_2$, meaning that carbon dioxide is being produced by this reaction. Here, the diffusion coefficient for calcium at 12°C is $0.9 \times 10^{-9} \text{ m}^2/\text{s}$. At this temperature, the diffusion coefficient for carbon dioxide is $1.3 \times 10^{-9} \text{ m}^2/\text{s}$ (Buhmann and Dreybrodt, 1985).

For a fluid thickness of 10^{-5} m we find that the Péclet number $\text{Pe}_2 = 7.5$ and $\kappa_c = 7.7 \times 10^{-4}$, which means $\kappa_c = O(\epsilon)$. $\xi_1 = 1.8 \times 10^4$ so $\xi_1 = O(\epsilon^{-1})$ and $\xi_2 = 440$.

With a film of this size we are in regime 1 according to Dreybrodt (2012). In this regime, diffusion is fast across the film layer and so all chemicals are effectively constant in the radial direction. The carbon dioxide production is the rate limiting step, and the precipitation rates are proportional to the fluid thickness.

Increasing the fluid thickness slightly to 5×10^{-5} m, we are in regime 2 of Dreybrodt (2012). The lower boundary for the thickness may be slightly less than 5×10^{-5} m to be in regime 2 here, as we are using a lower temperature. In regime 2, the precipitation rate depends on both the diffusion and the carbon dioxide production. We can see this from the reaction diffusion equation as now $Pe_2 = 4 \times 10^3 = O(\epsilon^{-1})$ and $\kappa_c = 0.02 = O(1)$. $\xi_1 = 720$ and $\xi_2 = 18$.

Note while the temperature, pH, calcium concentration and pressure of carbon dioxide can also affect the growth rate, we will primarily focus on the effects of the radius \tilde{R} and the flow rate Q . From these parameter the mean fluid thickness can be calculated using equation (2.4). Unless specified, we will use pH = 8, T = 12°C, [Ca] = 5 mol m⁻³ and $p_{CO_2}=10^{-3}$ atm in the rest of this chapter.

5.3 Linear Stability Analysis

In order to see under what conditions crenulations form, we start by considering a perfectly smooth cylinder. From this, we consider a small perturbation from the wall. If this perturbation grows in time, then this tells us that crenulations should form. The perturbation with the fastest growing wavelength tells us the wavelength that we would expect the crenulations to have. For the hydrodynamics, we will be using the equations of chapter 4. By also including the Reynolds number and ϵ , we better capture the effect of the flow rate on the fluid thickness.

In the smooth cylinder case, there is no z dependence. As seen in chapter 4, the smooth cylinder fluid thickness is $h_0 = 1$. We can calculate the velocities from (4.10),

(4.12), (4.17), (4.19), resulting in

$$w_0 = r - \frac{r^2}{2} + \frac{\epsilon}{6R} (r^3 - 3r^2 + 3r) \quad (5.42)$$

$$u_0 = 0. \quad (5.43)$$

Here we still have a base calcium c_{10} and carbon dioxide c_{20} concentration in the water. This will lead to a base calcite flux F_0 . Adding a perturbation to the wall of amplitude $\delta \ll 1$ results in a disturbance to the fluid thickness of the same order. We will also consider that the velocities, carbon dioxide and calcium and therefore also the calcite flux to be perturbed similarly. Now the variables can be written as

$$\eta = \delta e^{ikz - \omega t} \quad (5.44)$$

$$h = 1 + \delta h_1 e^{ikz - \omega t} \quad (5.45)$$

$$w = w_0(r) + \delta w_1(r) e^{ikz - \omega t} \quad (5.46)$$

$$u = \delta u_1(r) e^{ikz - \omega t} \quad (5.47)$$

$$c_1 = c_{10}(r) + \delta c_{11}(r) e^{ikz - \omega t} \quad (5.48)$$

$$c_2 = c_{20}(r) + \delta c_{21}(r) e^{ikz - \omega t} \quad (5.49)$$

$$F = F_0 + \delta F_1 e^{ikz - \omega t}. \quad (5.50)$$

For the bicarbonate we will use the approximation from equation (5.31). Looking at equation (5.34) at leading order in δ , we find

$$\frac{\partial^2 c_{10}}{\partial r^2} + \frac{\epsilon}{R} \frac{\partial c_{10}}{\partial r} = 0. \quad (5.51)$$

The boundary conditions (5.36), (5.38) give

$$\xi_1 c'_{10}(0) = -F \quad (5.52)$$

$$c'_{10}(1) = 0. \quad (5.53)$$

The flux at the fluid-air interface (5.53) gives us that the leading order calcium is a constant. As we scaled the calcium using its mean, this tells us that $c_{10} = 1$. This however would result in the flux at the wall from equation (5.52) also being 0, suggesting this flux is driven by smaller terms.

From equation (5.35) we find the leading order equation for the concentration of carbon dioxide to be

$$\frac{\partial^2 c_{20}}{\partial r^2} + \frac{\epsilon}{R} \frac{\partial c_{20}}{\partial r} + \kappa_c(\alpha - c_{20}) = 0 \quad (5.54)$$

where $\alpha = \alpha_1 + \alpha_2$. The boundary conditions (5.37), (5.40) at leading order are

$$c'_{20}(0) = 0 \quad (5.55)$$

$$c_{20}(1) = 1. \quad (5.56)$$

The carbon dioxide flux at the fluid-air interface (5.39) can be used to find the leading order calcite flux

$$F_0 = -\frac{R}{R - \epsilon} \xi_2 \frac{\partial c_{20}}{\partial r} \Big|_1. \quad (5.57)$$

Substituting this into equation (5.41), we find the growth rate of the radius

$$R_t = \epsilon F_0. \quad (5.58)$$

At $O(\delta)$, equation (5.34) gives

$$\frac{\partial^2 c_{11}}{\partial r^2} + \frac{\epsilon}{R} \frac{\partial c_{11}}{\partial r} = ik\epsilon \text{Pe}_1 w_0 c_{11}, \quad (5.59)$$

with boundary conditions (5.36), (5.38)

$$\xi_1 c'_{11}(0) = -F_1 \quad (5.60)$$

$$c'_{11}(1) = 0. \quad (5.61)$$

The $O(\delta)$ carbon dioxide can be found from equation (5.35).

$$\frac{\partial^2 c_{21}}{\partial r^2} + \frac{1}{R} \frac{\partial c_{21}}{\partial r} + \kappa_c(\alpha_1 c_{11} - c_{21}) = ik\epsilon \text{Pe}_2 \left((u_1 - w_0) \frac{\partial c_{20}}{\partial r} + w_0 c_{21} \right). \quad (5.62)$$

The boundary conditions are again found from equations (5.37), (5.40)

$$c'_{21}(0) = 0 \quad (5.63)$$

$$c_{21}(1) + h_1 c'_{20}(1) = 0 \quad (5.64)$$

The calcite flux perturbation is found from (5.39)

$$F_1 = -\frac{R}{R - \epsilon} \left(\xi_2 (c'_{21}(1) + h_1 c''_{20}(1)) - \frac{\epsilon h_1 F_0}{R} \right). \quad (5.65)$$

Substituting into equation (5.41), we get the growth rate of the crenulations

$$\omega = -F_1 \quad (5.66)$$

We solve equations (5.54)-(5.66) numerically using methods described in section 2.5. Here we discretise r into 100 spatial points and use a second order finite difference for the derivatives. We then use the MATLAB function `fsolve` to solve the system of equations.

Overall we want to calculate the growth rate ω from equation (5.66). Writing $\omega = -\sigma + ikc$, where σ is the real part of ω and kc is the imaginary part, we find that the perturbation will grow if $\sigma > 0$. This perturbation has a wave speed of c , which will determine whether the crenulations should travel upstream ($c < 0$) or downstream $c > 0$. Another important quantity is the wavelength which achieves the largest growth rate. As

this disturbance grows faster than all the others, it tells us the wavelength which we would expect our crenulations to have.

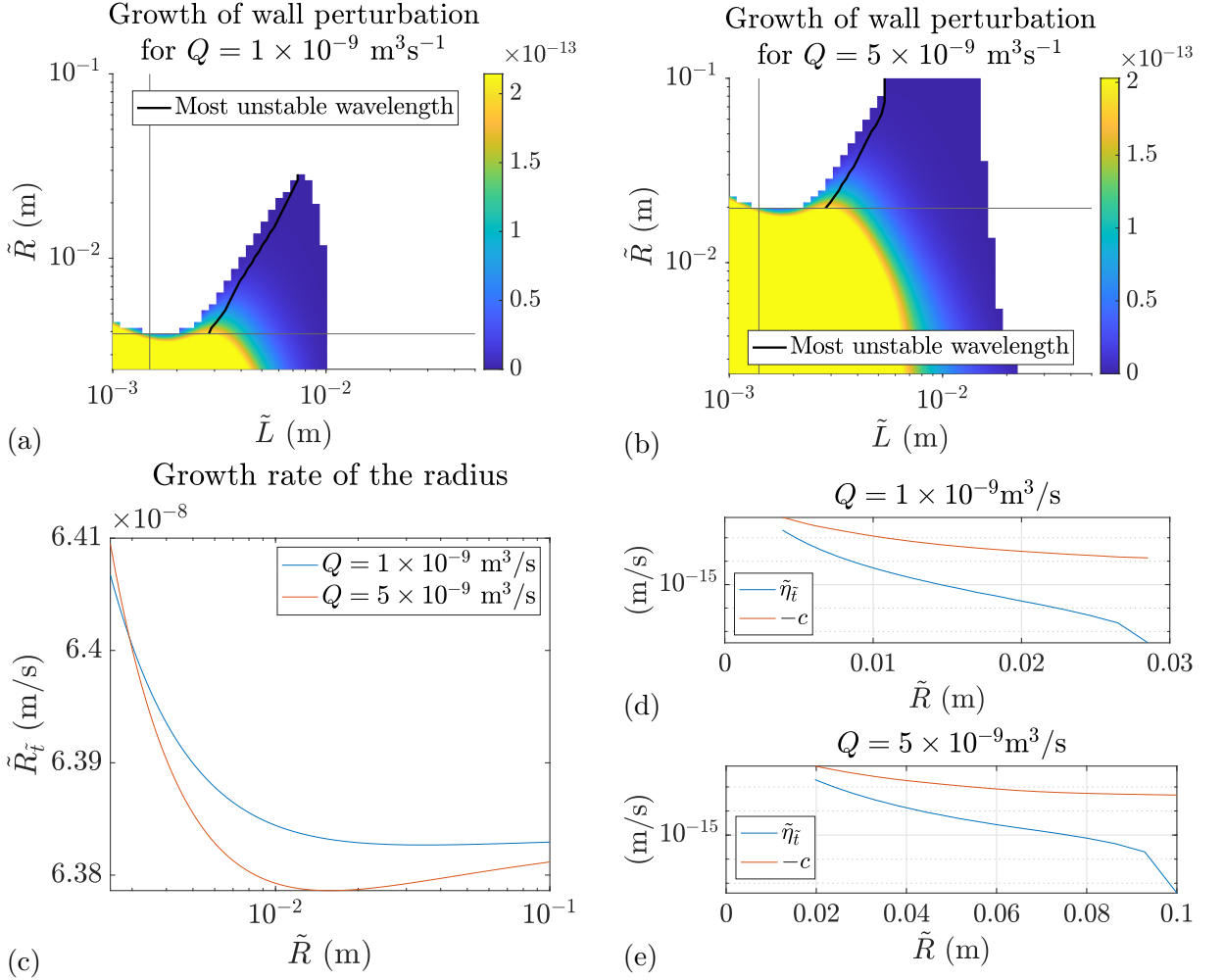


Figure 5.3: Growth of wall perturbation. (a) and (b) shows for which radius and wavelength that the wall perturbation grows, highlighting the most unstable wavelength for a given radius. (c) shows the speed at which the radius grows. (d) and (e) show the speed at which the perturbation grows and also the speed at which it travels. (a) and (d) have a flow rate of $10^{-9} \text{ m}^3/\text{s}$. (b) and (e) have a flow rate of $5 \times 10^{-9} \text{ m}^3/\text{s}$.

Figure 5.3 shows the growth of this wall perturbation for various radii and wavelengths. Plots (a) and (b) are coloured in where the wall perturbation should grow and are white where it does not. In both cases there is a region for smaller radii, where growth occurs, however the most unstable wavelength in this region is much smaller than 10^{-3} m . In the region where we expect growth, we find that the most unstable wavelength increases with the radius. Figure (a) has a flow rate of $Q = 1 \times 10^{-9} \text{ m}^3/\text{s}$. Here we expect crenulations to form for radii between 4 – 30 mm, however for radii larger than 30 mm we would

not expect to have crenulations. In this case, our most unstable wavelength ranges from 3 – 7 mm. Increasing the flow rate to $5 \times 10^{-9} \text{ m}^3/\text{s}$, as seen in (b), we now experience crenulations for radii of 2 – 10 cm. Here, the most unstable wavelength ranges from 3 – 5 mm. The regions where we see the most unstable wavelengths in (a) and (b) roughly correspond to similar fluid thicknesses.

Figure (c) shows the speed at which the radius grows for these flow rates. Here it can be seen that the radius grows at speeds of the order 10^{-12} m/s . This is similar to growth rates reported in Short et al. (2005b), as 1 cm/century is $3.1 \times 10^{-12} \text{ m/s}$. Increasing the radius decreases the speed at which it grows. As increasing the radius decreases the fluid thickness, we see that this agrees with the leading order findings of Short et al. (2005b) that thinner fluids result in slower growth. Figures (d) and (e) show the maximum growth rate ω and the corresponding speed c for increasing radii. In both cases we have $c < 0$ suggesting that the wall perturbations travel upstream. This agrees with observations and results from Camporeale (2017). In both cases, the speed is around $O(10^{-14} - 10^{-12}) \text{ m/s}$. The growth rate and the wave speed both decrease in magnitude for larger radii. These growth rates will also be multiplied by our small wall amplitude δ , showing that the growth of the wall perturbation is substantially slower than that of the radius.

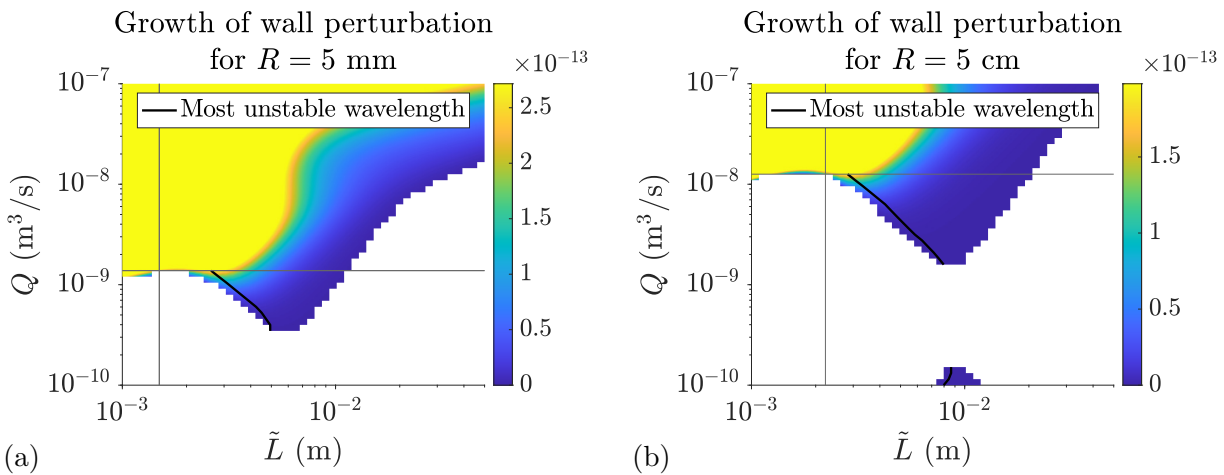


Figure 5.4: Growth of wall perturbation for different flow rates and wavelengths. (a) has a radius of 5 mm and (b) has a radius of 5 cm.

Figure 5.4 looks at how the growth rate changes with the flow rate Q . Here we see there is a region for larger Q where growth occurs, however the most unstable wavelength

is much smaller than we would expect. Subfigure (a) has a radius of 5 mm. Here we see the expected growth for Q between $3.5 \times 10^{-10} - 1.5 \times 10^{-9} \text{ m}^3/\text{s}$. The most unstable wavelength decreases from 5-3 mm. The growth rate of the most unstable mode increases with the flow rate up to $1.1 \times 10^{-8} \text{ m}^3/\text{s}$. In comparison, figure (b) has a radius of 5 cm. Now, the ideal region is between $Q = 1 \times 10^{-9} - 1 \times 10^{-8} \text{ m}^3/\text{s}$. Here, the most unstable wavelength decreases from 8-3 mm. There is also a small region with $Q = 1 \times 10^{-10} \text{ m}^3/\text{s}$ that has a wavelength of 8 mm. Again, the growth rate increases with Q . Here the fluid thickness increases as Q increases, but also increases as R decreases.

From figures 5.3 and 5.4 and equation (2.4), we effectively see that increasing the fluid thickness causes the most unstable wavelength to decrease. This is contradictory to results found in Vesipa et al. (2015); Camporeale (2017), where they find increasing the fluid thickness (by making use of the Reynolds number) should increase the wavelength. This could be the result of the different geometries of our models.

5.4 Wall Evolution Models

While the linear stability analysis will tell us under which conditions the crenulations form, it is also useful to know how the crenulations grow when their amplitude is no longer small compared to the fluid thickness. This is important for larger radii stalactites, where the crenulations should have already developed. In order to do this, we will attempt to model the wall evolution more fully.

5.4.1 Regime 1 - Thin fluid

In regime 1 looking at equations (5.34) and (5.35) to leading order we find

$$\frac{\partial^2 c_i}{\partial r^2} = 0 \tag{5.67}$$

for both calcium and carbon dioxide. The no flux conditions at the fluid-air (5.38) and fluid-solid interfaces (5.37) respectively mean that, the concentrations are just constants at leading order. These constants are set to 1 as these have been scaled by the mean concentrations \mathcal{C}_i . We expand the concentrations to first order in ϵ by setting

$$c_1 = 1 + \epsilon\chi \tag{5.68}$$

$$c_2 = 1 + \epsilon\psi \tag{5.69}$$

At $O(\epsilon)$ the calcium equation is

$$\chi_{rr} = 0 \tag{5.70}$$

with the fluid-air no flux condition (5.38), this means that the calcium is still constant. Again as this has been scaled by \mathcal{C}_1 , we can set this flux to be 0. At $O(\epsilon)$ the carbon dioxide equation is forced by the leading order calcium and carbon dioxide, with equation (5.35) becoming

$$\frac{\partial^2 \psi}{\partial r^2} + \kappa_c(\phi_0 - 1) = 0 \tag{5.71}$$

where ϕ_0 is a constant that depends on the leading order calcium. This can be calculated from equation (5.29). The boundary conditions here are $\psi_r(0) = 0$ and $\psi(h) = 0$. This results in

$$\psi = \kappa_c(1 - \phi_0) \left(\frac{r^2 - h^2}{2} \right). \tag{5.72}$$

The calcite flux can be found from looking at equation (5.39) at leading order, which results in

$$F = \xi_2 \kappa_c (\phi_0 - 1) h \tag{5.73}$$

This results in the wall evolution being

$$\eta_t = \gamma h \tag{5.74}$$

for a positive constant γ . This evolution equation was also used by Bertagni and Camporeale (2017); Ledda et al. (2021). The growth of the wall is very slow, with $\gamma \sim 10^{-7}$ (Bertagni and Camporeale, 2017). We therefore rescale our time $\tau = \gamma t$ so that we have

$$\eta_\tau = h \tag{5.75}$$

As the fluid has mean thickness 1 this suggests that the crenulations are always growing. Really the mean fluid thickness grows the radius of the stalactites. The crenulation growth is therefore the result of the difference from the mean fluid thickness. This means that our wall growth is

$$R_\tau = \epsilon \tag{5.76}$$

$$\eta_\tau = h - 1. \tag{5.77}$$

From chapters 3 and 4, we know that the fluid thickness depends on the wall shape. Due to the different timescales, we will use the wall at each time step to calculate the fluid thickness. As shown in chapters 3 and 4, the steady state fluid thicknesses are similar to the time averaged fluid thicknesses, and therefore we will use the steady state thicknesses to ease the computation.

If we are to maintain the same flow rate, the increasing radius would result in a thinning fluid thickness. This would in turn slow down the growth of the radius. However, we will for now ignore this effect by making sure we only integrate up to $\tau = \tau_T$ where $\tau_T \ll \frac{1}{\epsilon}$ so that the radial growth is small. From the linear stability analysis, we found the most unstable wavelength. While the wavelength may evolve with time, we would expect the wavelength to change at slower speeds similar to the radius.

Small amplitude sinusoidal crenulations

For the cases where we had a small amplitude wall of the form

$$\eta(z) = \delta \cos kz, \quad (5.78)$$

we showed in chapter 3 and 4 that the fluid thickness was of the form (3.17)-(3.19) and (4.53)-(4.55). This means that

$$h - 1 = B \cos(kz - \theta). \quad (5.79)$$

If we have the wall amplitude and phase shift changing in time, so

$$\eta(z, \tau) = A(\tau) \cos(kz - \varphi(\tau)). \quad (5.80)$$

If we let $\zeta = z - \frac{\varphi}{k}$, then from equations (3.17), (4.53), we expect the difference from the fluid thickness mean to take the form

$$h - 1 = B(\tau) \cos(k\zeta - \theta(\tau)). \quad (5.81)$$

Therefore from equation (5.77), we can find that the amplitude evolves like

$$A_\tau = B \cos \theta \quad (5.82)$$

and the phase shift evolves as

$$\varphi_\tau = \frac{B}{A} \sin \theta. \quad (5.83)$$

The crenulations will grow if $A_\tau > 0$ and shrink if $A_\tau < 0$. Noting that the amplitudes $A, B > 0$, this means that if the phase shift between the wall and the fluid disturbance is $\theta < \frac{\pi}{2}$ or $\theta > \frac{3\pi}{2}$ we would expect the crenulations to grow, and the crenulations should

shrink if $\frac{\pi}{2} < \theta < \frac{3\pi}{2}$. On the boundaries of these inequalities at $\theta = \frac{\pi}{2}, \frac{3\pi}{2}$, the amplitude of crenulations will remain constant. φ is the phase shift between the old and new wall. If $0 < \theta < \pi$ then $\varphi_\tau > 0$ and so, the crenulations move downstream. The crenulations move upstream for $\pi < \theta < 2\pi$. Here at $\theta = 0, \pi$, the crenulations will stay in the same position.

For the small amplitude steady states in chapter 3, we found from equations (3.17)-(3.19) that the phase shift between the crenulation and the fluid thickness had $\frac{\pi}{2} < \theta < \frac{3\pi}{2}$, which suggests for all cases that the crenulations should shrink. We also have $\theta > \pi$ for $L < 2\pi R$, suggesting that in these cases the crenulations move upstream. For $L > 2\pi R$ the crenulations would move downstream. The same is true for the fluid thickness in chapter 4 as can be seen in figure 4.4. While this suggests that crenulations would be smoothed out, the wall shape should introduce some z dependence in the concentrations and therefore the wall growth may be better suited to Regime 2.

5.4.2 Regime 2

As discussed in section 5.2.2, a film thickness of 5×10^{-5} m results in regime 2 of Dreybrodt (2012). The Péclet numbers in this case are large, roughly being $O(\epsilon^{-1})$. Therefore we set $\mathcal{P}_i = \epsilon \text{Pe}_i$ to more clearly see that the advection terms appear at leading order. In order to numerically integrate equations (5.34) and (5.35) it also helps to rectangularise the domain by letting

$$\tilde{r} = \tilde{h}_0 \left(\frac{R}{\epsilon} + \eta(z) + rh(z) \right) \quad (5.84)$$

so now the fluid lies in the region between 0 and 1. Now our derivatives are

$$\frac{\partial}{\partial \tilde{r}} = \frac{1}{\tilde{h}_0 h} \frac{\partial}{\partial r} \quad (5.85)$$

$$\frac{\partial}{\partial \tilde{z}} = \frac{\epsilon}{\tilde{h}_0} \left(\frac{\partial}{\partial z} - \frac{1}{h} (rh_z + \eta_z) \frac{\partial}{\partial r} \right). \quad (5.86)$$

From equations (5.34)-(5.35), we get the scaled diffusion reaction equations

$$\mathcal{P}_1 \left(\frac{(u - (\eta_z + rh_z)w)}{h} \frac{\partial c_1}{\partial r} + w \frac{\partial c_1}{\partial z} \right) = \frac{1}{h^2} \frac{\partial^2 c_1}{\partial r^2} \quad (5.87)$$

$$\mathcal{P}_2 \left(\frac{(u - (\eta_z + rh_z)w)}{h} \frac{\partial c_2}{\partial r} + w \frac{\partial c_2}{\partial z} \right) = \frac{1}{h^2} \frac{\partial^2 c_2}{\partial r^2} + \kappa_c(\phi(c_1) - c_2). \quad (5.88)$$

From the continuity equation (2.20) at leading order we find

$$u - (\eta_z + rh_z)w = - \int \frac{\partial}{\partial z} (hw) dr \quad (5.89)$$

giving an alternative expression for the first terms of equations (5.87)-(5.88). The boundary conditions are given by equations (5.15)-(5.19)

$$\xi_1 \frac{\partial c_1}{\partial r} \Big|_0 = -hF \quad (5.90)$$

$$\frac{\partial c_2}{\partial r} \Big|_0 = 0 \quad (5.91)$$

$$\frac{\partial c_1}{\partial r} \Big|_1 = 0 \quad (5.92)$$

$$\xi_2 \frac{\partial c_2}{\partial r} \Big|_1 = - \left(1 - \frac{\epsilon h}{R} \right) hF \quad (5.93)$$

$$c_2(1) = 1. \quad (5.94)$$

We attempted to solve equations (5.87) - (5.40) numerically using the methods described in section 2.5. To do this, z was split into 128 spatial steps, with the derivatives done using the pseudo spectral method. r was split into 65 spatial steps, with the derivatives done using second order central finite differences. The flux boundary conditions made use of forward and backwards finite differences. Then the MATLAB function `fsolve` was used to solve the system. In this scenario, no solution was found. A likely reason was the matching of the calcite flux at the wall (5.15) with the carbon dioxide flux at the air interface (5.18). The calcium flux may be driven by a boundary layer near the wall. Buhmann and Dreybrodt (1985) shows the concentration levels of the different species across the film. Their work shows that for fluids with thickness 0.05 cm the calcium

concentration across the fluid remains effectively constant, where the carbon dioxide is about 25% higher at the wall than at the air interface. Therefore, we will consider the calcium to be constant.

Now we solve the carbon dioxide concentration numerically using equation (5.88), with boundary conditions (5.91) and (5.94). The rate at which the wall will grow can then be calculated from the flux of carbon dioxide across the fluid air interface (5.93). The growth of the radius will be the calculated from the mean flux, and the growth of the perturbation will be the difference from the mean flux.

$$\tilde{F} = -\frac{\rho_c \mathcal{C}_2 D_2}{\tilde{h}_0 h} \frac{\partial c_2}{\partial r} \quad (5.95)$$

$$\tilde{R}_t = \tilde{F} \quad (5.96)$$

$$\tilde{\eta}_t = \tilde{F} - \bar{F} \quad (5.97)$$

where \bar{F} is the mean flux. Noting here, we have gone back to the dimensional variables to see the actual growth values. The growth rates were calculated numerically for walls of amplitude 1. From this, we found the wall growth to approximate a cosine. Therefore, if our wall is of the form

$$\tilde{\eta}(z, t) = A(t) \cos(kz - \varphi(t)) \quad (5.98)$$

and the growth is of the form

$$\tilde{\eta}_t = B(t) \cos(kz - \theta), \quad (5.99)$$

then our growth rate is

$$A_t = B \cos(\theta - \varphi) \quad (5.100)$$

and the phase shift evolves as

$$\varphi_t = \frac{B}{A} \sin(\theta - \varphi). \tag{5.101}$$

Physically the crenulations will grow if $A_t > 0$ and shrink if $A_t < 0$. $\varphi_t > 0$ means that the crenulations would migrate downstream and $\varphi_t < 0$ causes an upstream migration.

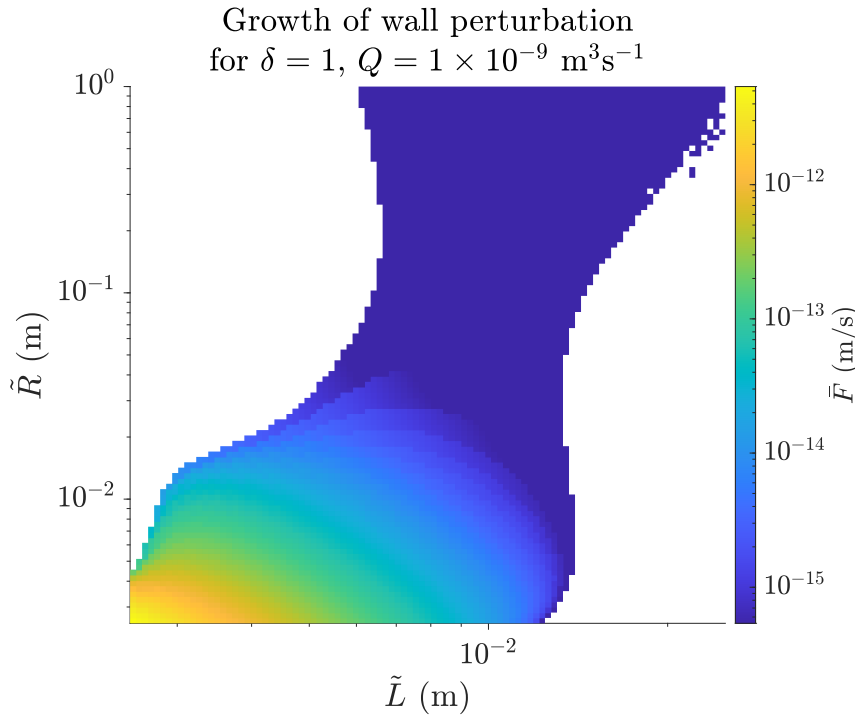


Figure 5.5: Radii and wavelengths for which growth occurs. Here we have a wall amplitude of $\delta = 1$ and a flow rate $Q = 1 \times 10^{-9} \text{ m}^3/\text{s}$.

Figure 5.5 shows the radii and the wavelengths for which we expect the crenulations to grow. Comparing this to the linear theory shown in figure 5.3(a) we see that the crenulations allows for growth to occur for both larger radii and shorter and longer wavelengths. The wavelengths that we expect vary between 3 mm and 2 cm. We see that for larger radii, growth occurs for longer wavelengths.

A potential stalactite from the linear theory, with flow rate of $1 \times 10^{-9} \text{ m}^3/\text{s}$ would be one that has a radius of 10 mm and a wavelength of 5 mm. Numerically solving the growth of stalactites given by equations (5.95)-(5.97) is done in stages. At each time step, a new radius and crenulation shape are found. These are then used to calculate the new

| | |
|---|---|
| Initial Radius | 1 cm |
| Crenulation wavelength | 5 mm |
| Initial Crenulation amplitude/fluid thickness | 0.1 |
| Flow rate | $1 \times 10^{-9} \text{ m}^3/\text{s}$ |
| Calcium concentration | $5 \text{ mol}/\text{m}^3$ |
| Pressure of carbon dioxide | $1 \times 10^{-3} \text{ atm}$ |
| Temperature | 12°C |
| pH | 8 |

Table 5.4: Modelled Stalactite Parameters

mean fluid thickness. This allows us to then calculate the nondimensional ϵ , L , Bo , Re and η , noting that here we scale the vertical length scale by \tilde{R} and so $R = 1$. Using these parameters, we then calculate the new steady state fluid thickness using equations (4.29) and (4.34). Using this fluid thickness, we can then calculate the carbon dioxide concentration using equations (5.88), (5.91) and (5.94). Which gives the new flux for equations (5.95)-(5.97). Again, we have used MATLAB function `ode15s` to perform the time-stepping.

From figure 5.5 we see that the wall growth is around 1×10^{-14} , which is approximately 0.1 mm/century. The radius is expected to grow by 10 mm/century. As the fluid thickness is around 0.01 mm thick, in a century the crenulation will grow ten times its size while the radius only doubles. As our model requires the wall to be of an amplitude similar to the fluid thickness, we will look to integrate the wall shape over a period of decades. We modelled the stalactite to initially have the parameters shown in table 5.4. Time was integrated in years and was stopped when the solver failed to find a steady state fluid thickness.

Figure 5.6 shows the growth of the radius for our stalactite. From (a) we see that in 60 years it has grown by 2 mm. (b) shows that the speed of the radial growth decreases with time. This is as expected, as increasing the radius decreases the fluid thickness, which slows down the growth. This is however very slight, as the radius does not grow by much in this time.

Figure 5.7 shows the growth of the crenulations for the modelled stalactite. From (a)

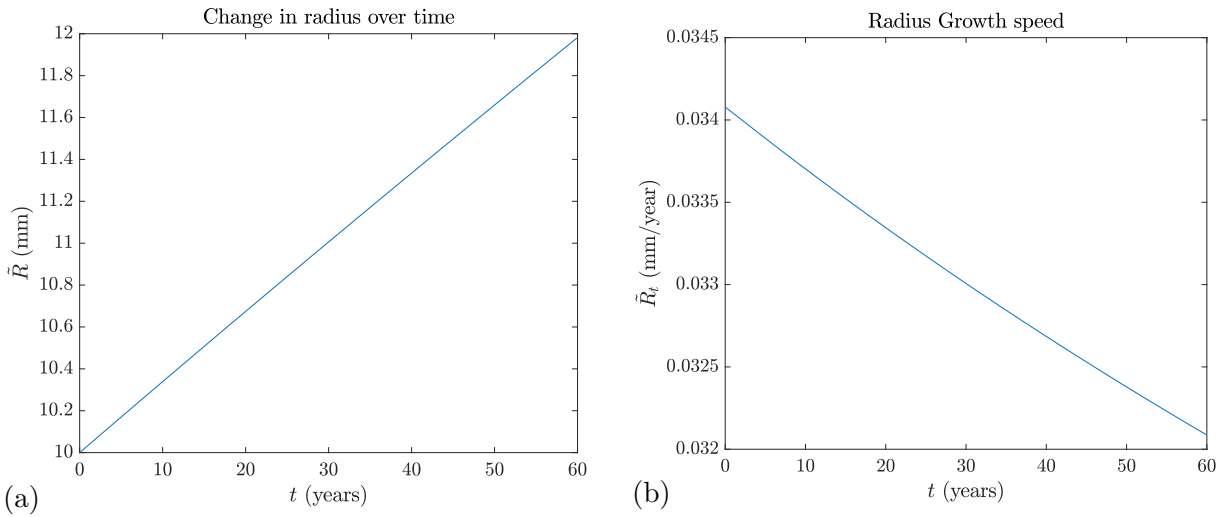


Figure 5.6: Growth of the radius for the modelled stalactite (a) shows the size of the radius and (b) shows the speed at which it grows.

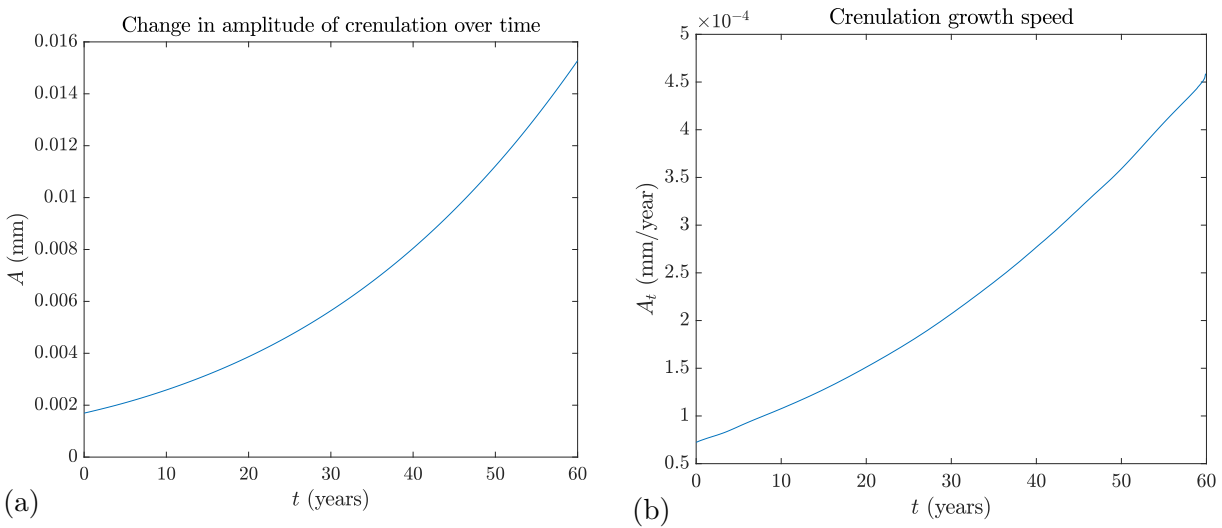


Figure 5.7: Growth of the crenulation amplitude for the modelled stalactite (a) shows the size of the amplitude and (b) shows the speed at which it grows.

we can see that the amplitude of the crenulation increases by 0.013 mm. From (b) we see that the speed at which the crenulation grows increases in time. From the linear theory, the growth rate of the crenulation depended on the amplitude, and we can see that (a) and (b) are similar curves. Figure (b) is slightly flatter however, this is because the growth rate decreases with the increased radius, due to the thinner film.

Figure 5.8 shows how the crenulation maximum migrates with time. The negative sign tells us that the crenulation is migrating upstream. As here the wavelength was 5 mm, we can see that the crenulation migrates a period in around 39 years.

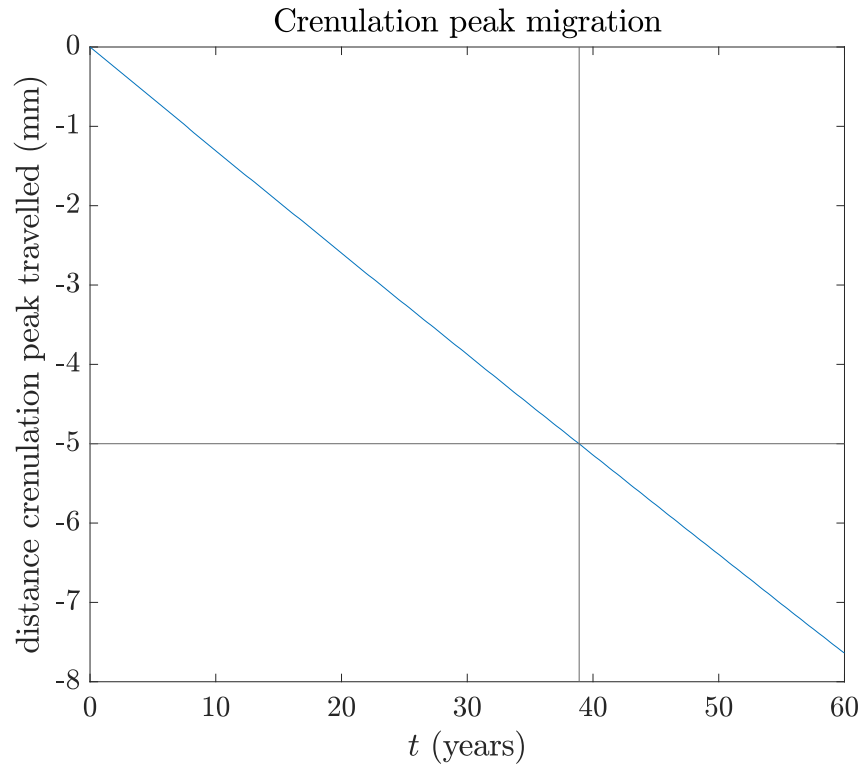


Figure 5.8: Migration of the crenulation peak.

5.5 Conclusion

In this chapter, we have looked at modelling the deposition of calcium on the surface of the stalactite. As the rate limiting reaction for the process is the conversion of bicarbonate into carbon dioxide, we have looked at how this affects the carbon dioxide concentration and calcium concentrations. We performed linear stability analysis to determine for what flow rates, radii, and wavelengths of crenulation, we would expect crenulations to form. Here we found the fastest growing wavelength increased with an increasing radius. A simplified model where the growth depended only on the fluid thickness was considered, however this suggested that no growth should occur. As the wall shape should bring z dependence to the carbon dioxide concentration, we derived a more involved model. For this, we decided to use the hydrodynamics derived in chapter 4. For this model, we assumed the calcium concentration was a constant. We looked again whether a crenulation of amplitude equal to the fluid thickness would result in growth, and we found that growth did occur for larger radii than the linear stability suggested. We then modelled an example stalactite with

wavelength and radius suggested by the linear stability analysis. Here we found that the radius grew proportionally to the fluid thickness and the crenulations grew proportionally to their amplitude. We also found that the crenulations migrate upstream.

Chapter 6

Conclusion

In this thesis, we have looked at fluid flows that result from the cylinders that have a sinusoidal surface that we expect from stalactites. Here, we have used a gradient expansion technique to develop two fluid thickness evolution equations. These models are building on models for thin film flow down a cylinder derived by Kalliadasis and Chang (1994); Frenkel (1993) but now including a small amplitude disturbance to the wall. T

The first fluid evolution equation results from a large surface tension, where the flow is driven as a result of a balance between the azimuthal and axial curvatures. From this equation, we found that the ratio between the wavelength and the radius is an important parameter, which controlled both the shape and stability of the steady states. We found the steady states to be located just before the wall trough for $L < 2\pi R$ and just after the wall maximum for $L > 2\pi R$. The cases where $L < 2\pi R$ generally lead to a larger amplitude disturbance. We performed Floquet analysis to determine the stability of the steady states. Here we found the cases where $L < 2\pi R$ were stable and the cases with $L > 2\pi R$ unstable. For the flat wall case, additional unstable modes appeared every $2\pi R$, however increasing the amplitude in the wall made the additional unstable modes appear at a longer wavelength. We then modelled the dynamics of this equation, where we found the unstable cases developed into waves. Where there was only one unstable mode in the Floquet analysis, we found that the solutions settled into time periodic waves. In the

cases with multiple unstable modes, we found that we could get many different solutions by changing the initial conditions. In these cases we could get periodic, quasi-periodic or non-periodic solutions depending on the contributions from the unstable modes. Despite the different possible solutions, we found that the time average of these solutions provided a good approximation for the steady state. For larger amplitude walls, we also found a special case, where the fluid appears to drip.

The second model for the hydrodynamics made use of a scaling to balance inertial terms with the surface tension terms. This resulted in a Benney like equation for the fluid thickness. Here the surface tension terms appeared at the same order as inertial terms, as well as an additional shear from the cylindrical geometry. Steady states were found, where again we found that for $L < 2\pi R$ the fluid was thickest upstream of the wall minimum and for $L > 2\pi R$ the fluid was thickest downstream of the wall minimum. The exact wavelength for this transition was actually slightly less, as it is deflected by ϵRe . As with the first model, the amplitude of the fluid disturbance was larger for the $L < 2\pi R$ cases. The phase shift in this model differs from the first model, with now at $L = 2\pi R$ and in the long wavelength limit the phase shift is $\theta = \pi$, where previously the phase shift was $\frac{\pi}{2}$. Increasing the amplitude of the wall made the fluid disturbance appear more nonlinear, with narrower and sometimes multiple peaks. We performed Floquet analysis to find the stability of these steady states. Here we found that inertia had a stabilising effect, with the critical wavenumber $k_0 = \sqrt{\frac{1}{R^2} + \frac{2}{5} \text{Bo Re}}$. Increasing the amplitude of the wall also acted to stabilise the steady state. Again we simulated numerical solutions and found the Floquet analysis generally provided a good insight to the dynamics. Where this analysis suggested the steady state was stable, the solution oscillated down to the steady state. Where there was one unstable mode, the fluid thickness formed a time periodic wave. With more unstable modes, the solutions exhibited quasi-periodic and non-periodic waves. The Floquet analysis was less accurate at predicting the dynamics for larger amplitudes. Here, certain stable cases were forming time periodic solutions. However, the wavelength where the first unstable solution occurred did increase with amplitude. In some cases, the larger amplitude caused the solution to blow up. With the various dynamics exhibited, it

was still found that the time average of the waves formed gave a good approximation for the steady state.

Finally, we looked at modelling the evolution of the wall of the stalactite. To do this we incorporated our second hydrodynamic model, as this model captures the effect of the flow rate, and recovers the first model for small Bond numbers. As the time average flows approximated the steady states, we used the steady state fluid thickness in the model. The growth rate depends on the calcite flux. As the rate limiting reaction for the process is the conversion of bicarbonate into carbon dioxide, we have looked at how this affects the carbon dioxide concentration and calcium concentrations. We performed linear stability analysis to determine for what size radii and flow rates we would expect crenulations to form. We calculated the fastest growing wavelength to determine the wavelength that we would expect crenulations to have. We found that this wavelength increased with the radius of the fluid, but also decreased with the flow rate. This suggests that this wavelength is linked to the fluid thickness, with thinner fluids resulting in longer wavelengths. This is in contrast to the results found by Camporeale and Ridolfi (2012); Vesipa et al. (2015); Camporeale (2017), where increasing the fluid thickness, through the Reynolds number, results in longer wavelengths. This is perhaps a consequence of the fluid flowing down a cylinder rather than a flat wall. We then looked at the growth rates for when the crenulation had already formed. Here we found that the crenulation could grow on larger radii than the linear stability suggested. This means that if the crenulation forms with the radius growing, the crenulation will also continue to grow. Finally, we modelled the growth of a stalactite starting with radius and wavelength suggested by the linear theory. Here we saw the radius grow proportionally to the fluid thickness. The crenulation grew proportionally to its amplitude, however this was also affected by the decreasing fluid thickness. Here the crenulations migrate upstream, completing a period over several decades. The upstream migration of crenulations agrees with observations made on a stalactite from in Bossea Cave (Camporeale and Ridolfi, 2012).

Future work can look to improve the fluid dynamics model by also including the slope

of the stalactite. As stalactites taper down to a tip, the model could be improved by no longer assuming periodic boundary conditions and instead modelling the stalactite as a whole. Work can also be done to improve the chemical models. Here it would be beneficial to introduce a third reaction-diffusion equation for bicarbonate, to better capture its dynamics. The problem can also be looked at with crenulations larger than the fluid thickness, to see whether that would change the rate at which they grow. Finally it would also be good to include the evolution of the radius and wavelength of the crenulations in the model.

Bibliography

- J. P. Alexander. *Systems of nonlinear PDEs arising from multi-dimensional and multi-fluid viscous shear flows*. Ph.D. thesis, Imperial College London (2021). doi:10.25560/92452.
- K. Allred and C. Allred. Tubular lava stalactites and other related segregations. *JOURNAL OF CAVES AND KARST STUDIES*, 60:131–140 (1998).
- Y. Arbel, N. Greenbaum, J. Lange, and M. Inbar. Infiltration processes and flow rates in developed karst vadose zone using tracers in cave drips. *Earth Surface Processes and Landforms*, 35(14):1682–1693 (2010). ISSN 1096-9837. doi:10.1002/esp.2010.
- A. Baker, D. Genty, and I. J. Fairchild. Hydrological characterisation of stalagmite dripwaters at Grotte de Villars, Dordogne, by the analysis of inorganic species and luminescent organic matter. *Hydrology and Earth System Sciences*, 4(3):439–449 (2000). ISSN 1607-7938. doi:10.5194/hess-4-439-2000.
- C. K. Batchelor and G. K. Batchelor. *An introduction to fluid dynamics*. Cambridge university press (2000).
- D. J. Benney. Long waves on liquid films. *Journal of mathematics and physics*, 45(1-4):150–155 (1966).
- M. B. Bertagni and C. Camporeale. Nonlinear and subharmonic stability analysis in film-driven morphological patterns. *Physical Review E*, 96(5):53115 (2017).
- A. L. Bertozzi and M. P. Brenner. Linear stability and transient growth in driven contact lines. *Physics of Fluids*, 9(3):530 (1998). ISSN 1070-6631. doi:10.1063/1.869217.

- F. Bourges, P. Genthon, A. Mangin, and D. D'Hulst. Microclimates of l'Aven d'Ornagac and other French limestone caves (Chauvet, Esparros, Marsoulas). *International Journal of Climatology*, 26(12):1651–1670 (2006). ISSN 0899-8418. doi:10.1002/joc.1327.
- D. Buhmann and W. Dreybrodt. The kinetics of calcite dissolution and precipitation in geologically relevant situations of karst areas: 1. Open system. *Chemical Geology*, 48(1):189 – 211 (1985). ISSN 0009-2541. doi:https://doi.org/10.1016/0009-2541(85)90046-4.
- C. Camporeale. An asymptotic approach to the crenulation instability. *Journal of Fluid Mechanics*, 826:636–652 (2017). doi:10.1017/jfm.2017.454.
- C. Camporeale and L. Ridolfi. Hydrodynamic-Driven Stability Analysis of Morphological Patterns on Stalactites and Implications for Cave Paleoflow Reconstructions. *Phys. Rev. Lett.*, 108(23):238501 (2012). doi:10.1103/PhysRevLett.108.238501.
- H. C. Chang, E. A. Demekhin, and D. I. Kopelevich. Nonlinear evolution of waves on a vertically falling film. *Journal of Fluid Mechanics*, 250(1):433–480 (1993). ISSN 1469-7645. doi:10.1017/S0022112093001521.
- R. V. Craster and O. K. Matar. On viscous beads flowing down a vertical fibre. *Journal of Fluid Mechanics*, 553(-1):85 (2006). ISSN 1469-7645. doi:10.1017/s0022112006008706.
- R. V. Craster and O. K. Matar. Dynamics and stability of thin liquid films. *Reviews of Modern Physics*, 81(3):1131–1198 (2009). ISSN 00346861. doi:10.1103/RevModPhys.81.1131.
- R. L. Curl. Minimum diameter stalactites. *Bulletin of the National Speleological Society*, 34(4):129–136 (1972).
- J. M. Desmarchelier, J. C. Hellstrom, and M. T. McCulloch. Rapid trace element analysis of speleothems by ELA-ICP-MS. *Chemical Geology*, 231(1-2):102–117 (2006). ISSN 0009-2541. doi:10.1016/J.CHEMGEO.2006.01.002.

- W. Dreybrodt. Deposition of calcite from thin films of natural calcareous solutions and the growth of speleothems. *Chemical Geology*, 29(1-4):89–105 (1980). ISSN 0009-2541. doi:10.1016/0009-2541(80)90007-8.
- W. Dreybrodt. The kinetics of calcite precipitation from thin films of calcareous solutions and the growth of speleothems: Revisited. *Chemical Geology*, 32(1-4):237–245 (1981). ISSN 00092541. doi:10.1016/0009-2541(81)90146-7.
- W. Dreybrodt. Chemical kinetics, speleothem growth and climate. *Boreas*, 28(3):347–356 (1999). doi:10.1111/j.1502-3885.1999.tb00224.x.
- W. Dreybrodt. *Processes in karst systems: physics, chemistry, and geology*, volume 4. Springer Science & Business Media (2012).
- H. Even, I. Carmi, M. Magaritz, and R. Gerson. Timing the transport of water through the upper vadose zone in a Karstic system above a cave in Israel. *Earth Surface Processes and Landforms*, 11(2):181–191 (1986). ISSN 10969837. doi:10.1002/ESP.3290110208.
- I. J. Fairchild and A. Baker. The Architecture of Speleothems. *Speleothem Science*, pages 205–244 (2012). doi:10.1002/9781444361094.CH7.
- I. J. Fairchild, A. Baker, A. Asrat, D. Domínguez-Villar, J. Gunn, A. Hartland, and D. Lowe. Speleothem Science: From Process to Past Environments. *Speleothem Science: From Process to Past Environments* (2012). doi:10.1002/9781444361094/FORMAT/EPUB.
- I. J. Fairchild, A. Baker, A. Borsato, S. Frisia, R. W. Hinton, F. McDERMOTT, and A. F. Tooth. Annual to sub-annual resolution of multiple trace-element trends in speleothems. *Journal of the Geological Society*, 158(5):831–841 (2001). ISSN 0016-7649, 2041-479X. doi:10.1144/jgs.158.5.831.
- A. Fick. Ueber Diffusion. *Annalen der Physik*, 170(1):59–86 (1855). ISSN 1521-3889. doi:10.1002/ANDP.18551700105.
- D. Ford and P. Williams. *Karst Hydrogeology and Geomorphology*. John Wiley & Sons (2013).

- P. Forti and G. Springer. Genesis and evolution of the square soda straws of Dry Cave, West Virginia, USA. *Journal of Cave and Karst Studies*, 82:169–182 (2020). doi:10.4311/2019ES0134.
- A. L. Frenkel. Nonlinear Theory of Strongly Undulating Thin Films Flowing Down Vertical Cylinders. *Europhysics Letters (EPL)*, 18(7):583–588 (1992). ISSN 1286-4854. doi:10.1209/0295-5075/18/7/003.
- A. L. Frenkel. On evolution equations for thin films flowing down solid surfaces. *Physics of Fluids A: Fluid Dynamics*, 5(10):2342–2347 (1993).
- D. Genty and G. Deflandre. Drip flow variations under a stalactite of the Pere Noel cave (Belgium). Evidence of seasonal variations and air pressure constraints. *Journal of Hydrology*, 211(1-4):208–232 (1998). ISSN 00221694. doi:10.1016/S0022-1694(98)00235-2.
- F. L. Hicks. Formation and mineralogy of stalactites and stalagmites. *National Speleological Society Bulletin*, 12:63–72 (1950).
- Y. Huang and I. J. Fairchild. Partitioning of Sr²⁺ and Mg²⁺ into calcite under karst-analogue experimental conditions. *Geochimica et Cosmochimica Acta*, 65(1):47–62 (2001). ISSN 0016-7037. doi:10.1016/S0016-7037(00)00513-5.
- Y. Huang, I. J. Fairchild, A. Borsato, S. Frisia, N. J. Cassidy, F. McDermott, and C. J. Hawkesworth. Seasonal variations in Sr, Mg and P in modern speleothems (Grotta di Ernesto, Italy). *Chemical Geology*, 175(3-4):429–448 (2001). ISSN 0009-2541. doi:10.1016/S0009-2541(00)00337-5.
- M. F. Johnson, R. A. Schluter, M. J. Miksis, and S. G. Bankoff. Experimental study of rivulet formation on an inclined plate by fluorescent imaging. *Journal of Fluid Mechanics*, 394:339–354 (1999). ISSN 1469-7645. doi:10.1017/S0022112099005765.
- S. W. Joo, S. H. Davis, and S. G. Bankoff. On falling-film instabilities and wave breaking. *Physics of Fluids A: Fluid Dynamics*, 3(1):231–232 (1991).

- S. Kalliadasis, C. Bielarz, and G. M. Homsy. Steady free-surface thin film flows over topography. *Physics of Fluids*, 12(8):1889–1898 (2000). doi:10.1063/1.870438.
- S. Kalliadasis and H.-C. Chang. Drop formation during coating of vertical fibres. *Journal of Fluid Mechanics*, 261:135–168 (1994). doi:10.1017/S0022112094000297.
- G. Kaufmann and W. Dreybrodt. Calcite dissolution kinetics in the system CaCO₃–H₂O–CO₂ at high undersaturation. *Geochimica et Cosmochimica Acta*, 71(6):1398–1410 (2007). ISSN 00167037. doi:10.1016/j.gca.2006.10.024.
- Y. S. Kim and D. J. Sanderson. Inferred fluid flow through fault damage zones based on the observation of stalactites in carbonate caves. *Journal of Structural Geology*, 32(9):1305–1316 (2010). ISSN 0191-8141. doi:10.1016/J.JSG.2009.04.017.
- J. P. Kuehner, M. R. Lee, M. M. Dodson, W. R. Schirmer, A. F. Vela De La Garza Evia, and L. O. Kutelak. The effect of substrate amplitude and wavelength on gravity-driven film flow inside an inclined corrugated pipe. *Physics of Fluids*, 33(11):112105 (2021). ISSN 1070-6631. doi:10.1063/5.0069664.
- J. P. Kuehner, J. D. Mitchell, and M. R. Lee. Experimental investigation of gravity-driven film flow inside an inclined corrugated pipe. *Physics of Fluids*, 31(12):122104 (2019). ISSN 1070-6631. doi:10.1063/1.5125432.
- P. L. Kumar, S. P. Thampi, and M. G. Basavaraj. Particle size and substrate wettability dependent patterns in dried pendant drops. *Journal of Physics: Condensed Matter*, 33(2):24003 (2021). ISSN 0953-8984, 1361-648X. doi:10.1088/1361-648X/abb64e.
- Y. Kuramoto. Diffusion-Induced Chaos in Reaction Systems. *Progress of Theoretical Physics Supplement*, 64:346–367 (1978). ISSN 0375-9687. doi:10.1143/PTPS.64.346.
- P. G. Ledda, G. Balestra, G. Lerisson, B. Scheid, M. Wyart, and F. Gallaire. Hydrodynamic-driven morphogenesis of karst draperies: spatio-temporal analysis of the two-dimensional impulse response. *Journal of Fluid Mechanics*, 910:53 (2021). ISSN 0022-1120. doi:10.1017/JFM.2020.1010.

- V. A. Maltsev. Stalactites with “internal” and “external” feeding. *Proceedings of the University of Bristol Speleological Society*, 21(2):149–158 (1999).
- P. Meakin and B. Jamtveit. Geological pattern formation by growth and dissolution in aqueous systems. *Proceedings of the Royal Society A: Mathematical, Physical and Engineering Sciences*, 466(2115):659–694 (2010). doi:10.1098/rspa.2009.0189.
- G. W. Moore. The growth of stalactites. *Nad. Speleo. Soc. Bull.*, 24(2):95–106 (1962).
- A. Oron, S. H. Davis, and S. G. Bankoff. Long-scale evolution of thin liquid films. *Reviews of Modern Physics*, 69(3):931 (1997). ISSN 00346861. doi:10.1103/RevModPhys.69.931.
- D. T. Papageorgiou. On the breakup of viscous liquid threads. *Physics of Fluids*, 7(7):1529–1544 (1995). ISSN 1070-6631. doi:10.1063/1.868540.
- C. Parrish, L. Pham, and S. Kumar. Thin-liquid-film flow on three-dimensional topographically patterned rotating cylinders. *Journal of Fluid Mechanics*, 918:A12 (2021). doi:10.1017/jfm.2021.224.
- B. Paul, R. Drysdale, H. Green, J. Woodhead, J. Hellstrom, and R. Eberhard. A model for the formation of layered soda-straw stalactites. *International Journal of Speleology*, 42(2):155–160 (2013). ISSN 0392-6672, 1827-806X. doi:10.5038/1827-806X.42.2.8.
- A. F. Pitty. Rate of uptake of calcium carbonate in underground karst water. *Geological Magazine*, 108(6):537–543 (1971). ISSN 0016-7568. doi:10.1017/S0016756800056752.
- L. N. Plummer, T. M. L. Wigley, and D. L. Parkhurst. The kinetics of calcite dissolution in CO₂-water systems at 5 degrees to 60 degrees C and 0.0 to 1.0 atm CO₂. *American Journal of Science*, 278(2):179–216 (1978). doi:10.2475/ajs.278.2.179.
- J. W. Raich and W. H. Schlesinger. The global carbon dioxide flux in soil respiration and its relationship to vegetation and climate. *Tellus B*, 44(2):81–99 (1992). ISSN 1600-0889. doi:10.1034/j.1600-0889.1992.t01-1-00001.x.

- A. Sadeghpour, Z. Zeng, H. Ji, N. D. Ebrahimi, A. L. Bertozzi, and Y. S. Ju. Water vapor capturing using an array of traveling liquid beads for desalination and water treatment. *Science Advances*, 5(4) (2019). ISSN 23752548. doi:10.1126/SCIADV.AAV7662.
- I. D. Sasowsky and C. T. Dalton. Measurement of pH for field studies in karst areas. *Journal of Cave and Karst studies*, 67(2):127–132 (2005).
- M. B. Short, J. C. Baygents, J. W. Beck, D. A. Stone, R. S. Toomey, and R. E. Goldstein. Stalactite Growth as a Free-Boundary Problem: A Geometric Law and Its Platonic Ideal. *Phys. Rev. Lett.*, 94(1):18501 (2005a). doi:10.1103/PhysRevLett.94.018501.
- M. B. Short, J. C. Baygents, and R. E. Goldstein. Stalactite growth as a free-boundary problem. *Physics of Fluids*, 17(8):83101 (2005b). doi:10.1063/1.2006027.
- G. I. Sivashinsky. Nonlinear analysis of hydrodynamic instability in laminar flames—I. Derivation of basic equations. *Acta Astronautica*, 4(11-12):1177–1206 (1977). ISSN 0094-5765. doi:10.1016/0094-5765(77)90096-0.
- P. A. Smithson. Inter-relationships between cave and outside air temperatures. *Theoretical and Applied Climatology*, 44(1):65–73 (1991). ISSN 0177-798X. doi:10.1007/BF00865553.
- A. F. Tooth. *Controls on the geochemistry of speleothem-forming karstic drip waters*. Ph.D. thesis, University of Keele (2000).
- D. Tseluiko, M. G. Blyth, and D. T. Papageorgiou. Stability of film flow over inclined topography based on a long-wave nonlinear model. *Journal of Fluid Mechanics*, 729:638–671 (2013). doi:10.1017/jfm.2013.331.
- D. Tseluiko, M. G. Blyth, D. T. Papageorgiou, and J.-M. Vanden-broeck. Electrified viscous thin film flow over topography. *Journal of Fluid Mechanics*, 597:449–475 (2008). doi:10.1017/S002211200700986X.
- K. Ueno. Characteristics of the wavelength of ripples on icicles. *Physics of Fluids*, 19(9):93602 (2007). doi:10.1063/1.2775484.

- K. Ueno, M. Farzaneh, S. Yamaguchi, and H. Tsuji. Numerical and experimental verification of a theoretical model of ripple formation in ice growth under supercooled water film flow. *Fluid Dynamics Research*, 42(2):25508 (2009). doi:10.1088/0169-5983/42/2/025508.
- R. Vesipa, C. Camporeale, and L. Ridolfi. Thin-film-induced morphological instabilities over calcite surfaces. *Proceedings of the Royal Society A: Mathematical, Physical and Engineering Sciences*, 471(2176):20150031 (2015). doi:10.1098/rspa.2015.0031.
- S. J. Weinstein and K. J. Ruschak. Coating flows. *Annual Review of Fluid Mechanics*, 36:29–53 (2004). ISSN 00664189.
- W. B. White. Cave minerals and speleothems. *The science of speleology*, pages 267–327 (1976).
- A. Wierschem and N. Aksel. Instability of a liquid film flowing down an inclined wavy plane. *Physica D: Nonlinear Phenomena*, 186(3-4):221–237 (2003). ISSN 0167-2789. doi:10.1016/S0167-2789(03)00242-2.
- A. Wierschem, C. Lepski, and N. Aksel. Effect of long undulated bottoms on thin gravity-driven films. *Acta Mechanica*, 179(1-2):41–66 (2005). ISSN 0001-5970. doi:10.1007/s00707-005-0242-2.
- Z. Zeng, A. Sadeghpour, and Y. S. Ju. A highly effective multi-string humidifier with a low gas stream pressure drop for desalination. *Desalination*, 449:92–100 (2019). ISSN 0011-9164. doi:10.1016/J.DESAL.2018.10.017.
- J. Zhu, J. L. Chen, R. K. Lade, W. J. Suszynski, and L. F. Francis. Water-based coatings for 3D printed parts. *Journal of Coatings Technology and Research*, 12(5):889–897 (2015). ISSN 1547-0091. doi:10.1007/s11998-015-9710-3.